

ABSTRACT

Title of Document: A POWER DISTRIBUTION SYSTEM BUILT FOR A VARIETY OF UNATTENDED ELECTRONICS

Wei Zhao, Doctor of Philosophy, 2013

Directed By: Professor Martin Peckerar
Department of Electrical and Computer Engineering

A power distribution system (PDS) delivers electrical power to a load safely and effectively in a pre-determined format. Here format refers to necessary voltages, current levels and time variation of either as required by the empowered system. This formatting is usually referred as “conditioning”. The research reported in this dissertation presents a complete system focusing on low power energy harvesting, conditioning, storage and regulation.

Energy harvesting is a process by which ambient energy present in the environment is captured and converted to electrical energy. In recent years, it has become a prominent research area in multiple disciplines. Several energy harvesting schemes have been exploited in the literature, including solar energy, mechanic energy, radio frequency (RF) energy, thermal energy, electromagnetic energy, biochemical energy, radioactive energy and so on. Different from the large scale energy generation, energy

harvesting typically operates in milli-watts or even micro-watts power levels. Almost all energy harvesting schemes require stages of power conditioning and intermediate storage – batteries or capacitors that reservoir energy harvested from the environment. Most of the ambient energy fluctuates and is usually weak. The purpose of power conditioning is to adjust the format of the energy to be further used, and intermediate storage smoothes out the impact of the fluctuations on the power delivered to the load.

This dissertation reports an end to end power distribution system that integrates different functional blocks including energy harvesting, power conditioning, energy storage, output regulation and system control. We studied and investigated different energy harvesting schemes and the dissertation places emphasis on radio frequency energy harvesting. This approach has proven to be a viable power source for low-power electronics. However, it is still challenging to obtain significant amounts of energy rapidly and efficiently from the ambient. Available RF power is usually very weak, leading to low voltage applied to the electronics. The power delivered to the PDS is hard to utilize or store. This dissertation presents a configuration including a wideband rectenna, a switched capacitor voltage boost converter and a thin film flexible battery cell that can be re-charged at an exceptionally low voltage. We demonstrate that the system is able to harvest energy from a commercially available hand-held communication device at an overall efficiency as high as 7.7 %. Besides the RF energy harvesting block, the whole PDS includes a solar energy harvesting block, a USB recharging block, a customer selection block, two battery arrays, a

control block and an output block. The functions of each of the blocks have been tested and verified.

The dissertation also studies and investigates several potential applications of this PDS. The applications we exploited include an ultra-low power tunable neural oscillator, wireless sensor networks (WSNs), medical prosthetics and small unmanned aerial vehicles (UAVs). We prove that it is viable to power these potential loads through energy harvesting from multiple sources.

A POWER DISTRIBUTION SYSTEM BUILT FOR A VARIETY OF
UNATTENDED ELECTRONICS

By

Wei Zhao

Dissertation submitted to the Faculty of the Graduate School of the
University of Maryland, College Park, in partial fulfillment
of the requirements for the degree of
Doctor of Philosophy
2013

Advisory Committee:
Professor Martin Peckerar, Chair/Advisor
Professor Neil Goldsman
Professor Mario Dagenais
Professor Robert Newcomb
Professor Aristos Christou, Dean's representative

© Copyright by
Wei Zhao
2013

Analog & Mixed Signal Systems Design Laboratory
Electrical and Computer Engineering
University of Maryland, College Park

Dedication

This dissertation is dedicated to my parents, who always support and believe in me.

I love you with all my heart

Acknowledgements

This dissertation would be incomplete without mentioning the significant contributions from my advisor, colleagues, friends and family.

First and foremost, I would like to express my deepest gratitude to my advisor, Professor Martin Peckerar, for his support and guidance of my Ph.D. study and research for the past four years, for his motivation, patience, enthusiasm, extensive knowledge and experiences. I would also like to thank my dissertation committee members as well: Professor Neil Goldsman, Professor Mario Dagenais, Professor Robert Newcomb and Professor Aristos Christou.

I would never have been able to finish my Ph.D. program without the invaluable inputs from my talented colleagues. I would like to acknowledge Dr. Zeynep Dilli for her help and guidance over the Maryland Industrial Partnerships (MIPS) project, which is a key part of my dissertation. I would also like to recognize Dr. Neil Goldsman for his support and guidance for my Ph.D. study and research, and for providing me the opportunity to work with CoolCAD Electronics, LLC, when I was able to cooperate with Dr. Akin Akturk and Dr. Siddharth Potbhare and benefited from their knowledge and skills. My special thanks also go to FlexEl, LLC for their support and help in my project, especially Dr. Daniel Lowy and Ms. Mahsa Dornajafi. I would like to thank Dr. Kwangsik Choi and Dr. Filiz Yesilkoy for their help and patient “orientation” when I first joined the group, and my other colleagues for their help and inspiring discussions including Mr. Bo Li, Mr. Scott Bauman, Mr. Chao Wang, Mr. Guannan Liu, Mr. Nick Kratzmeier, Ms. Negin Shahshahan and Ms. Jing Xia.

Finally, I would like to express my sincere thanks to my parents, for unconditionally supporting their only child traveling half way across the earth to chase his dream, like they always have been. Thank you for your wholehearted love and devotion throughout the years. I would also like to acknowledge my other family members, especially my grandmother, who have always believed in me ever since she taught me how to read.

Last but not the least, I would like to thank all the individuals that I have worked with and all the friends I met in United States during this journey. I am blessed to have you in my life.

Table of Contents

Dedication	ii
Acknowledgements	iii
Table of Contents	v
List of Tables	vii
List of Figures	viii
Chapter 1: Introduction	1
1.1 Motivation	1
1.2 Overview of Different Energy Harvesting Schemes	3
1.2.1 Solar Energy Harvesting	3
1.2.2 Radio Frequency Energy Harvesting	9
1.2.3 Other Energy Harvesting Schemes	15
1.3 Power Conditioning	21
1.4 Energy Storage	25
1.4.1 Batteries	26
1.4.2 Supercapacitors	28
1.5 Summary of Open Literature Results on RF Energy Harvesting	29
1.6 The Proposed Power Distribution System	33
1.7 Summary of Contributions	34
Chapter 2: Broadband Rectenna Design	38
2.1 Antenna Overview	38
2.2 Design Analysis	39
2.3 Rectenna Fabrication and Testing	42
Chapter 3: Switched Capacitor DC – DC Converter Design	44
3.1 Power Loss Analysis of the Switched Capacitor DC - DC Converter	44
3.2 Circuit Structure	47
3.3 Simulations and Experiments	51
3.3.1 Basic Function verification	51
3.3.2 Capacitive Load Charging Simulations and Experiment	52
3.3.3 Frequency Dependency Experiments	55
Chapter 4: Energy Storage Solution: A Supercapacitor/Battery Hybrid Cell	58
4.1 Cell Overview	58
4.2 Electrical Characteristics of the Battery	60
4.3 Battery Recharge Experiment with SC Voltage Converter	65
Chapter 5: Power Distribution System Integration	68
5.1 Solar Energy Harvesting Block	68
5.2 USB Recharging Block	72
5.3 Output Voltage Regulator	73
5.4 Microcontroller Overview	76
5.5 System Overview	81
5.5.1 Battery Arrays	81
5.5.2 Microcontroller Implementation	85
5.5.3 Printed Circuit Board Design	92

5.6 RF Energy Harvesting Experiments	94
5.7 Discussions of the RF Energy Harvesting Experiments	106
5.8 Power Budget of the PDS	108
5.9 Investigation of Alternative Solutions to the RF energy harvesting block.....	111
Chapter 6: Potential Applications Design and Measurements	118
6.1 An Ultra Low Power Tunable Neural Oscillator for Biological Rhythmic Behaviors	118
6.1.1 Neuron Oscillation Overview	118
6.1.2 Research Background	120
6.1.3 Circuit Structure and Operation	122
6.1.4 Simulation Results	129
6.2 Wireless Sensor Networks	132
6.3 Brief Examination of a Prosthetics System	136
6.4 An Evaluation of Powering Unmanned Aerial Vehicles (UAVs)	138
Chapter 7: Conclusions.....	149
7.1 Summary of Contributions.....	149
7.2 Future Work	153
7.2.1 Possible Improvements of the Power Distribution System.....	153
7.2.2 Future Research Trends and Challenges in Energy Harvesting.....	156
7.3 Conclusions.....	158
Appendix A: Original C Code for the Microcontroller (excluding the library files that are called).....	161
Chapter 8: Bibliography	187

List of Tables

Table 1-1. Comparison of the recent research results of RF energy harvesting	31
Table 2-1. Parameters of Schottky diode SMS7630	42
Table 3-1 Frequency Dependency of the converter in the 1000uF capacitor charging	57
Table 4-1. Comparison between the reported battery cell and commercially available rechargeable thin film batteries	63
Table 5-1. List of components used in the solar cell recharging protection circuit....	70
Table 5-2. Voltage regulator comparison	75
Table 5-3. Testing results of voltage regulating block based on LTC3564	76
Table 5-4. Testing results of Si1035X	85
Table 5-5. Values in calculation of recharging efficiency using “capacitance modeling method” in the first experiment	100
Table 5-6. Values in calculation of recharging efficiency using “voltage reference method” in the first experiment	101
Table 5-7. Recharging efficiency calculation using “capacitance modeling method” of the second RF energy harvesting system test	103
Table 5-8. Values in calculation of recharging efficiency using “voltage reference method” in the second experiment.....	103
Table 5-9. Comparison of two RF energy harvesting experiments and their efficiencies calculation.....	103
Table 5-10. Values in calculation of recharging efficiency using “voltage reference method” in 4 battery experiment.....	106
Table 5-11. Large capacitors experiment results of the dual band RF energy harvesting block	115
Table 5-12. Large capacitors experiment results of the dual band RF energy harvesting block with 1 μ F capacitors in the SC voltage converter.....	116
Table 6-1. Cycle of a Prosthetic Electronic Device	136
Table 6-2. Run times calculated for a prosthetic device operated with a 3 cm ³ Zn-RuO ₂ ·xH ₂ O battery	137
Table 6-3. Power requirements of the tested airplane and motor	140

List of Figures

Figure 1.1. Block diagram of the proposed power distribution system	3
Figure 1.2. A typical structure of a solar cell.....	4
Figure 1.3. The electron-hole pair generation process in a solar cell	5
Figure 1.4. The equivalent circuit of a typical solar cell	6
Figure 1.5. (a) PV cell, (b) PV cell array	7
Figure 1.6. Solar cell energy conversion efficiency comparison of different technologies [13].....	9
Figure 1.7. Range of ambient RF power available and various efficiencies reported in the literature [15].....	10
Figure 1.8. A typical structure of an RF energy harvester.....	11
Figure 1.9. Impedance matching illustration and the equivalent circuit.....	12
Figure 1.10. The three most used matching configurations in RF energy harvesters: (a) transformer; (b) shunt inductor and (c) LC network	14
Figure 1.11. A cantilever beam with a tip mass.....	16
Figure 1.12. Multi-mode mechanical energy harvester using piezoelectric and electromagnetic schemes	18
Figure 1.13. Magnetolectric composites in a layer by layer structure	18
Figure 1.14. An example structure of a thermoelectric harvester.....	19
Figure 1.15. Typical linear regulator configuration using PMOS	22
Figure 1.16. A typical illustration of a magnetic switching buck converter.....	23
Figure 1.17. A typical illustration of a magnetic switching boost converter	23
Figure 1.18. A typical working process of a charge pump. In phase (a) capacitors C_1 to C_N are charged in parallel. In phase (b), capacitors are changed into series to output a higher voltage.....	24
Figure 1.19. A typical configuration of a ac-dc switching converter: bridge rectifier	25
Figure 1.20. A typical battery model	26
Figure 1.21. Volumetric energy density versus the gravimetric energy density for common secondary battery types [3]	27
Figure 1.22. Structure of a supercapacitor	29
Figure 1.23. Equivalent circuit of a supercapacitor	29
Figure 1.24. Block diagram for the RF energy harvesting block.....	34
Figure 2.1. Equivalent circuit of an antenna	38
Figure 2.2. Shape of a designed single spiral antenna	40
Figure 2.3. The designed broad band rectenna	41
Figure 3.1. Ideal model of a SC voltage converter	45
Figure 3.2. Illustration of energy loss in switches in switched capacitor converter ...	46
Figure 3.3. Schematic of SC voltage converter in three stage illustration.....	48
Figure 3.4. Operations of switched capacitor voltage converter	49
Figure 3.5. Layout of the SC voltage converter	49
Figure 3.6. Electrostatic discharge protection on pad.....	50
Figure 3.7. Photograph of the SC voltage converter.....	50
Figure 3.8. Block diagram of the SC converter chip at work	51
Figure 3.9. Three stage converter operation for 0.35 V input at 20 Hz switching using 100 μ F external capacitors	52

Figure 3.10. Simulation results of load voltage in 100 μ F capacitor charging	53
Figure 3.11. Experiment results of load voltage in 100 μ F capacitor charging.....	53
Figure 3.12. Simulation results of input current in 100 μ F capacitor charging	54
Figure 3.13. Experiment results of input current in 100 μ F capacitor charging.....	54
Figure 3.14. Frequency dependency of 1000 μ F capacitor charging with 0.35V input and three 100 μ F external storing capacitors	56
Figure 4.1. (A) Cross-section of the single-sheet Zn–RuO ₂ ·nH ₂ O galvanic cell: 1—Zn anode; 2—RuO ₂ ·nH ₂ O /activated carbon cathode, where 2a—paste containing Ru(IV) oxide nanoparticles and 2b—graphite film current collector; 3—separator; 4—packaging and sealing materials. (B) Photograph of an assembled ultrathin cell [48].....	60
Figure 4.2. Discharge curve of a thick film RuO ₂ ·nH ₂ O galvanic cell over 1 k Ω load. Blue curve shows the cell voltage and red curve shows the capacity [48].	61
Figure 4.3. Capacity monitoring for a representative thin and flexible Zn–RuO ₂ ·nH ₂ O galvanic cell [48].....	62
Figure 4.4. Life cycle test of the battery cell. Top figure shows a total of 800 cycles. Bottom left shows the early cycles. Bottom right shows the later cycles [47].	63
Figure 4.5. Burst discharge capability of a 1 cm ² battery cell [47].	63
Figure 4.6. First 40 hours of a battery’s discharge curve. The RC-discharge profile fit to the capacitive region of the battery operation.....	65
Figure 4.7. Results of the battery cycle test. (a) Discharging test results for 16 hours (1 K Ω load), (b) Potential change during 24 hours charging (0.25 V input, 1 Hz clock signal), and (c) 10 minutes discharging after charging (1 K Ω load).	67
Figure 5.1. Photograph of solar cells used in the system.....	68
Figure 5.2. Solar cell recharging protection circuit diagram	69
Figure 5.3. 2200 μ F capacitor charging with the system solar energy harvesting block and iPhone flashlight.....	71
Figure 5.4. Circuit diagram of the step down converter for USB recharging.....	73
Figure 5.5. Schematic diagram of single series voltage regulator	74
Figure 5.6. Circuit diagram of output voltage regulator	76
Figure 5.7. EM6819 overview [69].....	78
Figure 5.8. Block diagram of the microcontroller EM6819	80
Figure 5.9. Circuit diagram of a single battery array	82
Figure 5.10. Internal circuit of Si1035X [70]	82
Figure 5.11. Absolute maximum ratings of Si1035X [70]	83
Figure 5.12. Specifications of Si1035X [70]	84
Figure 5.13. Testing circuit and the transmission gate Si1035X	85
Figure 5.14. The REva mother board for microcontroller EM6819 [72]	86
Figure 5.15. Development environment of RLink.....	87
Figure 5.16. Block diagram of the power distribution system and signal/power line routing.....	88
Figure 5.17. Flow chart of the microcontroller program	90
Figure 5.18. Layout of the power distribution system PCB	92
Figure 5.19. PCB of the power distribution system.....	93
Figure 5.20. Experimental setup of the RF energy harvesting system. The voltage converter is an integrated silicon IC in package being tested on the bread board.	95

Figure 5.21. Panel configuration of the designed LabView program.....	96
Figure 5.22. Block diagram of the designed LabView program.....	96
Figure 5.23. Comparison of two discharging processes & the battery potential change during 1 h charging.....	98
Figure 5.24. Change of battery potential during recharge	98
Figure 5.25. Comparison of the first and second discharge processes (curves A and B, respectively) of the second test.....	102
Figure 5.26. Change of battery potential during charging over about 1 h of the second discharge	102
Figure 5.27. The two discharge profiles of four batteries recharging experiment....	105
Figure 5.28. The voltage change during recharge of 4 batteries in parallel.....	105
Figure 5.29. Normal operation of the SC voltage converter in the PDS (yellow waveform is the input signal, blue waveform is the output signal)	113
Figure 5.30. The operation of SC voltage converter working with the dual band (yellow waveform is the input signal, blue waveform is the output signal)	114
Figure 6.1. Structure of a typical neuron. Adapted from [89].	119
Figure 6.2. Block diagram of the oscillator	122
Figure 6.3. The compact silicon neuron circuit [98].....	123
Figure 6.4. Change of Slow variable and Membrane potential with input.....	124
Figure 6.5. Circuit diagram of the synapse [99]	125
Figure 6.6. Circuit diagram of the Schmitt Trigger	126
Figure 6.7. Schematic and transfer curves of Schmitt trigger.....	126
Figure 6.8. Symmetrical oscillation	130
Figure 6.9. Tuning of the duty cycle.....	130
Figure 6.10. High frequency oscillation	131
Figure 6.11. Low frequency oscillation	131
Figure 6.12. Current consumption of a Resensys sensor while sensing and transmitting. The left circuit shows the utilized test circuit (picture, courtesy of Resensys LLC, www.resensys.com).....	134
Figure 6.13. Resensys sensor running test for 24 hours with 3 battery cells in series	135
Figure 6.14. Ember 2 airplane.....	140
Figure 6.15. EM400 motor with EP1260 propeller	141
Figure 6.16. Ember 2 airplane and battery arrays.....	143
Figure 6.17. The Ember 2 airplane test with 2 batteries in series as a group, and 3 such groups in total to power the airplane	144
Figure 6.18. The Ember 2 airplane test with 3 batteries in series as a group, and 3 such groups in total to power the airplane	144
Figure 6.19. The Ember 2 airplane test with 4 batteries in series as a group, and 2 such groups in total to power the airplane	145
Figure 6.20. The Ember 2 airplane test with 4 batteries in series as a group, and 3 such groups in total to power the airplane for over 3 hours.....	146
Figure 6.21. The EM400 motor and EP1260 propeller test with 4 batteries in series as a group, and 2 such groups in total for 900 s.....	147
Figure 6.22. Battery banks mounted an UAV wing.....	148

Figure 7.1. Power distribution system with a tuning network to match the impedance while keep the wide band harvesting feature 154
Figure 7.2. I-V and P-V curves of a typical solar cell with the MPP marked 155

Chapter 1: Introduction

1.1 Motivation

Energy harvesting is a process by which ambient energy present in the environment is captured and converted to electrical energy [1]. It has become a prominent research area and continues to grow in aspects such as materials, circuits design and system integration [2]. Compared to large-scale renewable energy generation, energy harvesting typically refers to collection of milli-watt or even micro-watt power levels. Major ambient sources for energy harvesting include solar energy, radio frequency (RF) energy, thermal energy, kinetic energy and electromagnetic radiation.

The current interest in energy harvesting is largely sparked by the development of autonomous wireless electronic systems. Wireless sensor networks (WSNs) which are composed of wireless sensor nodes is an example application. Typically, each node includes a sensor, a transceiver for wireless communication, processing and control electronics and power supply. In order to achieve wireless communication, the node is usually powered by a battery. However, batteries all have a limited lifetime. They have to be replaced periodically or recharged. But replacing all the batteries in a whole network doesn't seem reasonable in most cases. First, the maintenance costs are not economically feasible when the number of nodes is very large. Second, some nodes in WSNs may be difficult or impractical to access without compromising the system performance. Third, battery disposal raises environmental concerns [1]. Therefore, energy harvesting becomes a promising solution, to supply

sustainable energy to the nodes. Driven by the demands, energy harvesting has a wide range of applications including embedded wireless sensors for health and bridge monitoring, powering unmanned aerial vehicles (UAVs) and medical prosthetics.

Solar energy is a popular source for energy harvesting due to its great abundance. However, it cannot be harvested for electronics at nights, used in shadows or within structures. RF energy exists almost ubiquitously in the environment, and it can be a complementary source for solar energy. However, it is usually very weak. These features have made RF energy a viable source for low power electronics, yet very challenging to obtain significant amounts of energy fast and efficiently from the ambience. It is necessary to exploit the possibility to integrate harvesting schemes from multiple energy sources.

The energy from ambient space is usually weak and unstable. Additionally, it needs to be formatted to further power potential electronics. Therefore, the design power conditioning, energy storage and regulation is of great importance to utilize the harvested energy efficiently. However, most of the research in literature only focuses on one aspect of the problem, and lacks the implementation from an integrated point of view.

Based on these observations, we have designed and fabricated an end-to-end power distribution system with a focus on RF energy with the block diagram shown in Figure 1-1. The PDS is able to harvest energy from multiple sources, and can be used to supply power for a number of unattended electronics. The PDS includes: the transducer that draws energy from the environment (for example, an antenna for RF scavenging); matching networks that enable efficient coupling of the transducer to the

energy source and to subsequent stages of the PDS; voltage multipliers, energy storage subsystems; power conditioning and regulators. These subsystems are shown in the figure and each will be discussed in detail in subsequent chapters of this thesis.

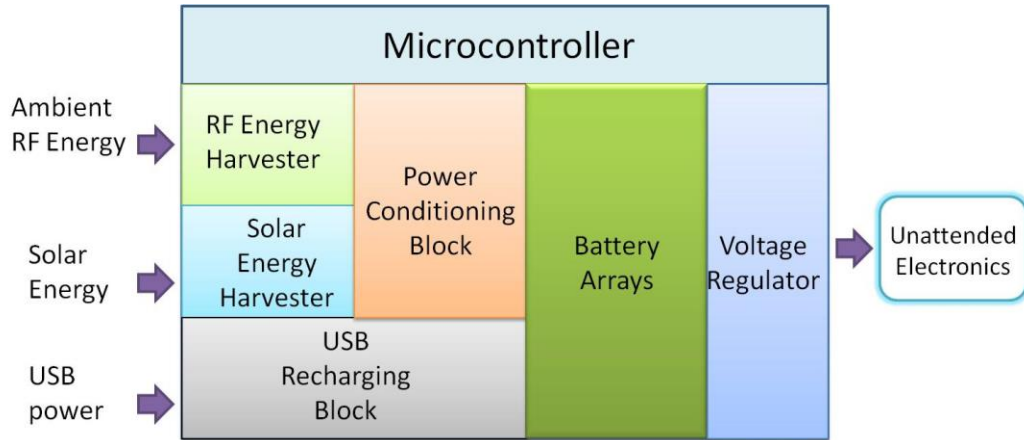


Figure 1.1. Block diagram of the proposed power distribution system

1.2 Overview of Different Energy Harvesting Schemes

1.2.1 Solar Energy Harvesting

Solar energy is by far the most significant ambient energy source on Earth. It is also referred to as optical energy [3]. Because of its abundance and greatest availability compared to other energy sources, solar energy has been exploited and utilized in numerous ways. Studies show that over 10^{24} J of solar energy reaches the Earth every year, which is over a hundred times more than the second largest energy source, wind [4]. The available power density differs according to the weather

condition, location on the Earth, the day in the year and the time of the day. For instance, the outdoor power density on the Earth surface is about 100 mW/cm^2 on a sunny day at noon [3]. The indoor optical energy comes from the sun as well as the illumination. The typical indoor value ranges from $100 \text{ }\mu\text{W/cm}^2$ to $1000 \text{ }\mu\text{W/cm}^2$.

Solar energy is harvested by solar cells, or photovoltaic cells (PVs), by converting it to electricity. A typical structure is shown in Figure 1.2. It is the physical process known as photoelectric effect. A solar cell is basically a semiconductor diode. A large amount of the light shining on the cell is partly absorbed, creating electron-hole pairs (EHPs) in the process. The other part of the light may either be reflected or transmit through the cell. These electron-hole pairs create a current flow to external loads. This process is illustrated by Figure 1.3. The ideal solar cell would have 100% absorption, 100% electron and hole separation and be stable forever.

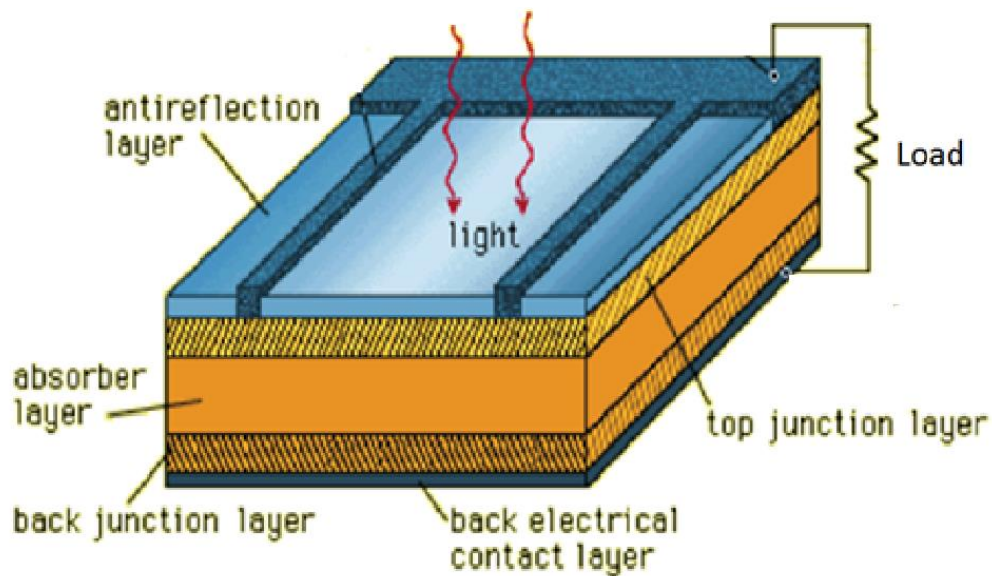


Figure 1.2. A typical structure of a solar cell

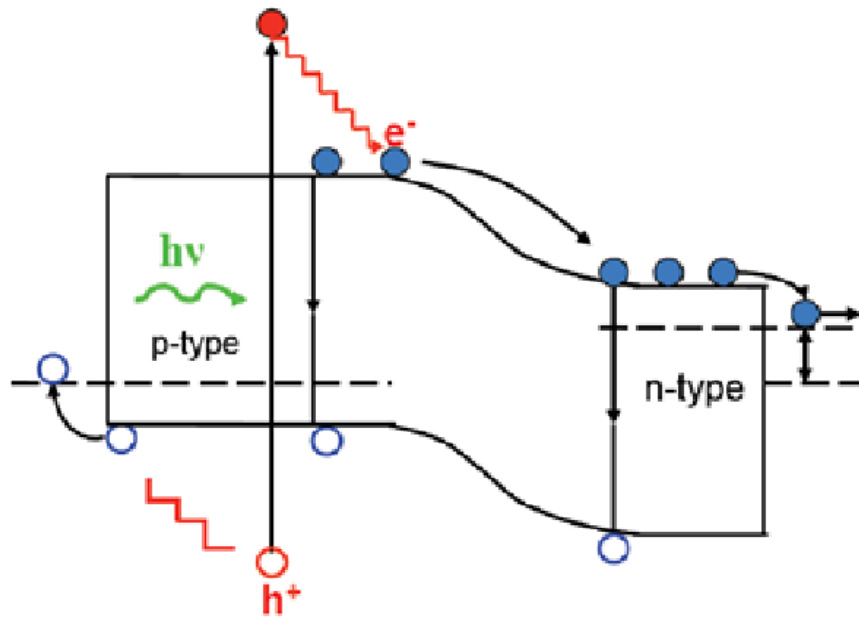


Figure 1.3. The electron-hole pair generation process in a solar cell

A typical solar cell can be modeled as a current source and diode in parallel with each other, as shown in Figure 1.4. There are also a shunt resistor and a series resistor. The diode models the p-n junction while R_{SH} represents the leakage current in it. Its value is usually very high. R_S models the ohmic contacts with the silicon.

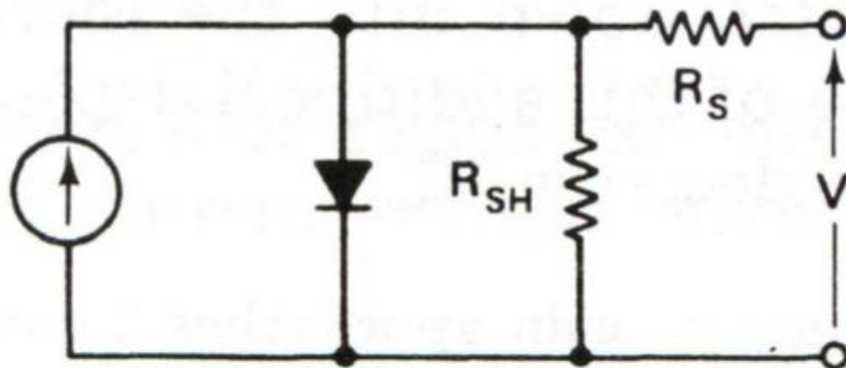


Figure 1.4. The equivalent circuit of a typical solar cell

There are a few other important parameters of a solar cell. V_{OC} is the open circuit voltage, which is stable at a high light intensity by varies in low power input. The short circuit current, I_{SC} , is typically proportional to the incoming light intensity. The relationship between the output voltage V and current I of a solar cell can be described by [5]:

$$I = I_{PH} - I_0 \left[e^{\frac{q(V+R_S I)}{n_d K T}} - 1 \right] - \frac{V + R_S I}{R_p} \quad (1-1)$$

where I_{PH} is the light-generated current and can be approximated as I_{SC} . I_0 is the reverse saturation current of the diode. n_d is the ideality factor of the diode. K is the Boltzmann constant and T is the temperature in Kelvin. The temperature of the cell can be derived in Celsius by the following empirical equation [3]:

$$T_{cell} = T_a + \frac{NOCT - 20}{800W / m^2} G \quad (1-2)$$

where T_a is the ambient temperature, G is the incident light intensity in W/m^2 , and NOCT stands for nominal operating cell temperature, which is an empirical parameter.

In practice, as shown in Figure 1.5, solar cells are often connected together to form larger units called modules, to meet the particular energy demands. Further, the modules in turn, can be interconnected to produce more power, and the unit is called an array. PV systems can be categorized into two classes [6]: flat-plate systems and concentrator systems, based on the sunlight collection method. The difference between them is that the concentrator system collects sunlight and focuses it on the

PV panels with reflectors and lenses, while the flat-plate system uses direct sunlight or that diffused in the environment.

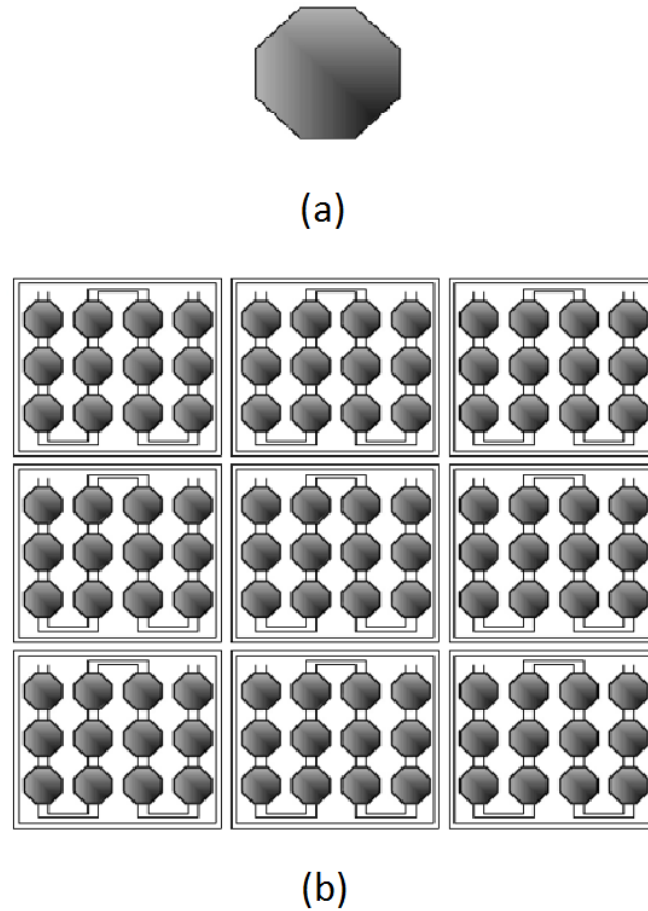


Figure 1.5. (a) PV cell, (b) PV cell array

Currently solar cells can be fabricated from various types of semiconductor materials in multiple structures [7]. Three major types of the PV cells now are silicon, polycrystalline thin films and single-crystalline thin film [8]. The PV cell market is now dominated by silicon, including monocrystalline, polycrystalline and amorphous forms [9]. Silicon is the most popular material for solar cells for a long time. It is the

second most abundant element in the earth's crust just behind oxygen. But it has to be purified to 99.9999% in order to be used as solar cell materials [10]. The molecular structure in single crystal silicon is uniform, which is suitable for electrons transferring. On the other hand, semi-crystalline silicon lacks the uniformity, so it is much less expensive to produce. The polycrystalline thin film materials include copper indium diselenide (CIS), cadmium telluride (CdTe) and thin film silicon. They are deposited in very thin layers of atoms, molecules or ions [11]. Single crystalline thin films include GaAs, which is a high-efficiency compound semiconductor of gallium and arsenic. It has high absorption ratio and insensitive to heat, making it very suitable for space applications.

The energy conversion efficiency of a solar cell is defined as the ratio of generated electrical power to the incident optical power. The reported efficiencies range from as high as over 25 % tested in labs, to less than 5 % commercial amorphous cells [12]. Figure 1.6 shows a summary of energy conversion efficiencies of different technologies. It can be noted that there is still an obvious gap between the lab results and the PV module efficiencies.

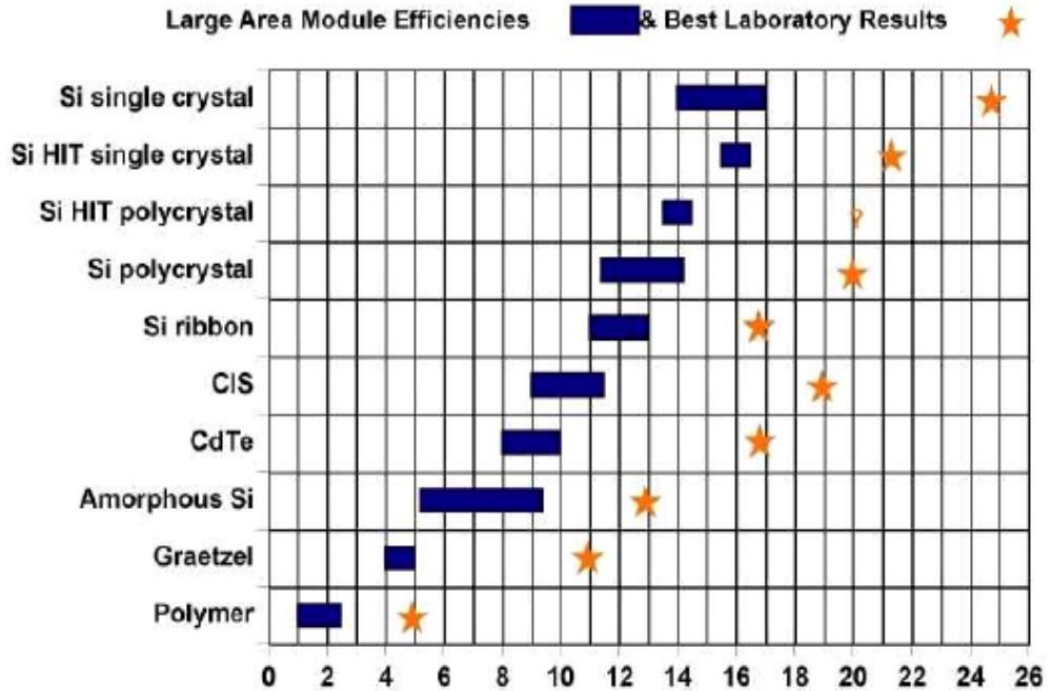


Figure 1.6. Solar cell energy conversion efficiency comparison of different technologies [13]

1.2.2 Radio Frequency Energy Harvesting

RF signals are deliberately radiated, usually by broadcasting station antennas and cellular phone antennas to cover a wide range of communication services [3]. They can also be unintentionally radiated by industrial, scientific and medical (ISM) applications without license. There are two features of RF signals: they are ubiquitous, especially in urban areas, and they are usually weak in power. A study which surveyed 560 RF spot measurements for 280 randomly selected residents living in 161 different homes shows that the exterior RF power values ranged from nondetectable to $20.9 \mu\text{W}/\text{cm}^2$, all below the general public exposure limit of $200 \mu\text{W}/\text{cm}^2$. The in-home power density ranged from nondetectable to $6.7 \mu\text{W}/\text{cm}^2$ [14]. However, when close to the transmitter, the power density can be much higher.

Consider a single point RF power source transmitting in free space, the power density at any point can be expressed as the following equation:

$$S = P_0 \frac{1}{4\pi d^2} \quad (1-3)$$

where P_0 is the effective power radiated from the source, and d is the distance from the source to the measuring spot. The available power received by an antenna (P_{RF}) is related to the effective antenna aperture (A_e). The power can be expressed as:

$$P_{RF} = S \times A_e = P_0 G_{RF} \frac{\lambda^2}{(4\pi d)^2} \quad (1-4)$$

where λ is the wavelength of the RF signal, and G_{RF} is the antenna gain. The equation shows that as the frequency of the signal increases (wavelength decreases), the available power received by the antenna will decrease. The most widely used antenna types are broadband and circularly polarized [15], since the RF energy to be harvested is in most cases multiband with different polarizations. Figure 1.7 shows the range of ambient RF power levels available and various efficiencies reported in the literature.

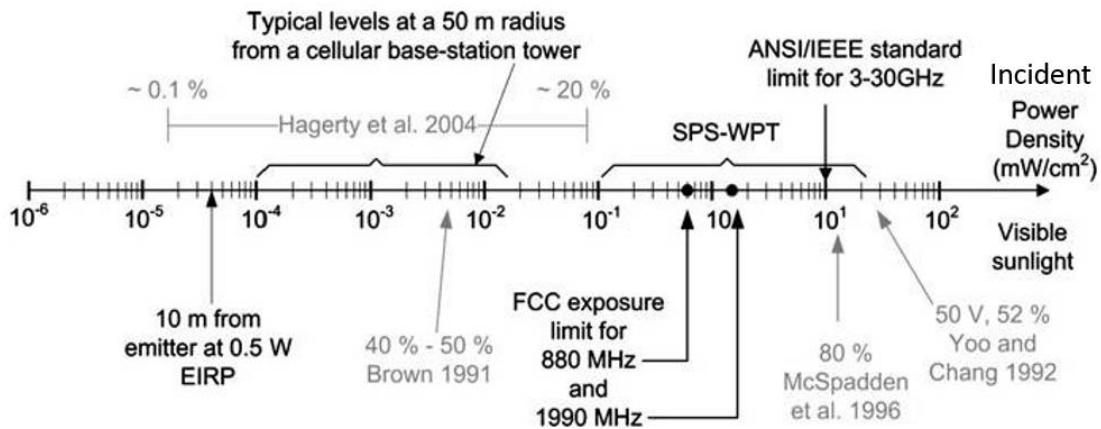


Figure 1.7. Range of ambient RF power available and various efficiencies reported in the literature [15]

Although RF energy is usually much weaker in the environment compared to solar energy, it can be used in situations that solar energy is difficult to access. For example, RF energy is superior at nights or even cloudy days, and for devices used in shadows or within structures. However, a certain level of signal conditioning has to be achieved in order to utilize to store the RF energy harvested.

A typical RF energy harvester consists of the following blocks as shown in Figure 1.8 an antenna, an impedance matching network, an optional filter block and a rectifier to convert the signal from ac to dc.

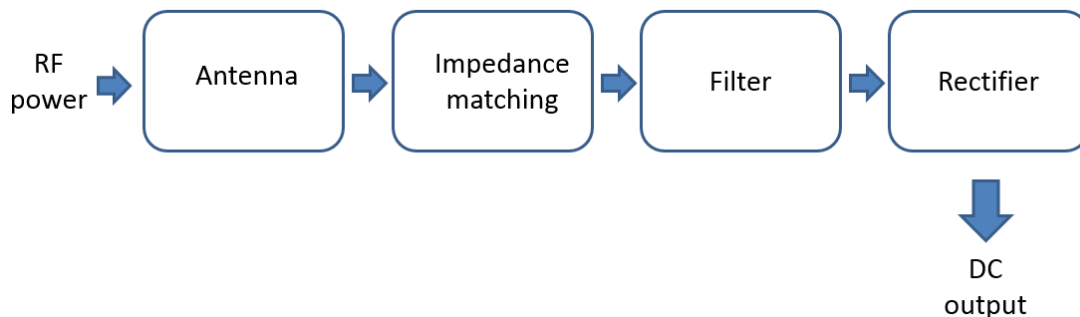


Figure 1.8. A typical structure of an RF energy harvester

In the near-field region, where the signal wavelength is much greater than the powering distance, the most widely used antennas are coils. The distances beyond approximately $\lambda/2\pi$ are generally considered as far-field region, where λ is the wavelength. In this region the field strength attenuates with respect to $1/d$, and the power intensity attenuates according to $1/d^2$, where d is the distance between the power source and the receiving antenna.

Impedance matching is often necessary in RF energy harvester design to provide the maximum possible power transfer between antenna and the next stage, especially in systems aiming at low power applications. In time varying waveforms, the maximum transfer of power occurs when the load impedance equals to the complex conjugate of the output impedance of the source. Figure 1.10 shows a simple illustration of the impedance matching and the equivalent circuit after matching, where the subscript S denotes source and L denotes load. A well matched design is important for antennas and rectifiers. The matching network is typically made of reactive components (capacitors and inductors), which don't consume real power.

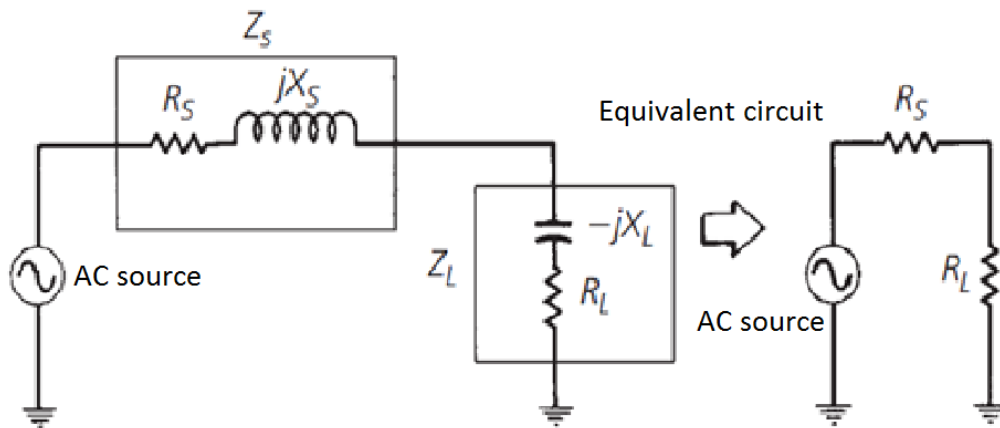


Figure 1.9. Impedance matching illustration and the equivalent circuit

Three main configurations are used for impedance matching in energy harvester designs: transformer matching as shown in Figure 1.9 (a), shunt inductor matching as shown in (b) and LC network matching as shown in (c). The source in the figure can be seen as an antenna with a resistor in series. The RC load can be

viewed as the rectifier in the next stage. The transformer configuration is able to boost the voltage up by k times. However, the cost of this configuration is usually high [16]. In the shunt inductor configuration, the inductor value must be able to resonate with the load capacitor described by the following equation:

$$L_{shunt} = \frac{1}{\omega^2 C_{in}} \quad (1-5)$$

where ω is the signal frequency. The LC network configuration is able to boost up the antenna voltage, which is usually more convenient for the rectifier to use. In order to achieve the conjugate impedance of the rectifier, the matching network LC values can be calculated as follows:

$$L_m = \frac{R_{in}}{\omega} \frac{1}{R_{in} C_{in} \omega + \sqrt{\frac{R_{in} - R_s}{R_s}}} \quad (1-6)$$

$$C_m = \frac{1}{R_s \omega} \sqrt{\frac{R_s}{R_{in} - R_s}} \quad (1-7)$$

Some custom designed antennas are matched to the rectifiers at a specific frequency and power level, while some other wide band antenna design seeks the tradeoff between impedance matching and wide working frequency range.

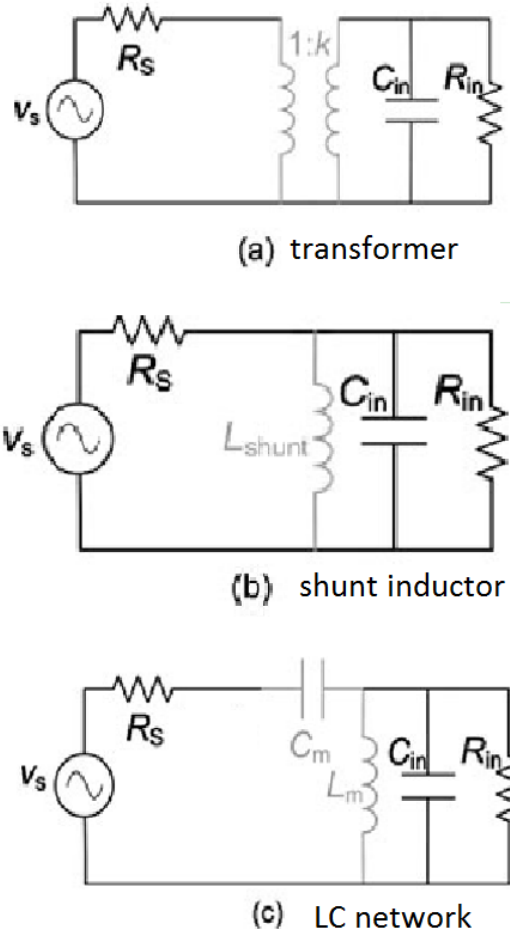


Figure 1.10. The three most used matching configurations in RF energy harvesters: (a) transformer; (b) shunt inductor and (c) LC network

Optional filters are needed in an RF energy harvester when the designer wants to rule out the harmonics generated by the rectifiers and other circuit blocks. The harmonics could flow back to the antenna and reduce the energy conversion efficiency [17]. If a filter block is added, two matching circuit will be necessary including one from the antenna to the filter, and the other from the filter to the rectifier.

The rectifiers convert ac signals to dc form for future use. It will be explained in details in Section 1.3, Power Conditioning.

1.2.3 Other Energy Harvesting Schemes

Mechanical energy harvesting is another active research area. This energy is broadly available in the ambient space and as a result has attracted much attention [18]. The sources of mechanical energy include vibrations, human body activities, liquid or gas flow and pressure variations [3]. The frequencies of mechanical energy vary according to the sources. Human movements generate energy with less than 10 Hz frequency, including active and passive activities, where active movements come from deliberate motions and passive activities are caused by daily routines such as heel strike. Machinery vibrations are typically over 30 Hz [1]. Mechanical energy harvesters employ one of the following principles for energy conversion: piezoelectric, electrostatic and electromagnetic. Reported efficiencies range from below 1 % [18] to 20 % [19].

Electrostatic converters use variable capacitors to generate energy. The typical method is to fix one plate of the capacitor, and control the other plate by mechanical forces. One of the advantages of this technique is that they can be fabricated in IC. The energy can be extracted by either charge constraint technique [20] or voltage constraint technique [21]. The harvested energy can be calculated by the following equation:

$$E = \frac{1}{2} Q^2 \left(\frac{1}{C_{\min}} - \frac{1}{C_{\max}} \right) \quad (1-8)$$

Piezoelectricity is the effect that some materials turn mechanical stress into electric field or electric potential. Accordingly, reverse piezoelectric effect refers to the case where the stress and/or strain is turned into electric field. It was discovered by Pierre Curie and Jacques Curie in 1880 [2]. The nature of piezoelectric effect oriented from the change of electric dipole moments and polarization of the materials, a re-configuration and orientation of the dipole inducing and molecular dipole moments. Piezoelectric harvesters usually employ several operational modes, including the most widely used mode 33 and 31. Mode 33 typically relates to energy harvesting from passive human motion, and mode 31 is more suitable in cantilever structures, as shown in Figure 1.11. The piezoelectric cantilever beam is configured with a mass at the tip. Generally, the piezoelectric energy harvesters are modeled as an ac current source with a capacitor in parallel [22]. It is still challenging to integrate the transducer into ICs.

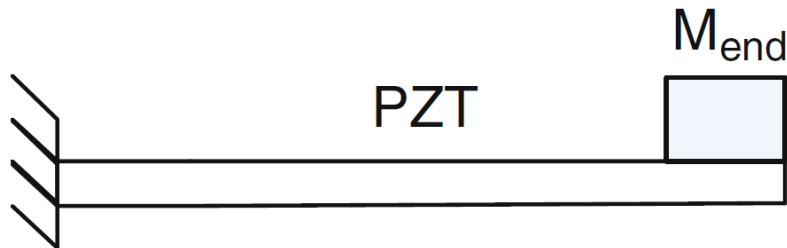


Figure 1.11. A cantilever beam with a tip mass

There are 4 general categories of piezoelectric materials: Piezoelectric polycrystalline ceramics, piezoelectric single crystal materials, piezoelectric and electrostrictive polymers and piezoelectric thin films. Two important parameters are used to describe the quality of a specific material in piezoelectricity, namely piezoelectric strain constant and piezoelectric voltage constant. The two widely used high energy density materials are polyvinylidene fluoride (PVDF) and relaxor piezoelectric single crystal.

Electromagnetic energy harvesting is based on Faraday's law. It states that a voltage will be generated with a time variable magnetic flux, as described in the equation below:

$$v = -\frac{d\phi}{dt} \quad (1-9)$$

The voltage is generated in a conductor, typically a coil. And the magnetic flux can be provided by a permanent magnet. The electromagnetic energy harvester can be modeled as an ac source with a resistor in series. One of the challenge of this type of transducer is that the integrated prototypes are only able to provide very weak output.

In practice, piezoelectric energy harvesting and magnetic energy harvesting can be used in the same transducer to increase the output power and energy conversion efficiency. Figure 1.12 shows a possible structure with the two harvesting schemes used together. Another idea to enhancing the mechanical energy harvester performance is to use magnetoelectric composites. An example is shown in Figure 1.13. The composites are constructed that they combine piezoelectric and

magnetostrictive phases in turn, and thus have the chance to convert magnetic field into stress and improve the vibration energy harvesting efficiency.

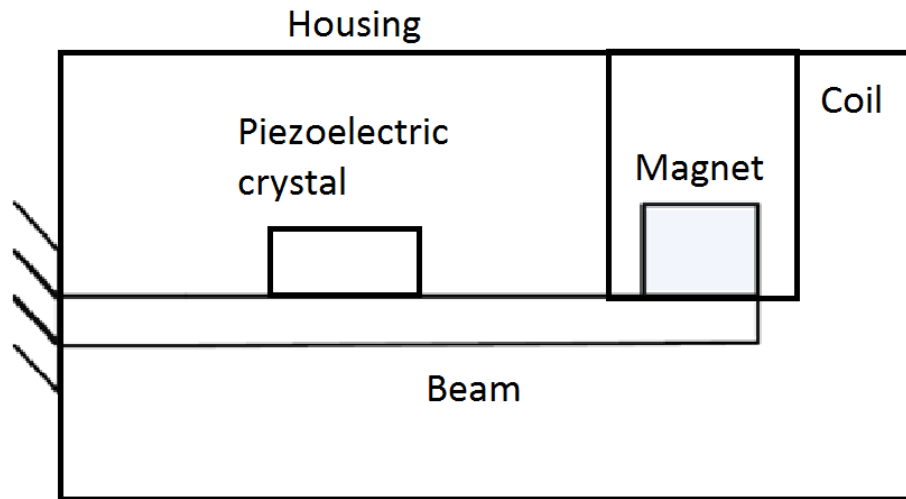


Figure 1.12. Multi-mode mechanical energy harvester using piezoelectric and electromagnetic schemes

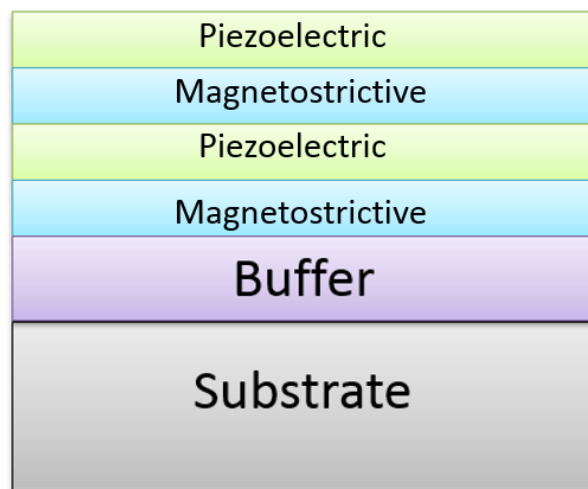


Figure 1.13. Magnetolectric composites in a layer by layer structure

The two most widely used thermal energy harvesting schemes are thermal electric energy harvesters and pyroelectric converters. Thermoelectric devices have been demonstrated successfully on applications such as wireless sensor nodes [23], which rely on temperature gradient in space. They utilize Seebeck effect (basically conversion between temperature differences and electricity), typically containing semiconductors in p and n type alternatively arranged. An example is shown in Figure 1.14. They can be modeled as a dc voltage source with a resistor in series. The p and n type semiconductors have opposite signs in Seebeck coefficients, providing the maximum possible output voltage. The two most common materials for thermoelectric generators are Bi_2Te_3 and Poly-SiGe. Similar to RF energy harvesting, the thermal resistance of the generators have to be matched to that of the source in order to maximize the transferred power.

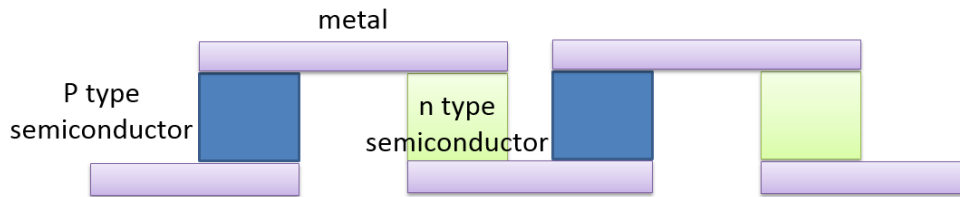


Figure 1.14. An example structure of a thermoelectric harvester

In comparison, Pyroelectric transducer is an alternative energy harvesting method based on temporal temperature gradient. It can be modeled as an ac current source with a capacitor in parallel. The theoretic maximum efficiency of thermal energy harvesting is given as following [3]:

$$\eta = \frac{(T_H - T_C)}{T_H} \quad (1-10)$$

where T_H and T_C refer to the hot and cold temperature respectively. This is also called the Carnot efficiency. The reported efficiencies in literature, however, are usually well below this value. Efficiencies of 0.02 % to 0.05 % of the Carnot value have been reported for Pyroelectric transducers [24], and up to 17 % for thermal electric transducers [25].

Magnetic energy exists near conductors carrying ac current and magnets. This magnetic energy can be converted into electrical energy by an inductor coil. The harvester coil can be modeled as an ac voltage source with an inductor in series [3]. Note that this magnet energy harvesting is different from the electromagnetic mechanic energy harvesting described earlier in this section. According to Ampere's law and Faraday's law, the power generated in this scheme can be expressed as:

$$P = \frac{N^2 A_c^2 \mu_c^2 f^2 I^2}{Zd^2} \quad (1-11)$$

where N is the number of turns of the coil, A_c is the surface area of the coil, μ_c is the permeability of the coil, f is the signal frequency, I is the current amplitude and d is the distance from the source and the coil.

Some other schemes for energy harvesting exploited in the literature include biochemical sources [26] and radioactive sources [27].

1.3 Power Conditioning

There are a number of reasons to condition the power harvested from the ambient. For one, the signal may be in ac form and has to be rectified for further use or storage, and vice versa. What is more, the initial power derived from the environment is usually not usable to load directly because they are too weak to meet the application requirements such as impedance characteristics. Additionally, in order to store the energy the voltage level has to be high enough to recharge a secondary battery cell or a capacitor with initial charge on it. Even if the signals meet the loading requirements, power conditioning can adjust the signal to the minimum that the load needs, and thus reduce the power loss in the system. Therefore, a power conditioning block is necessary in most cases, to modify voltage and current so as to supply the needs of a loading application. Since the majority loading needs are in dc form, such as wireless sensor nodes and battery recharge, the focus in this dissertation will be on conditioners providing dc voltage.

Most of the power conditioning blocks in the literature are based on voltage regulators [3]. There are two main types [28]: linear regulators and switching regulators, while switching regulators include magnetic regulators and charge pumps (non-inductive switching regulators). The efficiency of a voltage regulator is defined as the ratio of the output power to the input power.

The most straightforward way to achieve voltage regulation is to use a linear converter. In this case, the converter will serve as a variable resistor. It can be realized through passive devices such as a Zener diode working in reverse-biased region, or active devices such as metal–oxide–semiconductor field-effect transistors

(MOSFETs) working in linear region. Figure 1.15 shows a typical configuration of a P-channel MOSFET used as a linear regulator.

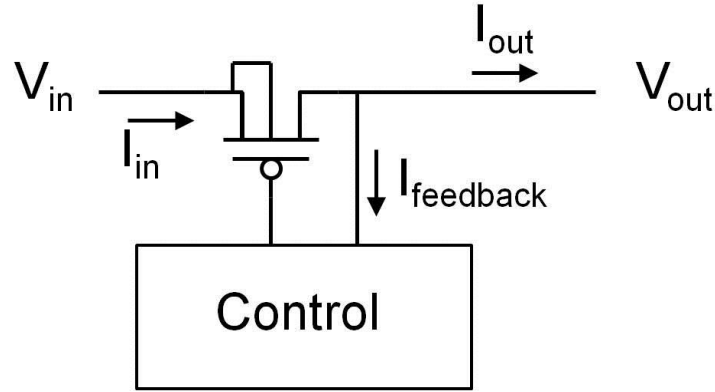


Figure 1.15. Typical linear regulator configuration using PMOS

Switching regulators usually enjoy higher energy transfer efficiency than linear regulators since they tend to have lower power loss [2]. This is because they eliminate the power loss on passive devices (ideal reactance dissipates no power), compared to linear regulators. Magnetic-based switching regulators typically use inductors to transfer energy and capacitors to store energy. The inductor keeps and releases energy in switch controlled cycles. Figure 1.16 shows a typical configuration of a buck converter, which has an output voltage smaller than input voltage. The conversion ratio of this circuit is proven to be [29]:

$$M = \frac{V_{out}}{V_{in}} = D \tag{1-12}$$

where D is the switching duty cycle. A typical boost converter is shown in Figure

1.17 with a conversion ratio of $\frac{1}{1-D}$.

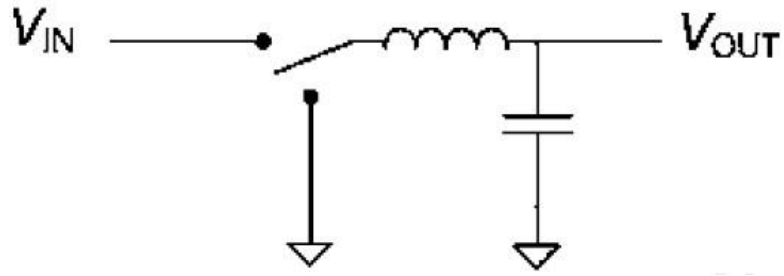


Figure 1.16. A typical illustration of a magnetic switching buck converter

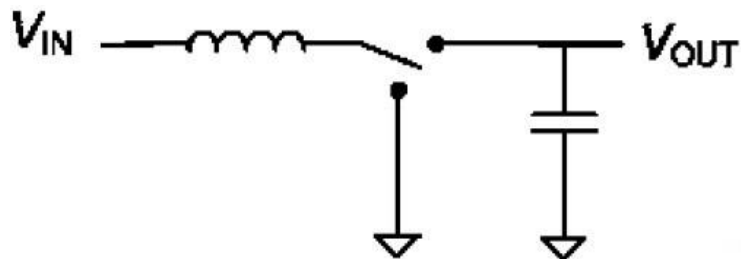


Figure 1.17. A typical illustration of a magnetic switching boost converter

Charge pumps are also called electrostatic switching converters. They typically include capacitors to store charge, and change their configurations by switching in different phases to step up and step down voltages. Their working process is basically through charge transfer. The general idea of boosting is to charge multiple capacitors in parallel in one phase, and connect them in series in another to output a higher voltage. Buck converters share a similar operating principle but they charge the capacitors in series, and shift them in parallel to output. Figure 1.18 shows the typical working process of a boost converter. When a higher boosting ratio is desired, designers usually connect several low gain charge pumps in series to achieve an overall gain of 2^N [2]. In that case, several different clock signals have to be employed to control each converter. The major power losses in charge pumps come from the losses in switches.

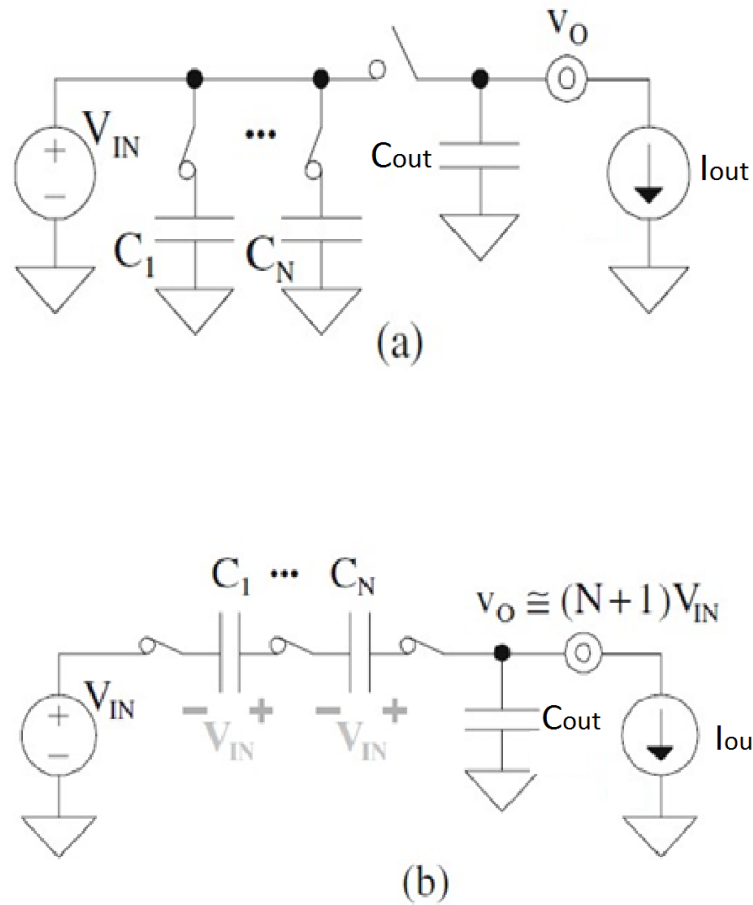


Figure 1.18. A typical working process of a charge pump. In phase (a) capacitors C_1 to C_N are charged in parallel. In phase (b), capacitors are changed into series to output a higher voltage.

Another type of power conditioning converter is the switching ac-dc converters. They are also called rectifiers. A typical configuration is shown in Figure 1.19, which uses diodes to control the current flow and change it to dc form. However, diodes have a threshold voltage needed to conduct. This “threshold” may not be achieved in some low power applications. Also, the voltage drop on diodes, when they are conducting, causes power losses. Designers normally use low power

MOSFETs to overcome these drawbacks, as they usually have a comparatively lower voltage drop when conducting. But additional circuits have to be designed to create clock signals to control them.

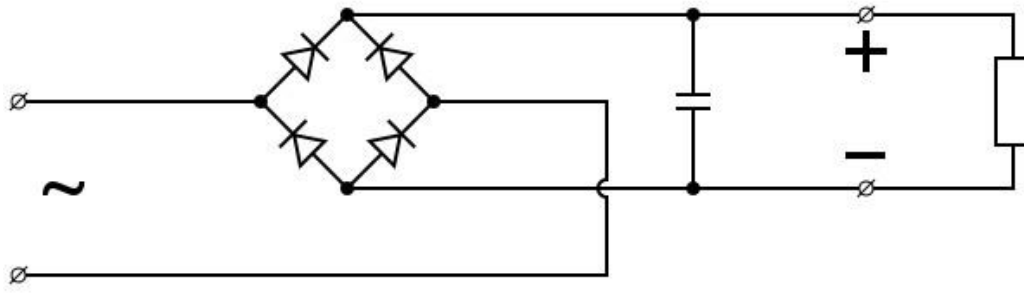


Figure 1.19. A typical configuration of a ac-dc switching converter: bridge rectifier

1.4 Energy Storage

The main energy storage elements in energy harvesting systems are batteries and supercapacitors. There two different types of battery system: primary batteries and secondary batteries. Primary batteries are designed to convert the chemical energy into electrical energy only once, while secondary batteries are reversible energy converters, designed to discharge and charge repeatedly [30]. Consequently, primary batteries are often used for long term storage in low discharge rate applications; on the other hand, secondary batteries are preferred in portable devices. This dissertation focuses on secondary batteries and supercapacitors since they are typical choices for energy harvesting systems.

1.4.1 Batteries

Batteries generate electrical energy by chemical reaction. Each battery typically includes one or more cells, which are electrochemical units connected in series and parallel to create the desired voltage and capacity [3]. And each cell comprises an anode, a cathode and an ionic conductor also known as electrolyte. The electrolyte provides the medium for charge transfer between anode and cathode. There is usually a partition material, called a separator between the two electrodes which is permeable to the electrolyte [31].

A battery cell can be modeled as an ideal voltage source with three passive elements, as shown in Figure 1.20. The voltage source V_B decides the open circuit voltage (OCV). It depends on the charge Q stored in the battery. R_S is the series resistance, which models the ohmic contacts between the electrodes and the current collectors. The capacitor C_P models the double-layer ion concentration effect at the interface of electrodes and the electrolyte, while the parallel resistance R_P represents the various resistance contributed by the electrode-electrolyte system [31].

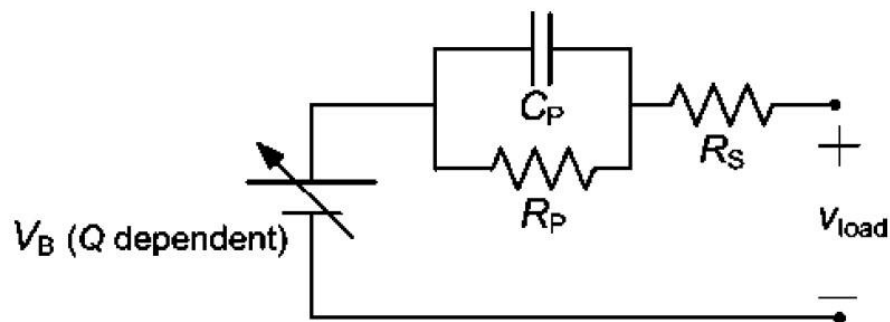


Figure 1.20. A typical battery model

A battery is characterized by a number of parameters, such as the open circuit voltage (OCV), closed circuit voltage (CCV), capacity (in the units of Ampere-hour), energy content (in the units of Watts-hour) and internal resistance. Additionally, energy density can be represented by the weight-related energy in Wh/kg, and the volume-related energy in Wh/L or Wh/cm³. Some batteries also tend to self-discharge, which is a process to lose charge gradually in open circuit state.

The most commonly used secondary batteries fall into two categories: Lithium based batteries (including Li-ion and Li polymer) and Nickel metal hydride (NiMH) [32] [33]. Figure 1.21 shows the volumetric energy density versus the gravimetric energy density for common secondary battery types. The battery used in this dissertation is mainly designed for a high gravimetric energy density because in shape it is thin and flexible. The details of this battery are presented in Chapter 4.

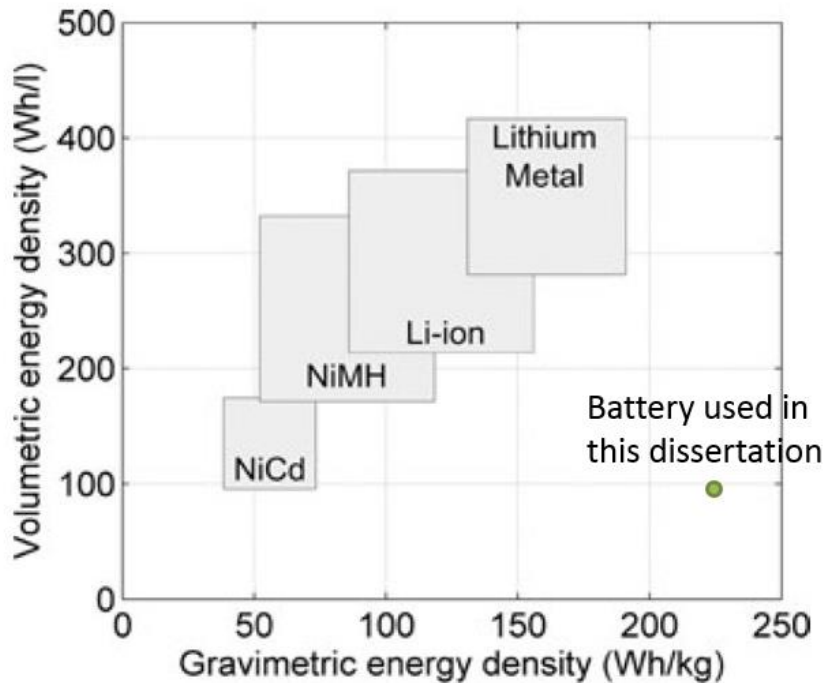


Figure 1.21. Volumetric energy density versus the gravimetric energy density for common secondary battery types [3]

Thin film batteries are designed for integration on silicon wafers using solid-state lithium and they can sustain solder reflow [31]. Several companies have been working on the mass commercialization to solve their limitation in low capacity per area and high-processing temperatures [34]. Thick film batteries, on the other hand, are limited for their solid-polymer electrolyte performance [35].

1.4.2 Supercapacitors

Supercapacitors, also known as ultracapacitors or double-layer capacitors, are electrochemical capacitors with comparatively high energy density. They increase storage density by using nanoporous material, typically activated carbon electrodes that have large surface areas and are separated by short distance [3]. Figure 1.22 shows a typical structure of a supercapacitor. The supercapacitor can be modeled as an ideal capacitor and two resistors as shown in Figure 1.23. R_C represents the series resistance and R_{leak} models the leakage current. C is the terminal-measured capacitance of the cell.

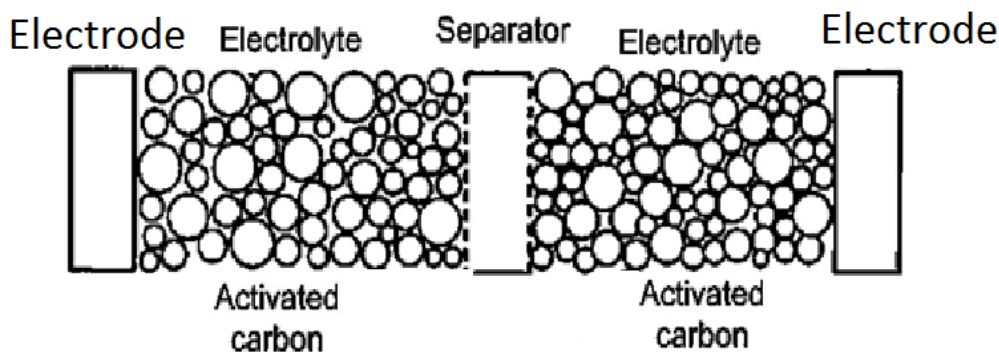


Figure 1.22. Structure of a supercapacitor

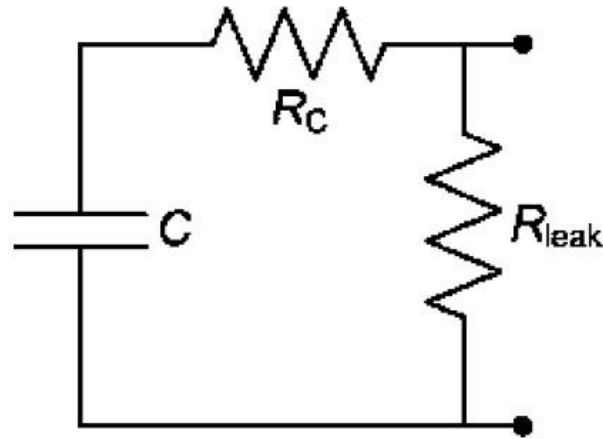


Figure 1.23. Equivalent circuit of a supercapacitor

Compared to secondary batteries, supercapacitors have a smaller energy storage density (about one to two magnitudes lower than a battery). However, they enjoy a higher power density and lower internal resistance. Furthermore, high quality supercapacitors are often expensive. This can be solved by hybrid use of secondary batteries and supercapacitors [36] [37].

1.5 Summary of Open Literature Results on RF Energy Harvesting

A number of reports on RF energy harvesting have been published in recent years. The powering distance ranges from several centimeters to several meters. A typical RF energy harvesting system includes a few basic building blocks: a single antenna or antenna array to receive the RF power wirelessly, an impedance matching network, optional filter and rectifier blocks to modify the power to or from dc, a power conditioning block to adjust the voltage and current as the applications require, and a storage unit to keep the energy for future use. Most of the reports in literature

concentrate on one or a few blocks. On the system level, key parameters include input power level, powering distance and efficiency.

Let us review reports focusing on the system level, as shown in Table 1-1. Umeda et al. achieved 1.2 V to recharge a secondary battery with -14 dBm input power at an efficiency of 1.2 % [38]. Kocer et al. proposed a wireless temperature sensor that recovers power from 450 MHz RF signals from a 7 W base station 18 m away (corresponding to an incident power density of $0.17 \mu\text{W}/\text{cm}^2$) [39]. Also, Paing et al. reported a wireless sensor platform powered by 2.45 GHz RF signal with an incident power density of around $100 \mu\text{W}/\text{cm}^2$ [40]. A silicon wafer-fabricated aqueous Ni-Zn microbattery was proposed in [41] with a RF energy receiver which can deliver more than 3.5 V with input power larger than 18 dBm. The company Powercast claimed their product is able to harvest -11 dBm input power and generate output voltage up to 5 V [42].

Table 1-1. Comparison of the recent research results of RF energy harvesting

Work	Incident level	Frequency	Efficiency [%]	With antenna	Energy Storage
Umeda et al. [38]	-14 dBm	950 MHz	1.2 %	No	Yes
Korcer at al. [39]	-12.3 dBm	450 MHz	N/A	Yes	No
Paing et al. [40]	100 $\mu\text{W}/\text{cm}^2$	2.45 GHz	N/A	Yes	Yes
Singh et al. [41]	Over 18 dBm	2.45 GHz	N/A	Yes	Yes
Powercast [42]	-11 dBm	Narrow band (850 – 950 MHz)	~ 10 %	Yes	No
Jabbar et al. [43]	-5 dBm	400 MHz and 2.4 GHz	3.9%	Yes	No
Li [44]	-19 dBm	900 MHz and 1800 Hz	9%	No	No
This dissertation	30 $\mu\text{W}/\text{cm}^2$ or -5.9 dBm	2 – 18 GHz (Broadband and tested with 900 MHz)	7.7 %	Yes	Yes

A comparison of the recent research results mentioned above is shown in Table 1-1. These reports clearly demonstrate the feasibility of RF energy harvesting. However, most of them do not apply to broad band harvesting, and suffer from low energy conversion efficiency at low input levels. Moreover, some of the reports only focus on the open circuit voltage that they can generate, instead of the output power that the system can deliver or keep into a storage unit. In [38], authors mentioned recharging to a commercially available secondary battery with 1.2 V, but failed to describe the recharge and discharge characteristics as well as the compatibility of the battery cell when used in an RF energy harvesting system. Additionally, it does not have antenna set up for practical use. [42] claims that they have achieved 10% energy conversion efficiency from -11 dBm power level. However, the energy storage solution was not provided and harvesting was conducted in a narrow bandwidth. In [44], a dual band energy harvester that obtains over 9% efficiency for two different bands (900MHz and 1800MHz) at an input power as low as -19dBm. The DC output voltage of this harvester is over 1V under optimized loading conditions. However, further experiments showed that this harvester was not able to drive a large capacitor load or recharge our battery, as will be illustrated in Section 5.9. These considerations led to the design of the switched capacitor converter used in this dissertation. This converter is able to source current under the different loading requirements consistent with a multi-source energy harvester and is compatible with other elements of the PDS. Another similar experiment has been done recently and reported on in the literature. This system generates 12.39 μW of output power for input power level of 316.23 μW [43]. Compared to this work, this dissertation reports an RF energy

harvesting block with a broadband range of 2 to 18 GHz and the block stores the energy into a thin film battery. It is able to harvest energy from a lower input power (254.6 μ W) with a higher efficiency, and it allows for energy storage through the battery re-charge process as well. It has the highest efficiency and lowest input power level among results that have broadband characteristic and energy storage solutions.

1.6 The Proposed Power Distribution System

We propose a Power Distribution System (PDS) that focuses on RF energy harvesting. The RF energy harvesting block includes a wideband rectenna, a DC-DC voltage boost converter, and a supercapacitor/battery hybrid cell block [45]. The block is able to harvest RF energy from a commercially available hand-held communication device at an overall energy harvesting efficiency up to 7.7 %. The block diagram is shown in Figure 1.24 [46]. The rectenna uses low turn on Schottky diodes for rectification, and has a wide band of input frequency [15]. The Cockcroft-Walton capacitor boost converter has been designed and fabricated to meet the multiplication needs of the system [47]. A unique, flexible cell based on ruthenium (IV) oxide/zinc redox chemistry has been developed. It has a low re-charging voltage of less than 1.2 V, which allows the system to harvest the low RF power from the environment [48] [49]. The rectenna was fabricated to receive as much power as possible from the surroundings, and efficiently pass it to the voltage converter. The

voltage converter boosts up the weak RF signal to the level that can charge the thin film battery. The block also demonstrates that the battery can be re-charged from low power RF sources.

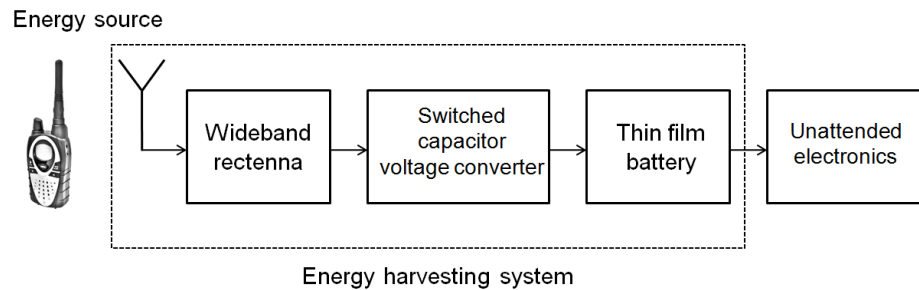


Figure 1.24. Block diagram for the RF energy harvesting block

The system also include a solar energy harvesting block, a USB recharging block, an ultra-low power microcontroller, a voltage regulator to shape the output voltage to stable 3 V, and two secondary battery arrays. Each of the battery arrays contains 4 thin film battery cells. The whole system is completed “stand alone”, potentially receiving energy from the RF source, USB source and solar energy source, storing it in the battery cell, stabilizing the output voltage and driving a variety of unattended electronics. Which source (or sources) the block draws from depends on the local strength of the source. The whole system structure is shown in Figure 1.1.

1.7 Summary of Contributions

- Radio Frequency Energy Harvesting System Design

- Established an energy harvesting system structure that can be applied to a range of energy source scenarios including solar, RF, vibrational, thermal, etc.
 - Analysis of operations and power consumption of a low power switched capacitor voltage converter. Designed and fabricated a six stage switched capacitor dc to dc converter (including an IC version and a PCB version). The chip was fabricated through IBM 130 nm 8RF process.
 - Tested and characterized the converter's performance, clearly demonstrated an energy conversion efficiency up to 40.53 %.
 - Designed and fabricated a broad band rectenna for ultra-low power RF energy.
 - Tested and characterized the broad band rectenna for intended input power levels.
 - Studied and analyzed the battery charging requirements of a ruthenium oxide based flexible battery cell.
 - Design and fabricate a complete RF energy harvesting system with broad band harvesting range and energy storage in a high specific capacity thin film flexible ruthenium oxide battery cell.
 - Demonstrated that a Ruthenium based flexible thin film battery cell can be recharged by a commercially available walkie talkie with an efficiency as high as 7.7%.
- Low Power Distribution System Integration

- Completed a survey of different energy harvesting schemes and system blocks.
- Selected and integrated a commercial solar cell optimally suited to for use with the PDS developed in this dissertation. Demonstrated battery charging with this solar cell PDS integration.
- Designed and implemented a solar cell recharging protection circuit.
- Implemented a USB regulator to recharge the thin film battery from USB source.
- Implemented a voltage regulator to smooth the battery's output profile to provide a constant voltage output.
- Verified, measured and characterized the solar cell converter, the circuit board version of switched capacitor converter, the USB converter and the output voltage regulator.
- Programmed an ultra-low power microcontroller to choose energy sources flexibly, monitor the batteries' potential and control the system operation.
- Integrate an end-to-end power distribution system that is able to harvest energy from different sources and provide stable output to a variety of unattended electronics. The system is completely self-powered, with the capability to select the energy sources smartly and control the system operation efficiently.
- Designed and fabricated a prototype PCB of the power distribution system.

- Provided a complete solution for low power applications to employ ambient energy harvesting as its power source.

- Potential Application Investigation
 - Designed an ultra-low power analog neural oscillator tunable in both frequency and duty cycle.
 - Investigated the typical power consumption of a low power wireless sensor node and assessed it as a load of the proposed power distribution system.
 - Measured and characterized a medical prosthetics system and introduced it as a load to the system.
 - Studied the power consumption of a UAV and presented the improved structure with the system equipped on it as power source.

Chapter 2: Broadband Rectenna Design

2.1 Antenna Overview

An antenna is a required element for harvesting RF energy. It is a device to convert between radiated power carried in an electromagnetic wave and circuit power (voltage and current) at the radio terminals [50]. The antenna operation is based on Maxwell's Equations [51]. In a RF energy harvesting system, the antenna (as a receiver) intercepts electromagnetic waves passing by and convert them into electrical signals.

A typical antenna can be modeled as an ac voltage source a series impedance [52], as shown in Figure 2.1. P_{RF} is the power the antenna received. R_s is the radiation resistance, which stands for the power used for receiving electromagnetic waves. R_{loss} is the loss resistance, representing the actual resistance including the materials of the antenna and dielectric loss. X_{ant} can be either inductive or capacitive depend on the specific antenna.

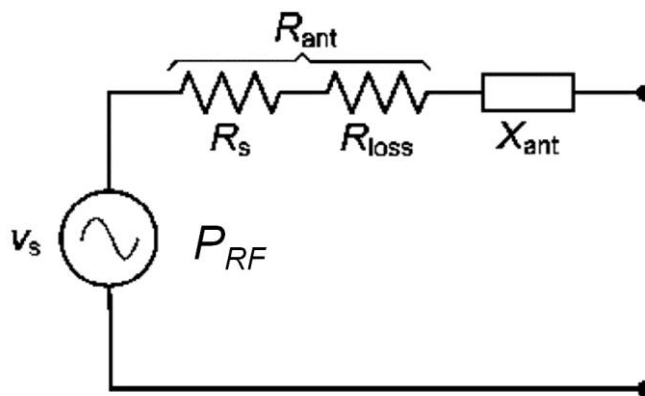


Figure 2.1. Equivalent circuit of an antenna

There are a number of parameters that antenna designers have to pay attention to. Power gain is the ratio of the maximum power density that an antenna can radiate from a certain angle at an arbitrary distance to the power density at the same distance of a hypothetical isotropic antenna. It can be thought of as the actual maximum power density over the ideal (lossless) average power density [50]. The effective antenna aperture is closely related to the available power an antenna can deliver as expressed in the equation (1-2). Some other key parameters include path loss, polarization, efficiency, directivity and so on.

2.2 Design Analysis

A rectenna is a hybrid of an antenna and Schottky diode placed at the antenna feed point. For RF energy harvesting purposes, a broadband dual-circularly polarized spiral rectenna was designed and fabricated based on the previous work of [15]. Its performance relies on Harmonic Balance (HB) analysis, which is performed in the frequency domain of Fourier space and divides the circuit into a linear and a nonlinear part.

Concerning the extreme bandwidth of interest, a frequency independent antenna design is desired. It has been verified that if the shape of an antenna, consisting of a metal in air, is entirely determined by angles, the antenna will be frequency independent because it is invariant to a range of scale [53]. This leads to a logarithmic spiral antenna which is defined by the following equation [51]:

$$r = r_0 e^{a(\varphi+\phi)}, 0 \leq \varphi \leq \phi \quad (2-1)$$

where r and φ are the polar coordinates, a is the expansion coefficient defined as

$\frac{1}{\tan(\phi)}$. ϕ is the arm width, as shown in Figure 2.2. The spiral antenna usually has

two or more arms. The equation applies to each arm. A Schottky diode was used at the feed point, the center of the antenna without matching network. Although the antenna itself is frequency independent, the diode impedance varies with incident power level. However, because of the wide range of input power levels this design is aiming at, it is difficult to design and integrate a matching network for every case. Therefore, the rectifier will achieve an optimum impedance matching only at one incident power level, but mismatch for every other. It would be useful to know the center frequency at a given power level to increase efficiency by modifying the antenna shape and adding a matching network.

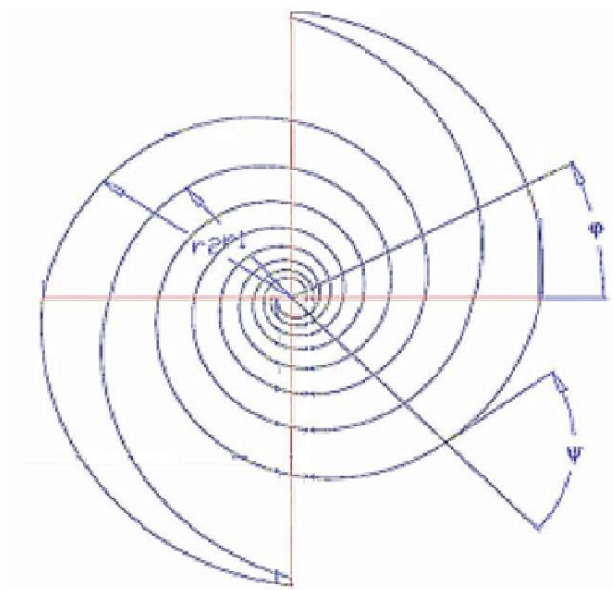


Figure 2.2. Shape of a designed single spiral antenna

Since the input RF power is usually very low, rectenna arrays are employed to achieve larger surface area and as many as possible polarizations. The basic array is 2 by 2, in which two rectennas are connected in series as a group, and two groups are connected in parallel. So the DC impedance is the same as a single rectenna. One pair is placed to receive left hand circular polarization, and the other pair to receive right hand circular polarization.

Finally, a 4 by 4 rectenna array is implemented with 4 of the 2 by 2 arrays in parallel. Each block differs in its orientation by $\frac{\pi}{2}$ from the predecessor to achieve horizontal and vertical polarizations for low frequencies [15]. A photograph of the designed rectenna is shown in Figure 2.3.



Figure 2.3. The designed broad band rectenna

2.3 Rectenna Fabrication and Testing

The Schottky diode chosen to integrate with the antenna is SMS7630 with package SC-79 from Skyworks Solutions Inc. The device is known for its high conversion efficiency and insensitivity to mismatch [54]. The diode parameters are shown in Table 2-1 as given in the manufacture's datasheet.

Parameter	SMS7630
I_s / A	$5 \cdot 10^{-6}$
R_s / Ω	20
N	1.05
TT / s	$1 \cdot 10^{-11}$
C_{j0} / pF	0.14
V_j / V	0.34
M	0.40
E_g / eV	0.69
XTI	2
F_C	0.5
B_V / V	2
I_{BV} / A	$1 \cdot 10^{-4}$

Table 2-1. Parameters of Schottky diode SMS7630

During the fabrication, a square piece of PCB is used that had copper plating on both sides. One side of the PCB was coated with photoresist. The mask used was a pattern reprinted on transparency several times to block any UV light from coming through. The mask was then overlaid on the PCB, exposed to UV light and then developed out. The PCB with the pattern overlay was then etched with ferric chloride, leaving behind the patterned rectenna array.

The rectenna was tested under an input signal of 900 MHz and 0.03 mW/cm^2 power density. This RF power source was used later as the input of the energy

harvesting system. A load of 102Ω was used at the rectenna output. The test yields an energy conversion efficiency of 19.4 %. Also as stated in [15], the antenna achieves a power efficiency of 20 % when the incident power density reaches 0.07 mW/cm^2 . It also characterized a frequency range of 2 – 18 GHz with single-tone and multitone incident waves. This frequency range was not further verified because of power source restrictions. Details of design and fabrication of the rectenna can be found in [15].

Chapter 3: Switched Capacitor DC – DC Converter Design

3.1 Power Loss Analysis of the Switched Capacitor DC - DC Converter

As mentioned in Chapter 1 Section 1.3, switched capacitor (SC) voltage converters (also known as electrostatic switching converters or charge pumps) are converters that periodically switch capacitors to realize voltage step-up, step-down or some combination. An ideal model of an SC voltage converter is shown in Figure 3.1. R_O is the output impedance and R_L represents the load. They do not employ inductors in energy transfer process, and therefore enables simpler and more compact design. They usually have a higher efficiency than linear regulators since they don't suffer from power loss in passive devices. The reason we chose a SC voltage boost converter is that it is able to generate a desired voltage level, and at the same time store the charges in the component capacitors as well, providing a better driving ability for supercapacitors and batteries than the regular resonant voltage converters. However, they still have both static and dynamic power loss, which eventually determines their efficiencies at a given load.

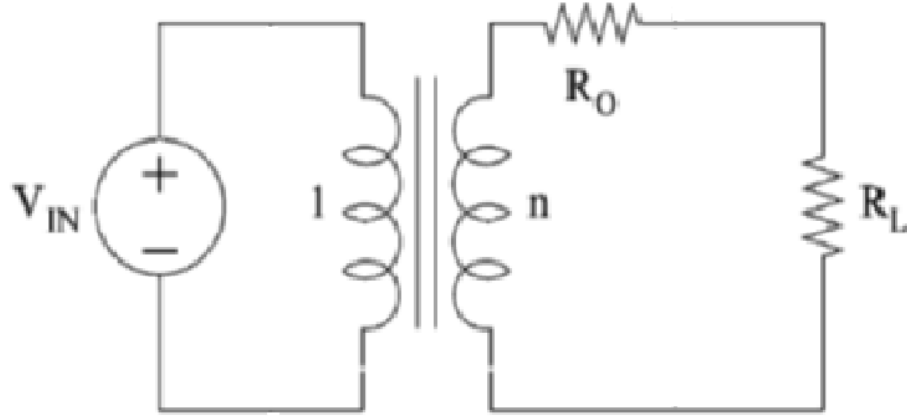


Figure 3.1. Ideal model of a SC voltage converter

The major power loss of an SC voltage converter occurred in the connecting switches [2]. Typically, the more stages the design has, the more energy lost there will be. Consider the energy transfer process in Figure 3.2. Assume in phase (a), as shown in Figure 3.2 (a), the input source charges up the capacitor C_P because there is a voltage difference ΔV . The energy increase on capacitor C_P is:

$$\Delta E_C = 0.5C_P[V_{IN}^2 - (V_{IN} - \Delta V)^2] = C_P V_{IN} \Delta V - 0.5C_P \Delta V^2 \quad (3-1)$$

where ΔV is the voltage change on C_P . While the energy provided by the source is:

$$\Delta E_{IN} = V_{IN} i_{IN} t = V_{IN} Q_C = V_{IN} C_P \Delta V \quad (3-2)$$

where t is the charging time, i_{IN} is the effective charging current for simplicity, and Q_C is the new charge stored in C_P . So the energy loss in the switch is just the difference between the two:

$$\Delta E_{loss} = \Delta E_{IN} - \Delta E_C = 0.5C_P \Delta V^2 = 0.5Q_C \Delta V \quad (3-3)$$

Similarly in phase (b), when C_P discharges as in Figure 3.2 (b), the energy loss on the switch is $0.5Q'_C \Delta V$, where Q'_C is the charge transferred in phase 2.

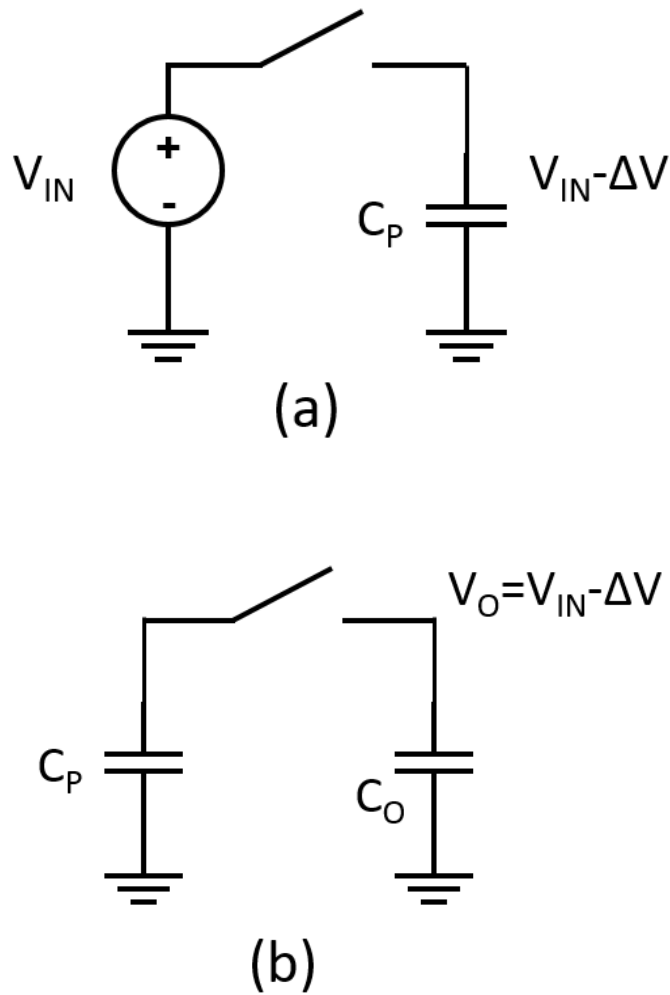


Figure 3.2. Illustration of energy loss in switches in switched capacitor converter

There are some other forms of energy losses in SC converter. For example, conduction losses are the energy lost as heat dissipated on the switches' turn-on resistors. Dynamic loss at the switching point is another important factor. Also, gate-drive losses happen when charging and discharging the transistor gates. It can be calculated as follows:

$$P_{GD} = v_C i_C \left(\frac{\Delta t}{T}\right) = \Delta V_C \left(C_G \frac{\Delta V_C}{\Delta t}\right) \left(\frac{\Delta t}{T}\right) = \Delta V_C^2 C_G f \quad (3-4)$$

where v_C and i_C stand for the voltage and current of the gate, respectively. Δt is the charging time of the gate, T is the switching period. ΔV_C is the difference between gate voltage and high level of clock signal. C_G is the effective capacitance of the gate and f is the switching frequency. The equation indicates that the energy loss is proportional to the switching frequency and gate capacitance.

3.2 Circuit Structure

An SC boost voltage converter was designed and fabricated using the IBM 8RF LM 130 nm CMOS process with 6-2 metal option [47]. Figure 3.3 shows the schematic of the converter in three stage illustration. The design includes all the switches for a six-stage converter, except for the external capacitors. This provides a maximum available output voltage seven times the input voltage through the external capacitors, and a user can select the output multiplication factor from the minimum (1x input) to the maximum (7x input) by connecting an external electrolytic capacitor's positive pad to the output. In the schematic, the top switches are made from nMOS transistors only, but the middle and bottom switches are made using transmission gates (combinations of nMOS and pMOS transistors) to transfer the accumulated potential on each capacitor to the next stage with the least loss. The input can be used in both phases without any wait or sleep modes of operation.

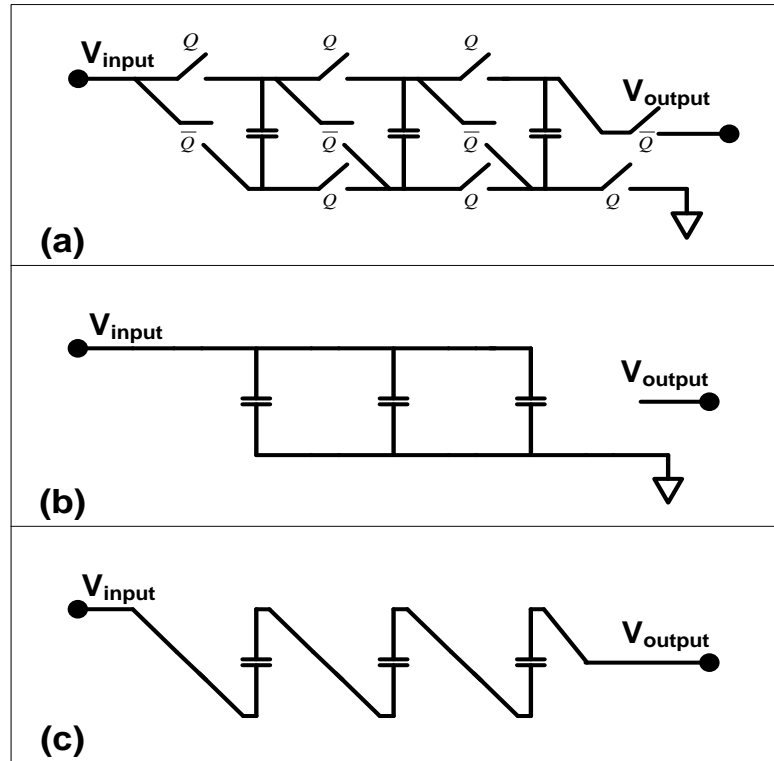


Figure 3.4. Operations of switched capacitor voltage converter

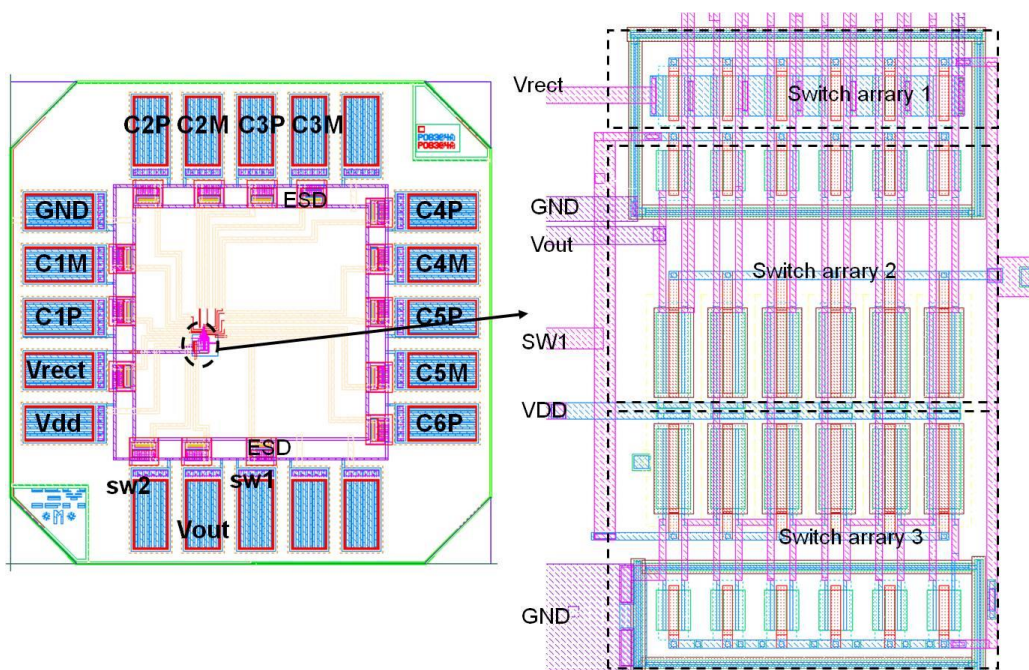


Figure 3.5. Layout of the SC voltage converter

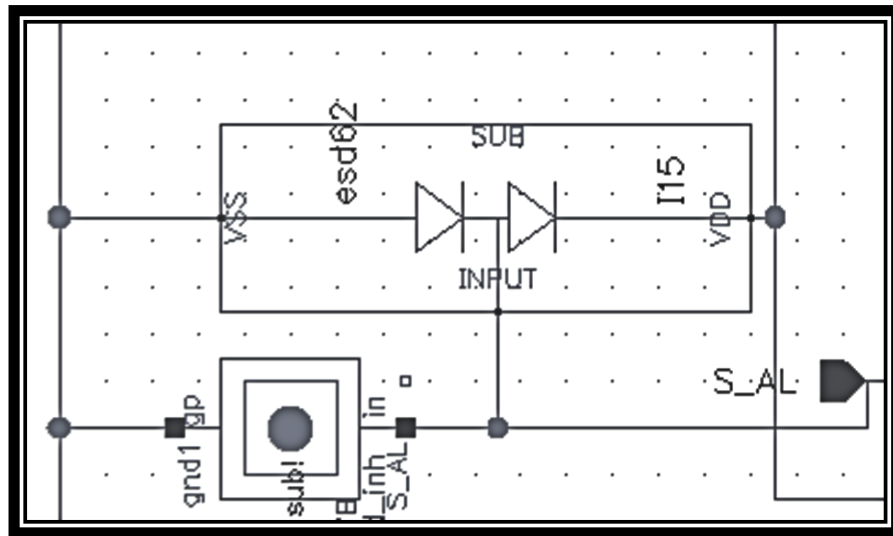


Figure 3.6. Electrostatic discharge protection on pad

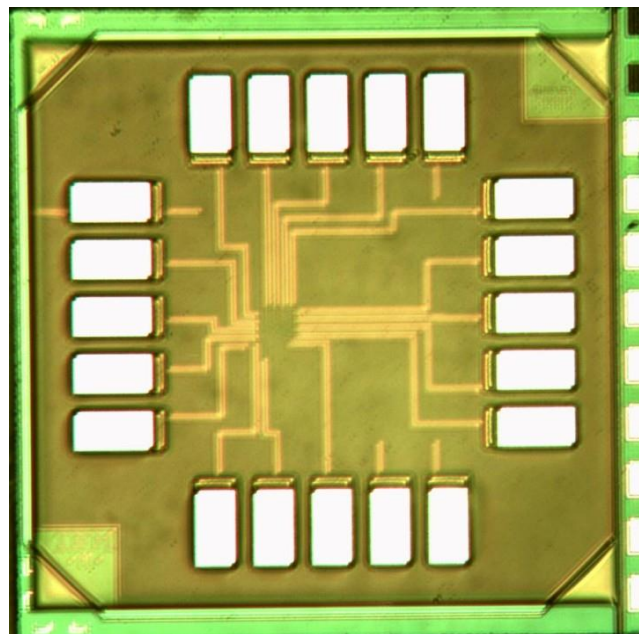


Figure 3.7. Photograph of the SC voltage converter

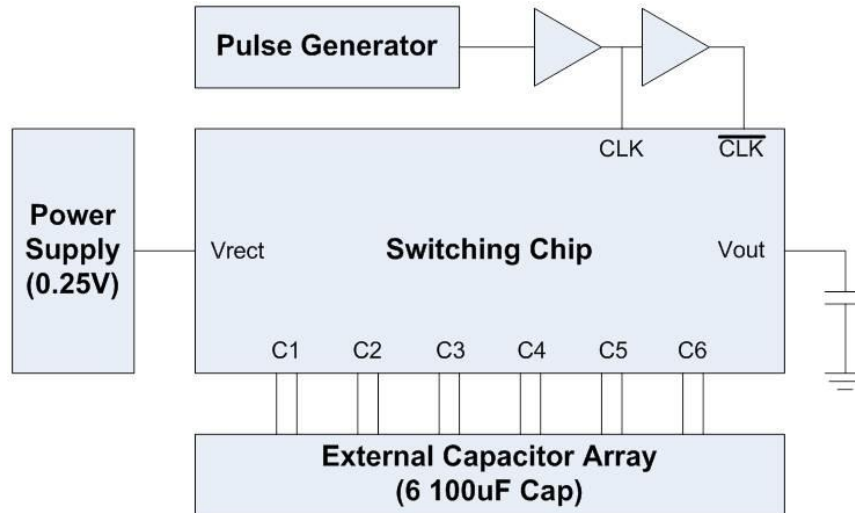


Figure 3.8. Block diagram of the SC converter chip at work

3.3 Simulations and Experiments

3.3.1 Basic Function verification

First, a simple test was performed to verify the basic functions of the SC voltage converter. Figure 3.9 shows the output waveform of a three-stage converter for a 0.35 V input at 20 Hz clock signal using 100 μ F three external capacitors. As analyzed in Section 3.2, the output (around 1.4 V) is four times the input signal. The PMOS body contacts in converter switches are connected to an external 1.5V DC power supply.

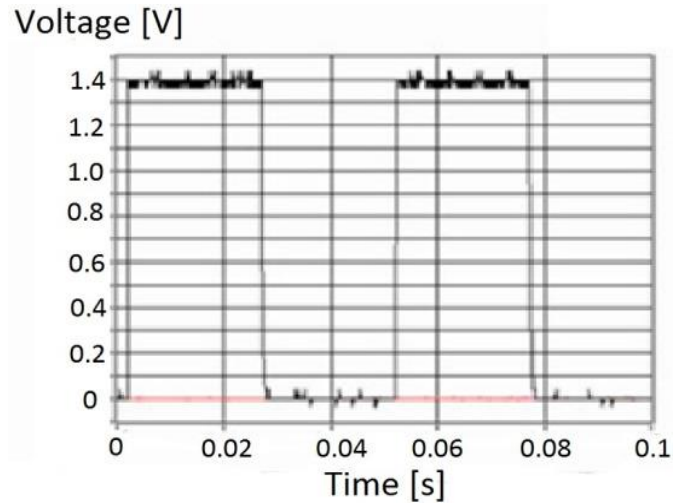


Figure 3.9. Three stage converter operation for 0.35 V input at 20 Hz switching using 100 μF external capacitors

3.3.2 Capacitive Load Charging Simulations and Experiment

A 100 μF capacitor was connected as a load to the SC converter. The SC converter used 0.25 V input with five stage boosting and 1 Hz clock signal. The external capacitors used for the SC converter are also 100 μF . The simulation results of this configuration are shown in Figure 3.10. The left figure shows the whole charging process, and the right one is magnified version of the curve. It shows that the voltage increases by ripples because of the switching nature of the converter. Figure 3.11 is the measurement results of the semiconductor parameter analyzer HP4156B. The load voltage increases similarly, with a minor difference in the final voltage. This could be related to the self-discharge of the load capacitor and the non-idealities of the converter capacitors. Again, the right hand side figure shows the magnified version of the charging curve.

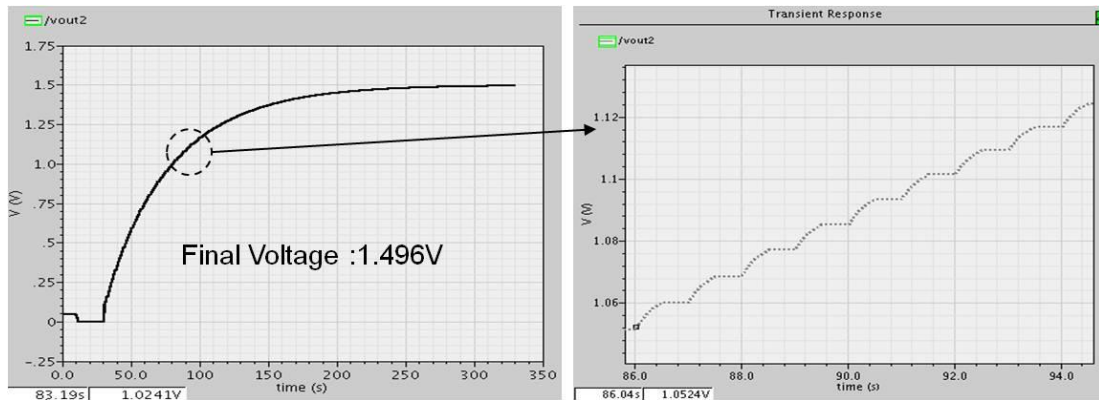


Figure 3.10. Simulation results of load voltage in 100 μF capacitor charging

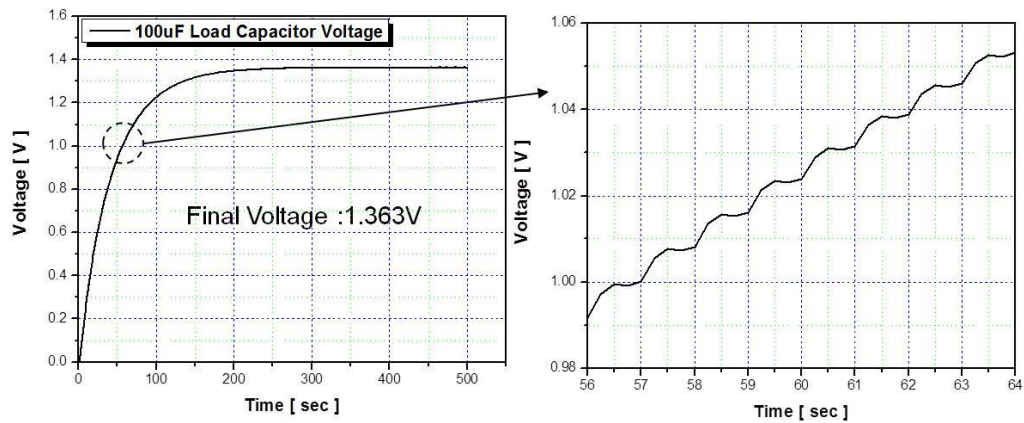


Figure 3.11. Experiment results of load voltage in 100 μF capacitor charging

At the input end, the rectified voltage is 0.25 V. The input current was simulated in Cadence and measured by Agilent 34410A Multimeter in LABVIEW. The simulation results are shown in Figure 3.12. It indicates that as the load voltage increases during the charging process, the input current decreases in average. It is due to that as the voltage difference between the load and the SC converter output decreases, the charge transferring process becomes slower, which further decreases the voltage difference between the input and the converter capacitor and decreases the

charging current. The right figure is a magnified version of the input current, which shows regular pulses with respect to the switching frequency. The measurements are shown in Figure 3.13, with similar results to the simulations. But the current values are more irregular. Part of the reason for this may include the presence of noise in the environment, since the current values are generally small and sensitive to external pick-up.

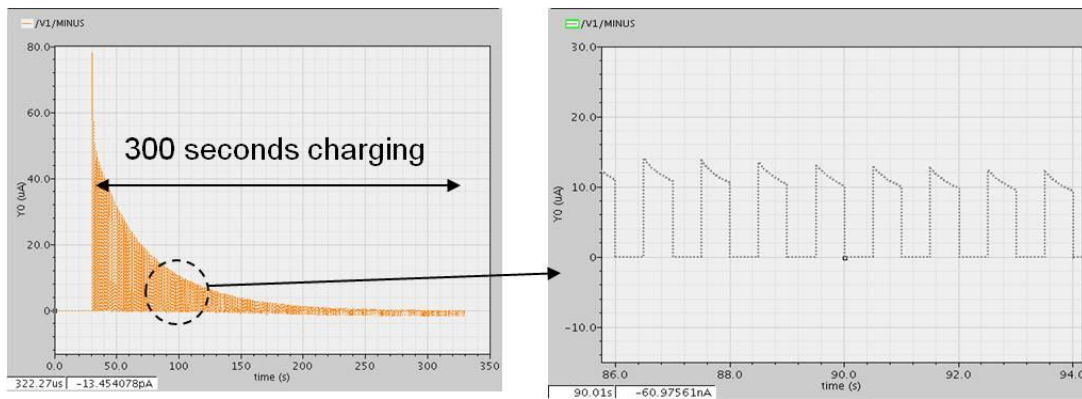


Figure 3.12. Simulation results of input current in 100 μF capacitor charging

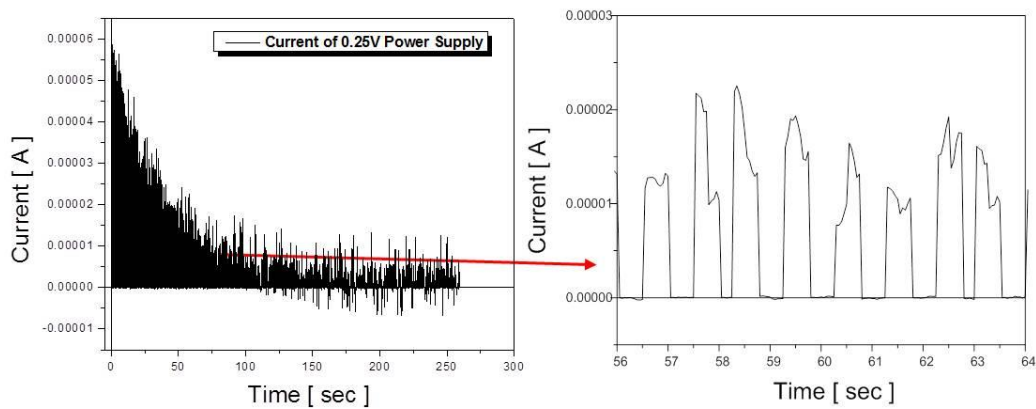


Figure 3.13. Experiment results of input current in 100 μF capacitor charging

3.3.3 Frequency Dependency Experiments

A large capacitor (1000 μF) was used as a load to check the frequency dependency of the SC voltage converter. Here, the converter only used three stages. Also, a number of different clock signal (provided by external signal generator) frequencies ranging from 0.2 Hz to 20 kHz with a 50 % duty cycle have been tested to find the optimum frequency. The external capacitors are 100 μF and the input voltage is 0.35 V. The results with different clock frequencies are compared mainly by their efficiencies and charging speed.

The supplied energy was calculated as:

$$E_{Consumption} = \int_{t_0}^{t_1} V(t) \cdot I(t) dt \quad (3-5)$$

where in this case, $V(t)$ is constantly 0.35 V from the input power supply. The current was integrated from t_0 to t_1 , which is the time of the whole charging process. The energy consumed in the MOSFETs' bodies and gates are neglected in the calculation because they are several magnitudes smaller than the input energy. Therefore, the efficiency of the converter is defined as:

$$\text{Energy Transfer efficiency} = \frac{E_{load}}{E_{consumption}} \times 100\% \quad (3-6)$$

where E_{load} is the energy stored in the load capacitor, calculated by $\frac{1}{2} C \cdot V^2$.

Figure.3.14 shows the results of measurement, and the inner graph is a magnified version of 400 - 700 second section segments of the charging period. All tests are stopped when the capacitor voltage reaches 1.38 V. The plots for the 2 Hz, 20 Hz, and 200 Hz tests show similar charging curves, indicating minimal frequency

dependence for the range of frequencies used. As shown in Table 3-1, the 0.2 Hz, 2 Hz and 20 Hz test have almost the same results for energy transfer efficiency approximately 40 %, for a charging time of about 10 minutes.

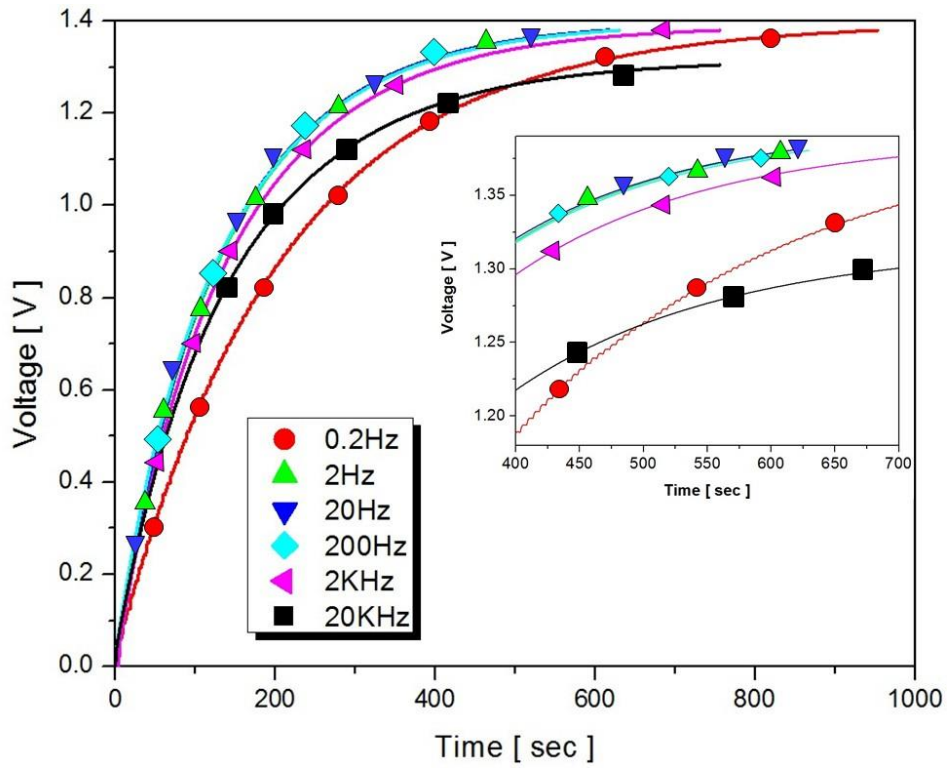


Figure 3.14. Frequency dependency of 1000 μF capacitor charging with 0.35V input and three 100 μF external storing capacitors

Table 3-1 Frequency Dependency of the converter in the 1000uF capacitor charging

Clock Frequency [Hz]	Charging Time [sec]	Supplied Energy [mJ]	Stored Energy [mJ]	Energy Transfer Efficiency [%]
0.2	953.5	2.352	0.952	40.48
2	611.5	2.349	0.952	40.53
20	617.5	2.394	0.952	39.77
200	629.5	2.555	0.953	37.30
2K	755.5	2.755	0.953	34.59
20K*	755.5	3.010	0.852	28.31

As shown in the figure, as the clock frequency goes higher, the saturation voltage goes lower. This is the result of the frequency dependency of the dynamic power consumption of CMOS switches [55]. As a result of these tests, a 2 Hz – 20 Hz clock frequency range was used for further charging tests.

Chapter 4: Energy Storage Solution: A Supercapacitor/Battery

Hybrid Cell

4.1 Cell Overview

Ultrathin galvanic cells are of technological importance because they can comply with a variety of form factors and electronic system packages, and have shown promise for flexible electronic systems [49]. Research toward developing flexible power sources was triggered by the various potential applications of flexing or “wearable” electronic devices [56].

A lightweight flexible thin film galvanic cell has been developed using monoparticulate films of activated carbon and ruthenium (IV) oxide, as the cathode, and spray deposited zinc, as the anode [48] [49]. Referring to this system as a supercapacitor/battery hybrid cell is justified by the observation that it provides the desired properties of both capacitors and galvanic cells in a power delivery system. Specifically, it enables burst energy delivery, upon demand, and long term power delivery, as well.

The battery provides several other advantages for energy harvesting system applications. First, it has the highest specific charge storage capacity per unit area of any commercially available thin film cell ($84.4 \text{ mAh}\cdot\text{cm}^{-2}$ over projected electrode area). Also, the typical re-chargeable battery cells require relatively high re-charge voltages. Li-ion batteries for example, typically operate at 3.6-3.7 V, and require over 4 V to re-charge. The cell described here can be re-charged at an exceptionally low voltage of 1.2 V (which is the open circuit voltage of the battery after being fully

charged), meeting the low voltage requirement of RF energy harvesting [57]. Given that a series of voltage up-conversions is both inefficient and affected by parasitic losses, this requirement constitutes a major barrier to implementing RF charging [58]. Furthermore, the battery is less than 0.5 mm thick (prior to the optimization of packaging materials), and flexible and can be fabricated under \$20 per square meter.

The cathode in this system is hydrated Ru (IV) oxide, which is a material with several unique capabilities [49]. Firstly, $\text{RuO}_2 \cdot n\text{H}_2\text{O}$ is a mixed proton–electron conductor that can generate ultra-high pseudo capacitance [59] [60]. Secondly, it exists in a multiplicity of oxidation states to allow grace discharge profile which is suitable for low power applications. Also, hydrated Ru (IV) oxide enables easy construction of hybrid power sources of batteries and supercapacitors. Specifically, a $\text{RuO}_2 \cdot n\text{H}_2\text{O}$ cathode with a metallic anode can operate as a battery, while two identical $\text{RuO}_2 \cdot n\text{H}_2\text{O}$ electrodes can serve as a supercapacitor. Finally, $\text{RuO}_2 \cdot n\text{H}_2\text{O}$ exists as nano-powder with a large specific surface area, which facilitates the electroactive process. Figure 4.1(A) shows the schematic of the assembled cell. Different parts of the cell are listed in the figure caption. Figure 4.1(B) is an illustration of the flexibility of the battery.

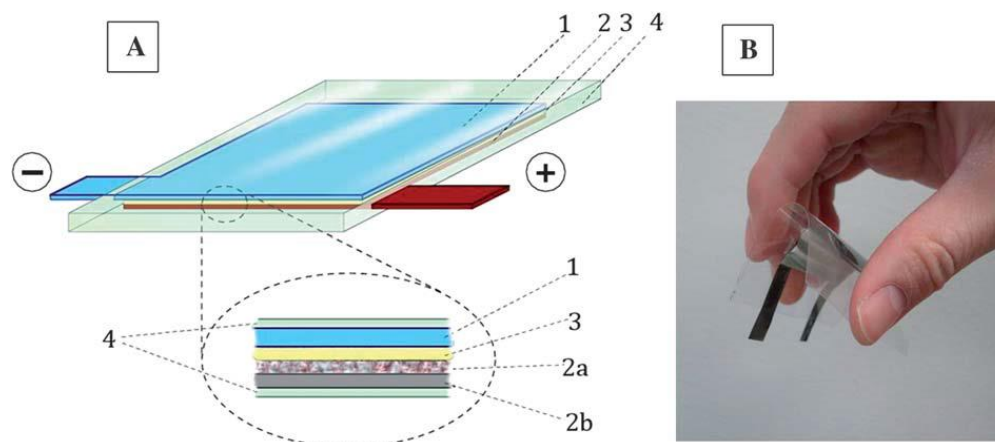
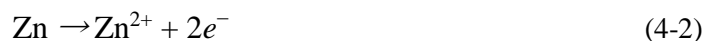


Figure 4.1. (A) Cross-section of the single-sheet Zn-RuO₂·nH₂O galvanic cell: 1—Zn anode; 2—RuO₂·nH₂O /activated carbon cathode, where 2a—paste containing Ru(IV) oxide nanoparticles and 2b—graphite film current collector; 3—separator; 4—packaging and sealing materials. (B) Photograph of an assembled ultrathin cell [49].

The simplified chemical reaction in the cell is governed by the following equations [48]:



The oxidation state of ruthenium changes from 4 to 2 by adding two electrons and protons. An oxidizable counter electrode provides the anode reaction. Metallic zinc was used in the cell, providing the electrons to form the current flow.

4.2 Electrical Characteristics of the Battery

The batteries were tested for specific charge capacity, cycle life and self-discharge current leakage. Figure 4.2 shows the discharge curve for a 4 cm² thick film RuO₂·nH₂O cell. It was connected to a 1 kΩ load and the final voltage was 20 % of

the maximum value. The capacity reached $50 \text{ mAh}\cdot\text{cm}^{-2}$ as the maximum and $25 \text{ mAh}\cdot\text{cm}^{-2}$ before the voltage dropped below 0.8 V . Additionally, the internal leakage current was measured using the method described in [61], and found to be less than 100 nA . Figure 4.3 shows the discharge curve of a thin flexible single sheet Zn - $\text{RuO}_2\cdot n\text{H}_2\text{O}$ cell with a 500Ω external load. It has an approximate thickness of 1 mm including package and an active electrode area of 9 cm^2 . The total charge the battery delivered is 760 mAh , corresponding to a specific capacity of $84.4 \text{ mAh}\cdot\text{cm}^{-2}$.

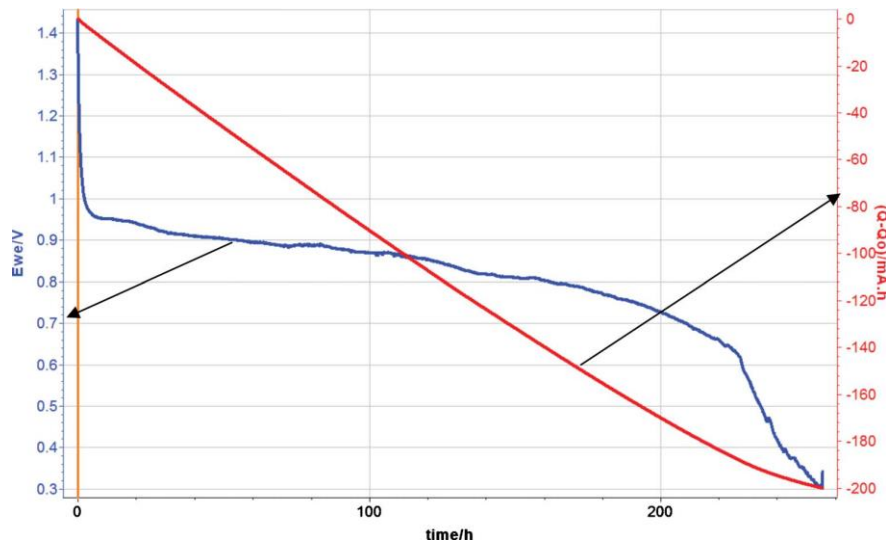


Figure 4.2. Discharge curve of a thick film $\text{RuO}_2\cdot n\text{H}_2\text{O}$ galvanic cell over $1 \text{ k}\Omega$ load. Blue curve shows the cell voltage and red curve shows the capacity [49].

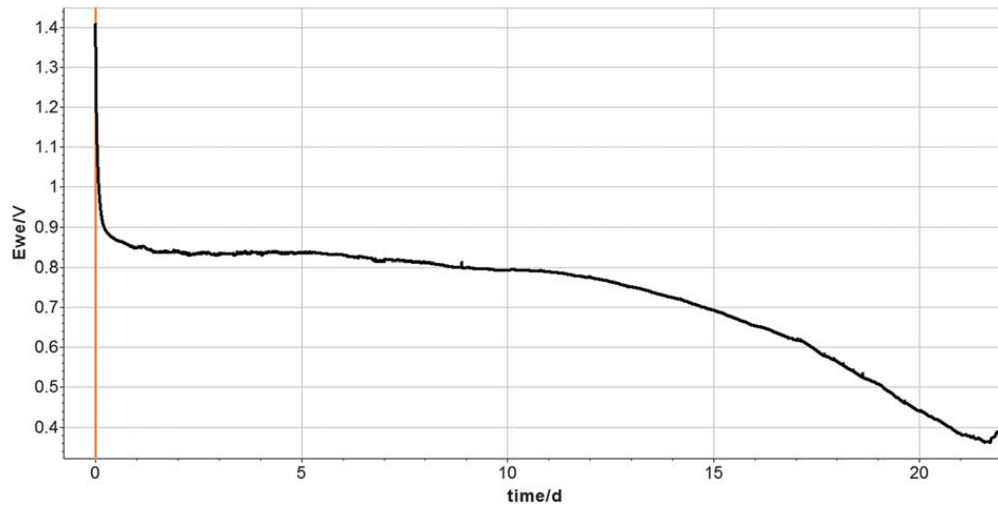


Figure 4.3. Capacity monitoring for a representative thin and flexible Zn–RuO₂·nH₂O galvanic cell [49].

Figure 4.4 displays a life cycle test of the battery cell. In the experiment, the battery was discharged over a 10 Ω load for 1 minute, and recharged at 1.25 V for another minute. A total of 800 such cycles are shown in the top figure. The bottom left figure shows the early cycles and the bottom right shows the later ones. The burst energy supply capability is illustrated in Figure 4.5. A 1 cm² cell was discharged in a short circuit and maintained current over 20 mA for more than 2 min. Table 4-1 shows a comparison of the specific capacity and recharge voltage between this galvanic cell and several commercially available thin film rechargeable batteries.

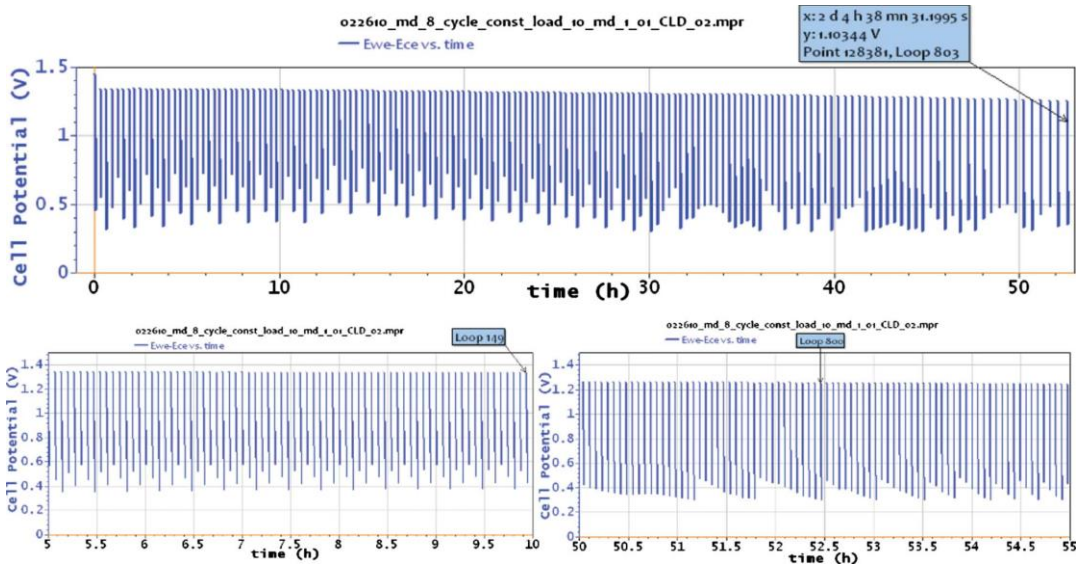


Figure 4.4. Life cycle test of the battery cell. Top figure shows a total of 800 cycles. Bottom left shows the early cycles. Bottom right shows the later cycles [48].

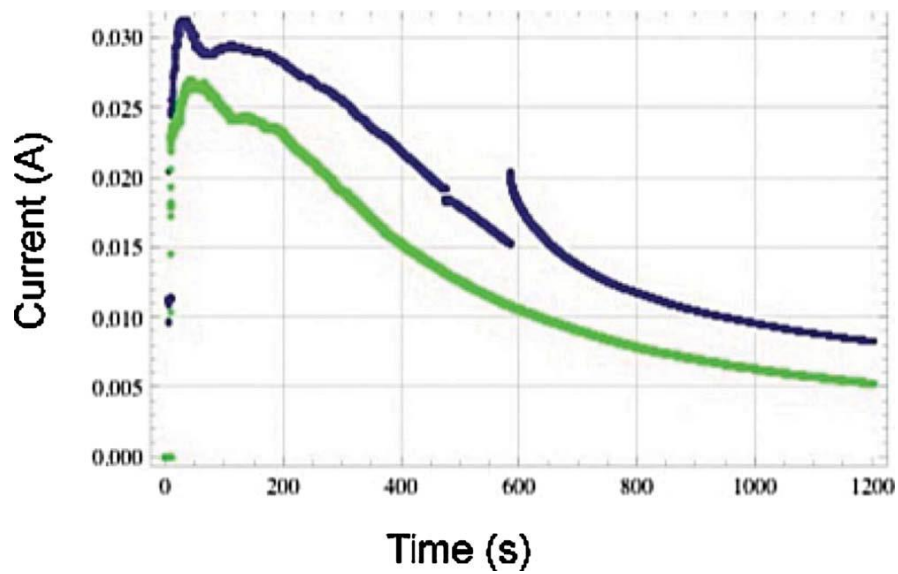


Figure 4.5. Burst discharge capability of a 1 cm² battery cell [48].

Table 4-1. Comparison between the reported battery cell and commercially available rechargeable thin film batteries

Galvanic cell	Source	Specific capacity (mAh/cm ²)	Recharge voltage (V)
Zn/RuO ₂ ·nH ₂ O	Present work	25 (before cell voltage drop below 0.8 V)	< 1.25 V
C/LiCoO ₂	Manufacturer A	1.5	> 4.0
	Manufacturer B	0.080	
	Manufacturer C	0.050	
	Manufacturer D	0.030	
C/LiFePO ₄	Manufacturer E	0.47	

The discharge profiles of the battery cells demonstrate distinct regions of operation. Figure 4.6 shows the first 40 hours of a thin film battery's discharge curve over a 1 K Ω load. The initial region of the discharge curve (blue) is a mixture of capacitive behavior and cathode material reduction. The capacitance of the battery can be modeled by fitting an RC-transient curve (red) to this portion of the discharge data, so an estimate of the capacitance could be obtained. This test has been performed across a range of cells to obtain capacitances ranging from 1.78 F to 4.63 F.

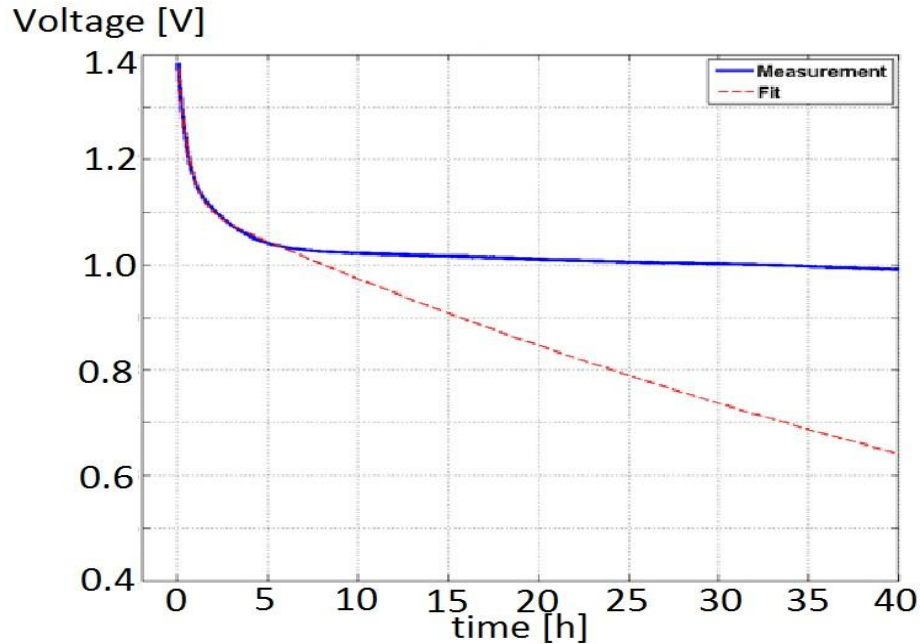


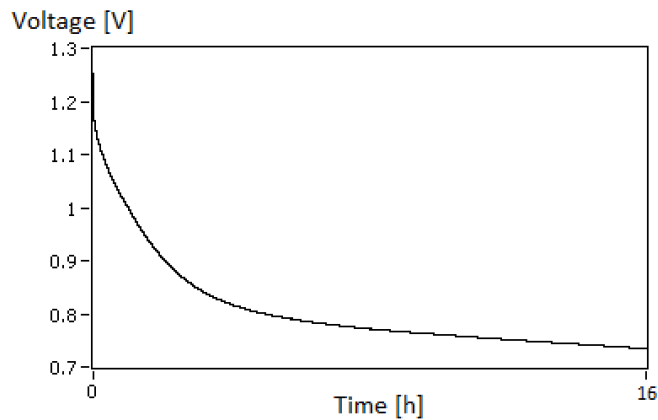
Figure 4.6. First 40 hours of a battery’s discharge curve. The RC-discharge profile fit to the capacitive region of the battery operation

4.3 Battery Recharge Experiment with SC Voltage Converter

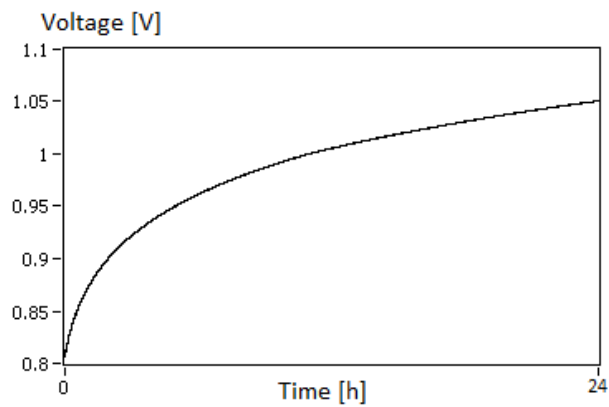
The battery’s recharge capability was further tested by using signals from the SC converter (analyzed in Chapter 3) as input. This re-charge test includes three steps at follows: 1) initial discharge, 2) recharge, 3) second discharge. The first discharge consumes part of the battery’s energy to prepare for the recharge process. From the second discharge, the change in potential after the converter charges the battery can be observed, by comparison with the first discharge.

The battery was discharged through a 1 k Ω load for 16 hours at first. As shown in Figure 4.7(a), the load voltage dropped from 1.171 V to 0.735 V. Note that by using a battery with a lower initial voltage, this discharge time can be reduced. The following recharging test was set up with a 0.25 V input from external power

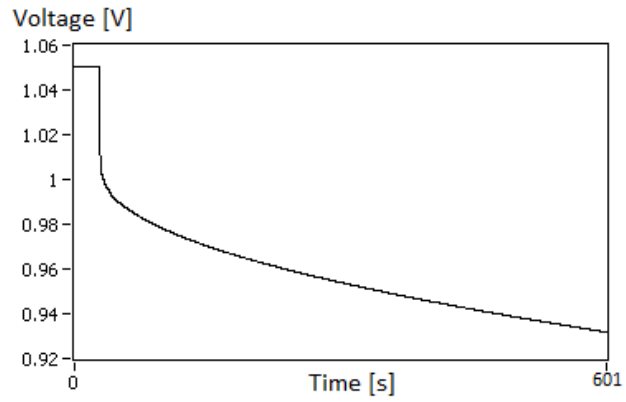
supply, and six 100 μF external storing capacitors for a six stage converter. This gave a 1.75 V open circuit output. A 50 % duty cycle and 1 Hz clock signal were implemented to control the charging process. The battery was recharged for 24 hours. Figure 4.7(b) shows the increasing potential during recharging. Then the battery was connected to the 1 k Ω load again for 10 minutes in order to monitor the potential change. As shown in Figure 4.7(c), the battery started to provide energy from 1.002 V. Compared to the load voltage before charging (0.735 V), the results demonstrated that the DC-DC converter is working properly and is able to recharge the battery.



(a)



(b)



(c)

Figure 4.7. Results of the battery cycle test. (a) Discharging test results for 16 hours (1 K Ω load), (b) Potential change during 24 hours charging (0.25 V input, 1 Hz clock signal), and (c) 10 minutes discharging after charging (1 K Ω load).

Chapter 5: Power Distribution System Integration

5.1 Solar Energy Harvesting Block

As discussed in Section 1.2.1, solar energy has the greatest availability compared to other energy sources. It has been commercialized in numerous fields and still has a large potential market. Therefore, the system reported here implemented a solar energy harvesting block as one of its energy sources. The solar cell used here is from Solarmade with the model number 3-1.5-100. Under full sun conditions, it has an open circuit voltage (OCV) of 1.5 V and a short circuit current (SCC) of 100 mA [62]. A photo of the model series is shown in Figure 5.1.



Figure 5.1. Photograph of solar cells used in the system

The battery cells described in Chapter 4 are able to operate normally when they are recharged to 1.4 V. Significant damage has not been observed in the experiment in terms of overcharging. However, charging protection circuit is still designed here in solar energy harvesting block. The circuit uses a feedback loop involving an operational amplifier. The circuit diagram is shown in Figure 5.2.

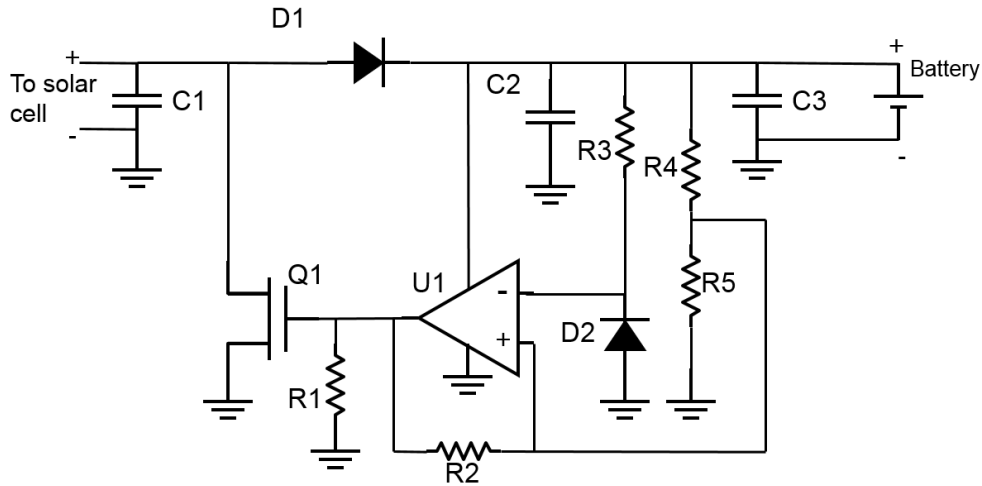


Figure 5.2. Solar cell recharging protection circuit diagram

D1 is a Schottky barrier diode with a low turn on voltage of 0.28 V. It makes sure that the current only flows from the solar cell to the battery. So when the solar cell has an output voltage lower than the battery potential, D1 will prevent the battery from providing energy to the solar cell. D2 is a micropower band-gap voltage reference diode with a reverse regulation voltage of 1.2 V. It sets the reference voltage for the operational amplifier (op-amp) U1. U1 is used as a comparator. Its power supply terminal is connected to the battery output. The positive input is connected to a resistor network consisting of R1, R2, R4 and R5. Assuming the solar cell has an adequate output voltage, and the voltage of U1's positive input terminal is lower than the voltage of the negative input terminal (1.2 V), U1 will provide an output signal close to ground (logic 0), and the transistor Q1 is off. In this case, solar cell will recharge the battery. However, when the battery potential reaches 1.4 V, the feedback network will present 1.2 V input to the positive input terminal of U1. Then the output of the op-amp changes to logic 1, which turns on the transistor Q1. It therefore shorts the solar cell, and the recharging stops. In another case, if the solar

cell does not have enough voltage to recharge, D1 will block the battery current from flowing back. A list of all the components used in this circuit is shown in Table 5-1 (resistors and capacitors are only shown for their values). This circuit is also suitable for use with a number of other different solar cells, which adds more flexibility to the system.

Table 5-1. List of components used in the solar cell recharging protection circuit

Symbol in the diagram	Value	Component	Company
D1		NSR0140P2T5G	On Semiconductor
D2		LM185-1.2	Linear Technology
U1		LMV951	Texas Instrument
Q1		SI1035X	Vishay
C1	100 nF		
C2	1000 μ F		
C3	100 nF		
R1	15 k Ω		
R2	470 k Ω		
R3	2.2 k Ω		
R4	4.3 k Ω		
R5	47 k Ω		

The solar energy harvesting block was tested to charge up a 2200 μF capacitor. The experiment was conducted in door, and an iPhone flashlight was used as the light source. Figure 5.3 shows the voltage profile of the capacitor during charging. The capacitor was charged up in a few seconds, and the voltage saturates at about 0.84 V. This is because the iPhone flashlight was not strong enough to let the solar cell reach 1.5 V output.

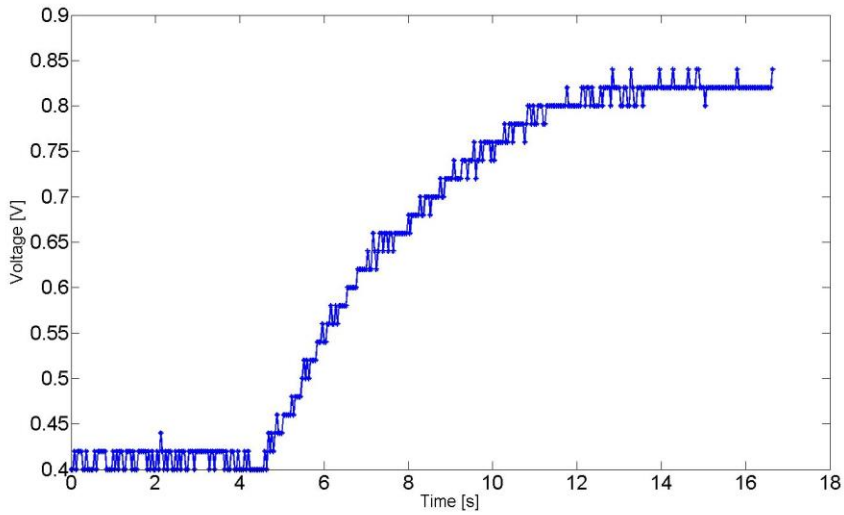


Figure 5.3. 2200 μF capacitor charging with the system solar energy harvesting block and iPhone flashlight

The efficiency of charging can be calculated as follows. The energy stored in the capacitor during charging is:

$$E_{\text{stored}} = \frac{1}{2} CV_2^2 - \frac{1}{2} CV_1^2 = \frac{1}{2} \times 2200 \times 10^{-6} \times (0.84^2 - 0.4^2) = 0.6 \text{ mJ} \quad (5-1)$$

where V_1 is the initial capacitor voltage, and V_2 is the voltage at the end of charging. The input energy was measured as the output of the solar cell. The current values were sampled every 0.17 s and an average voltage value of 0.7 V is used in the

calculation. The total input energy is calculated as a summation of all the sample points.

$$E_{input} = \sum_0^T V_{ave} Idt = 1.27mJ \quad (5-2)$$

where T is the total charging time, V_{ave} is the average output voltage of the solar cell, dt is the sample interval. Therefore, the solar block charging efficiency is:

$$\eta = \frac{E_{stored}}{E_{input}} = \frac{0.6mJ}{1.27mJ} = 47\% \quad (5-3)$$

The major power loss in this block comes from the charging protection circuit. Also note that this efficiency does not include the power loss in the solar cell. The reason to choose a large capacitor as the charging load is that it could provide a more accurate calculation result of the charging efficiency. Additionally, as the light source is restricted in this experiment, it is hard to use the iPhone flashlight to charge the battery cell, especially considering the batteries in the system all work above 0.8 V in typical operations.

5.2 USB Recharging Block

Invented by Ajay Bhatt [63], Universal Serial Bus (USB) is an industry standard developed in the mid-1990s that defines the cables, connectors and communications protocols used in a bus for connection, communication and power supply between computers and electronic devices. It is a convenient power source widely existing on personal computers, tablets and automobiles. As of 2008, approximately 6 billion USB ports and interfaces were in the global marketplace, and

about 2 billion were being sold each year [64]. Because of its stability, USB power will be used as the primary source for this energy harvesting system when available.

USB has an output voltage of 5 V, with maximum current up to 5 A in USB 3.0. The signal has to be conditioned in order to recharge the battery cell discussed in Chapter 4. The chip implemented here is TPS62250, a peak current limited step down converter from Texas Instruments [65]. It has an input voltage range from 2-6 V with peak output current of 1 A. It operates at 2.25MHz fixed switching with efficiency up to over 90 %. The peripheral components are selected to provide a constant output voltage of 1.4 V, which is suitable to recharge the battery cell. The circuit diagram of the whole configuration is shown in Figure 5.4.

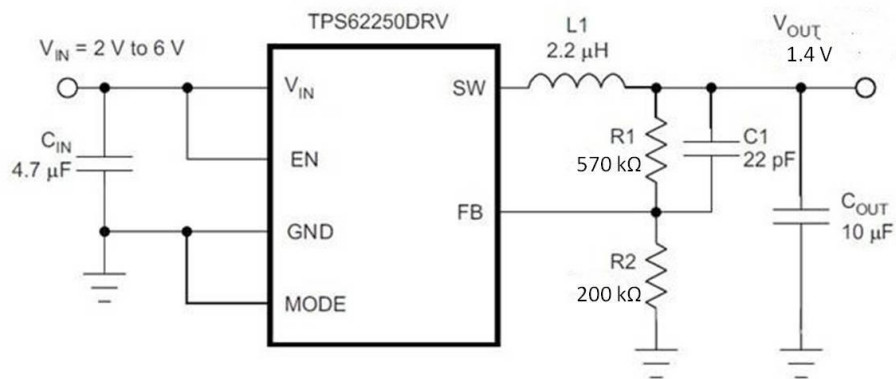


Figure 5.4. Circuit diagram of the step down converter for USB recharging

5.3 Output Voltage Regulator

A battery's potential decreases over time when it discharges. However, for most of the applications utilizing energy harvesting, the load requires a constant

voltage supply. Therefore, an output voltage regulator is needed in the system to provide a desired output.

One of the common choices is the low drop-out (LDO) regulator. It typically includes an error amplifier, a pass transistor, a reference circuit, a feedback network, and some loading elements [66]. Since an average low drop-out voltage regulator consumes several milli-Watts of power, this typical scheme is not suitable for this low power battery-operated system. Based on power considerations, our first solution is to use a single depletion mode transistor connected in series with other circuit elements. As shown in Figure 5.5.

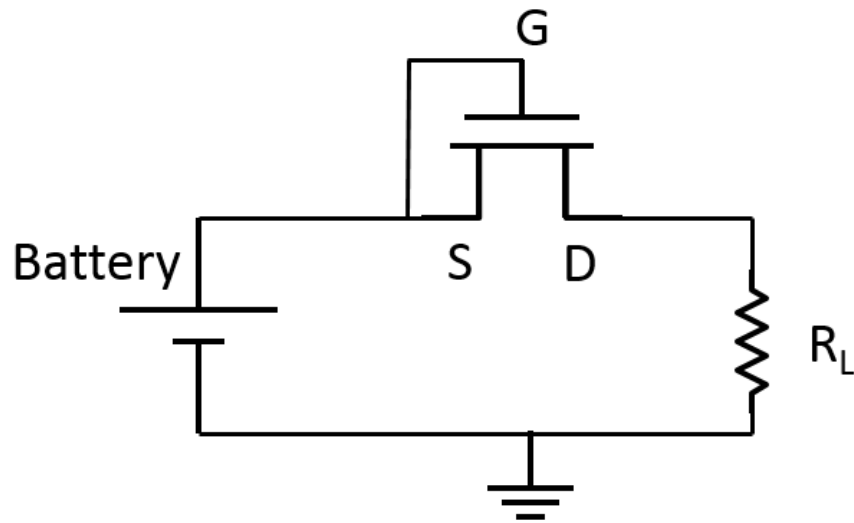


Figure 5.5. Schematic diagram of single series voltage regulator

The operation principle of the circuit is based on the different resistance characteristics within two MOSFET operation regions. As the battery discharges, the depletion mode MOSFET transitions from saturation region to linear region, with a

decrease in its internal resistance. This transition serves to attenuate the current early in the battery cycle and increase the current in the later part of the battery cycle with a feedback mechanism. Therefore, the lifetime of the battery is increased. The average power dissipation in the regulator is only 1.73 μ W. It is very suitable for low power applications.

In order to provide more stable output voltage, several commercial chips were compared by their input/output range, power consumption and efficiency, as shown in Table 5-2.

Table 5-2. Voltage regulator comparison

Chips	Input (V)	Output (V)	Max output current	Efficiency	Quiescent current
MAX1920 [67]	2 – 5.5	1.5, 1.8, 2.5, 3	400 mA	90%	50 μ A
LT1129-3.3 [68]	3.8 - 20	3.3, 5	700 mA	N/A	N/A
LTC3564 [69]	2.5 – 5.5	0.6 – 5.5	1.25 A	96%	20 μ A

LTC3564 from Linear Technology is selected as the core of the voltage regulator in the system for its high efficiency, low power consumption and wide input/output range. It has an input voltage range of 2.5 V to 5.5 V, a supply current of 20 μ A with efficiency up to 96 %. The output voltage temporarily set to be 3 V, which is common for a variety of electronic applications. It also can be adjusted by modify the configuration around the chip. The circuit diagram is shown in Figure 5.6.

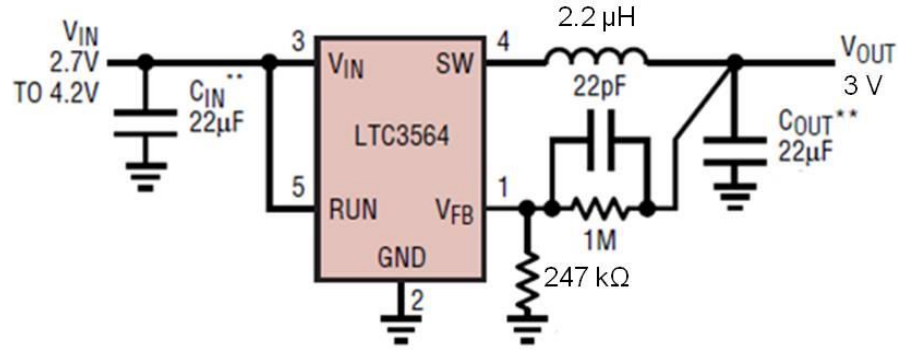


Figure 5.6. Circuit diagram of output voltage regulator

The voltage regulating block was tested with two different resistive loads as shown in Table 5-3. The output voltage is stable around 3 V within the typical operation voltage range of the battery cells. The results indicate a voltage regulating efficiency over 96%, which verified the specifications in datasheet.

Table 5-3. Testing results of voltage regulating block based on LTC3564

Input voltage	Input current	Output voltage	Load	Input power	Output power	Efficiency
4.8 V	2 mA	3.03 V	1 kΩ	9.6 mW	9.2 mW	96%
4.8 V	24 mA	3.33 V	100 Ω	115.2 mW	110.9 mW	96%

5.4 Microcontroller Overview

The complete power distribution system (PDS) includes 2 battery arrays. While one array is working, the other array will be recharged by energy harvesters. A control block is needed to monitor the batteries' voltage and switch the states of two battery arrays. Also, some energy sources may not be available at some time; and

even if multiple sources are available, choices have to be made to select the most stable one for battery recharge. There are other functions that need to be realized, such as clock signal supply and system shut down in emergency. The most suitable way to deal with all these functions with flexibility is to use a microcontroller. However, there are some requirements for the microcontroller to be used in this low power system, including power supply as low as 3 V, and ultra-low power consumption, preferably in microwatt level, which rules out most of the options. The microcontroller chosen for the system is an EM6819 from EM Microelectronic [70].

The microcontroller function blocks can be separated into 5 different categories [70]: power management and security functions, memories and CPU core, clock selection, clock switching and system peripherals, digital and analog internal peripherals and communication interfaces via the IO pads.

EM6819 has a power supply range from 0.9 V to 3.6 V with less than 6 μ W power consumption in standby mode at 8 kHz clock signal. Measurements also show that it has less than 40 μ W power consumption when executing a voltage level detection function. Figure 5.7 shows an overview of the microcontroller.

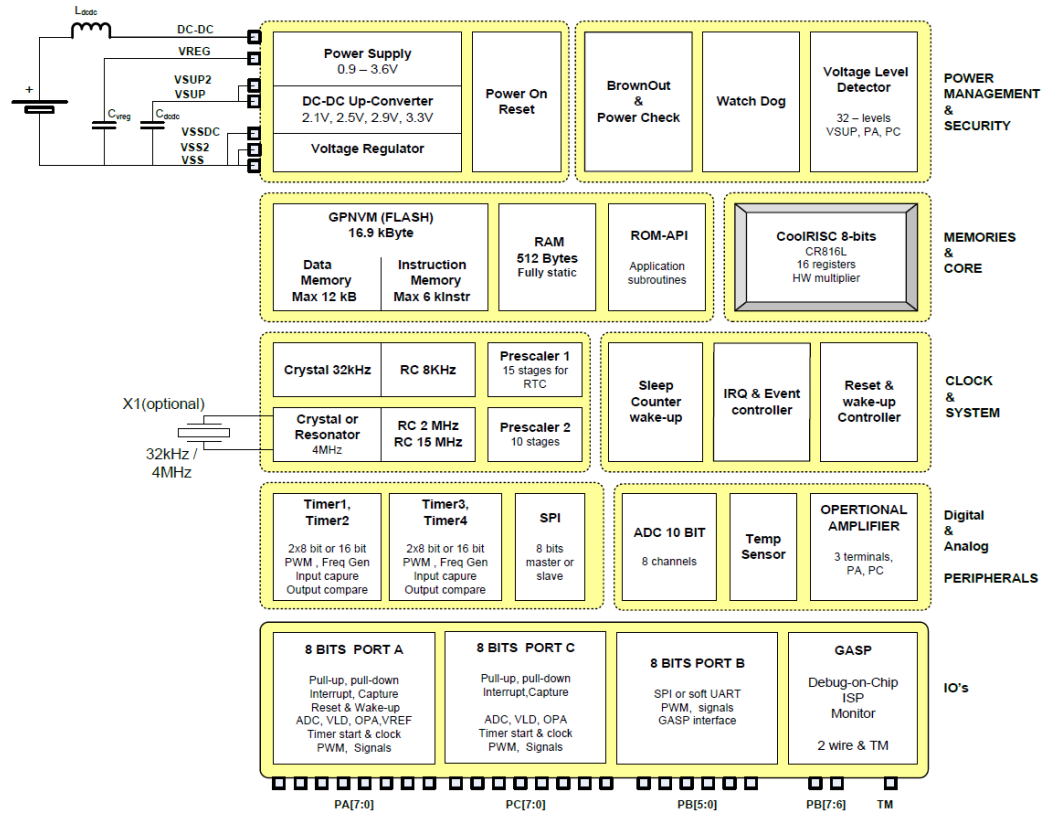


Figure 5.7. EM6819 overview [70]

The power management block assures a proper system start at power up with Power on reset and power check function. The internal Brownout supervises the CPU and core internal power supply and asserts a reset when the circuit is under minimum voltage. The watchdog function monitors the CPU execution, and the VLD can be used to monitor internal or external voltages. Its results are available to the user to take actions accordingly. The DC-DC converter can be switched on by demand.

The memories and CPU core block contains all the FLASH memories, the nonvolatile data memory (mapped into the FLASH memory), the RAM and the vendor supplied application subroutines (ROM-API) for nonvolatile memory modifications. CR816 microprocessor core is another essential part of the block.

The clock selection, clock switching block takes care of all internal and external clock sources. It synchronizes the clocks where needed and assures that the system won't stop working due to faulty clock switching (i.e avoids switching to a non-present clock source). This block is also an essential part of the low power architecture by minimizing the total energy consumption and budgeting the active clocking nodes.

Digital and analog internal peripherals contains all the user peripherals such as timer, Serial peripheral interface (SPI) bus, analog to digital converter (ADC) and other functional blocks. These peripherals are configurable and fully adjustable to the user application.

Communication interfaces include all the external communication channels grouped. All communication goes through at least 1 of the max 24 IO's with several internal functions such as, serial interface, PWM, frequency outputs mapping to the IO's.

There are four distinctive operation modes in the microcontroller: Active, Standby, Sleep and Power-down. In active mode, CPU will be running and all the functions are ready to be used. The other three modes are specific for low power applications. In these modes, CPU will be in standby without clock, and only part of the functions may be used.

A block diagram of the microcontroller is shown in Figure 5.8. The circled blocks are the key parts used in this PDS. The clock frequency used in this case is 8 kHz, since it's fast enough for the system operation and suitable in low power mode. A Voltage Level Detector (VLD) is employed to monitor the battery potential and

decide the status of the battery arrays. The IRO & Event block on the right is to handle the interrupt generated by voltage detector, and react to it accordingly. Timers are used to control the recharging time and also provide low frequency clock signal for the SC voltage converter discussed in Chapter 3. The microcontroller also operates in sleep mode during recharging the battery, with only the sleep counter to wake it up. It has three I/O ports and a General Access Serial Port (GASP) for power supply and programming.

Ultra Low Power 8 bit Flash μ Controller:
0.9V supply, DC-DC Converter, ADC, OpAmp, EEPROM, 8 to 32 leads

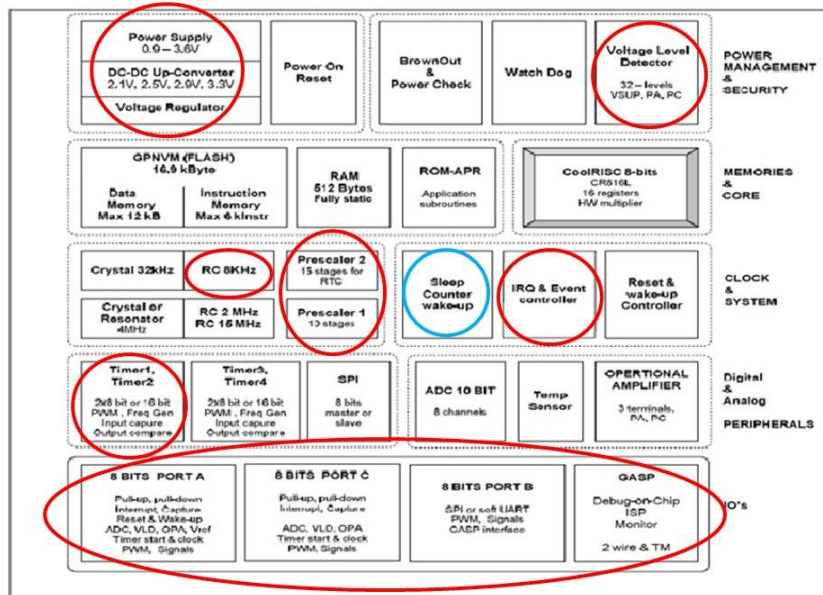


Figure 5.8. Block diagram of the microcontroller EM6819

5.5 System Overview

5.5.1 Battery Arrays

A fully recharged battery cell discussed in Chapter 4 has an open circuit voltage of 1.2 V. In order to provide a stable 3 V output with sufficient current supply, the single array of 4 batteries is selected. The batteries will provide energy in series, and be recharged in parallel. A total of 2 battery arrays are employed for the completely stand-alone system. While one array is providing energy to the load, the other array will be recharged. The battery combination can be readily adjusted with respect to the different output requirements and the specific application.

The battery array uses a similar configuration as the SC voltage converter, as shown in Figure 5.9. When $D = 1$, $\overline{D} = 0$, all the four batteries (B1-B4) are recharged in parallel by the energy harvesters; when $\overline{D} = 1$ and $D = 0$, four batteries are changed to series connection, providing a maximum output voltage of 4.8 V (4 times 1.2 V), which is converted to 3 V by the voltage converter discussed in Section 5.3. As the discharge continues, the output voltage of the battery array will drop but the voltage converter will keep the load voltage as 3 V. The other array uses complimentary control signals. When $\overline{D} = 1$ and $D = 0$, four batteries are recharged in parallel and when $D = 1$, $\overline{D} = 0$, they are changed to series connection to discharge.

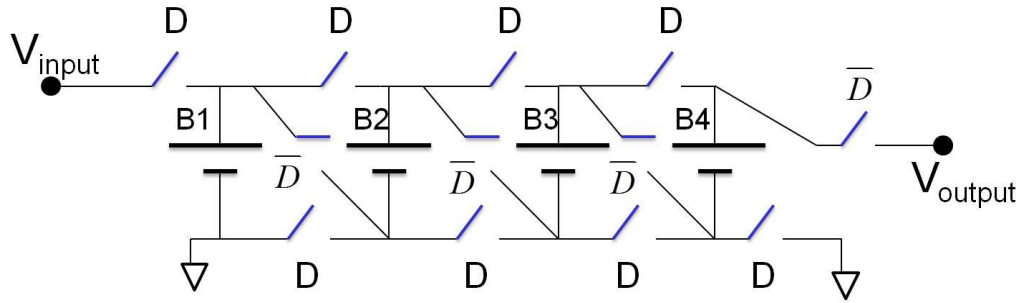


Figure 5.9. Circuit diagram of a single battery array

The switch selection is critical in this low power system. Since the switching frequency is low (could be hours or days depending on the specific applications), the key issues would be the static and dynamic power consumption, especially the on-resistance. The component selected in the system is Si1035X [71], as shown in Figure 5.10. The maximum ratings are shown in Figure 5.11. The static and dynamic specifications are shown in Figure 5.12. It has two complementary n- and p-channel MOSFETs, which are used as a transmission gate switch. Compared to a single NMOS or PMOS, a transmission gate has smaller on-resistance and lower dynamic power consumption.

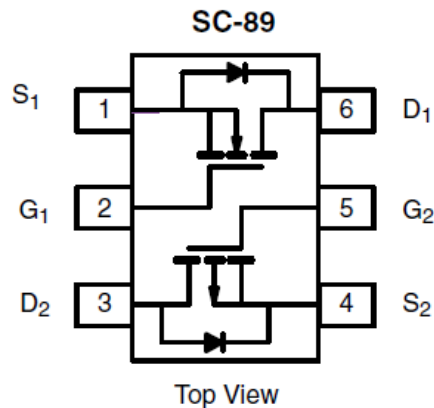


Figure 5.10. Internal circuit of Si1035X [71]

ABSOLUTE MAXIMUM RATINGS ($T_A = 25\text{ }^\circ\text{C}$, unless otherwise noted)							
Parameter	Symbol	N-Channel		P-Channel		Unit	
		5 s	Steady State	5 s	Steady State		
Drain-Source Voltage	V_{DS}	20		- 20		V	
Gate-Source Voltage	V_{GS}	± 5					
Continuous Drain Current ($T_J = 150\text{ }^\circ\text{C}$) ^a	$T_A = 25\text{ }^\circ\text{C}$	I_D	190	180	- 155	- 145	mA
	$T_A = 85\text{ }^\circ\text{C}$		140	130	- 110	- 105	
Pulsed Drain Current ^b	I_{DM}	650		- 650		mW	
Continuous Source Current (Diode Conduction)	I_S	450	380	- 450	- 380		
Maximum Power Dissipation ^a	$T_A = 25\text{ }^\circ\text{C}$	P_D	280	250	280	250	mW
	$T_A = 85\text{ }^\circ\text{C}$		145	130	145	130	
Operating Junction and Storage Temperature Range	T_J, T_{stg}	- 55 to 150				$^\circ\text{C}$	
Gate-Source ESD Rating (HBM, Method 3015)	ESD	2000				V	

Figure 5.11. Absolute maximum ratings of Si1035X [71]

SPECIFICATIONS ($T_J = 25\text{ }^\circ\text{C}$, unless otherwise noted)							
Parameter	Symbol	Test Conditions	Min.	Typ.	Max.	Unit	
Static							
Gate Threshold Voltage	$V_{GS(th)}$	$V_{DS} = V_{GS}, I_D = 250\text{ }\mu\text{A}$	N-Ch	0.40			V
		$V_{DS} = V_{GS}, I_D = -250\text{ }\mu\text{A}$	P-Ch	-0.40			
Gate-Body Leakage	I_{GSS}	$V_{DS} = 0\text{ V}, V_{GS} = \pm 2.8\text{ V}$	N-Ch		± 0.5	± 1.0	μA
		$V_{DS} = 0\text{ V}, V_{GS} = \pm 4.5\text{ V}$	P-Ch		± 0.5	± 1.0	
Zero Gate Voltage Drain Current	I_{DSS}	$V_{DS} = 16\text{ V}, V_{GS} = 0\text{ V}$	N-Ch		1	500	nA
		$V_{DS} = -16\text{ V}, V_{GS} = 0\text{ V}$	P-Ch		-1	-500	
		$V_{DS} = 16\text{ V}, V_{GS} = 0\text{ V}, T_J = 85\text{ }^\circ\text{C}$	N-Ch			10	μA
		$V_{DS} = -16\text{ V}, V_{GS} = 0\text{ V}, T_J = 85\text{ }^\circ\text{C}$	P-Ch			-10	
On-State Drain Current ^a	$I_{D(on)}$	$V_{DS} = 5\text{ V}, V_{GS} = 4.5\text{ V}$	N-Ch	250			mA
		$V_{DS} = -5\text{ V}, V_{GS} = -4.5\text{ V}$	P-Ch	-200			
Drain-Source On-State Resistance ^a	$R_{DS(on)}$	$V_{GS} = 4.5\text{ V}, I_D = 200\text{ mA}$	N-Ch			5	Ω
		$V_{GS} = -4.5\text{ V}, I_D = -150\text{ mA}$	P-Ch			8	
		$V_{GS} = 2.5\text{ V}, I_D = 175\text{ mA}$	N-Ch			7	
		$V_{GS} = -2.5\text{ V}, I_D = 125\text{ mA}$	P-Ch			12	
		$V_{GS} = 1.8\text{ V}, I_D = 150\text{ mA}$	N-Ch			9	
		$V_{GS} = -1.8\text{ V}, I_D = -100\text{ mA}$	P-Ch			15	
		$V_{DS} = 1.5\text{ V}, I_D = 40\text{ mA}$	N-Ch			10	
		$V_{DS} = -1.5\text{ V}, I_D = -30\text{ mA}$	P-Ch			20	
Forward Transconductance ^a	g_{fs}	$V_{DS} = 10\text{ V}, I_D = 200\text{ mA}$	N-Ch		0.5		S
		$V_{DS} = -10\text{ V}, I_D = -150\text{ mA}$	P-Ch		0.4		
Diode Forward Voltage ^a	V_{SD}	$I_S = 150\text{ mA}, V_{GS} = 0\text{ V}$	N-Ch			1.2	V
		$I_S = -150\text{ mA}, V_{GS} = 0\text{ V}$	P-Ch			-1.2	
Dynamic^b							
Total Gate Charge	Q_g	N-Channel $V_{DS} = 10\text{ V}, V_{GS} = 4.5\text{ V}, I_D = 150\text{ mA}$	N-Ch		750		pC
Gate-Source Charge	Q_{gs}		P-Ch		1500		
Gate-Drain Charge	Q_{gd}	P-Channel $V_{DS} = -10\text{ V}, V_{GS} = -4.5\text{ V}, I_D = -150\text{ mA}$	N-Ch		75		
			P-Ch		150		
Turn-On Time	t_{ON}	N-Channel $V_{DD} = 10\text{ V}, R_L = 47\text{ }\Omega$ $I_D \cong 250\text{ mA}, V_{GEN} = 4.5\text{ V}, R_g = 10\text{ }\Omega$	N-Ch			75	ns
			P-Ch			80	
Turn-Off Time	t_{OFF}	P-Channel $V_{DD} = -10\text{ V}, R_L = 65\text{ }\Omega$ $I_D \cong -150\text{ mA}, V_{GEN} = -4.5\text{ V}, R_g = 10\text{ }\Omega$	N-Ch			75	ns
			P-Ch			90	

Notes:

a. Pulse test; pulse width $\leq 300\text{ }\mu\text{s}$, duty cycle $\leq 2\%$.

b. Guaranteed by design, not subject to production testing.

Figure 5.12. Specifications of Si1035X [71]

The datasheet shows that the transmission gate has an on resistance of $3\text{ }\Omega$ and a typical threshold voltage of 0.9 V . This chip was tested with a dc voltage source and a resistor, as shown in Figure 5.13. The test results are shown in Table 5-4. It shows an on resistance less than $1\text{ }\Omega$, which is very suitable for use in the PDS.

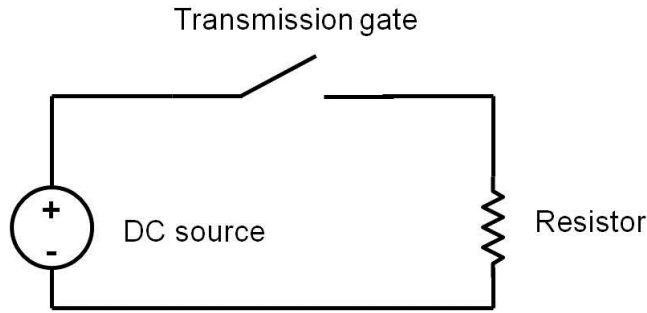


Figure 5.13. Testing circuit and the transmission gate Si1035X

Table 5-4. Testing results of Si1035X

Supply voltage	Load value	Load voltage	Si1035X on resistance
3.068 V	1.5 k Ω	3.066 V	0.978 Ω
3.067 V	217 Ω	3.053V	0.995 Ω

5.5.2 Microcontroller Implementation

The EM6819 microcontroller was equipped with software and hardware development tool kits. The EM6819 Tool Kits are based on the REva mother board platform that consists of a generic motherboard with interchangeable daughter boards supporting several target microcontrollers and an embedded RLink for in-circuit programming and debugging [72] [73]. A picture of the REva mother board is shown in Figure 5.14. The package of EM6819 adopted in the system is TSSOP28 because it provides enough I/O ports. The microcontroller was programmed and tested on

mother board first, and later was mounted on a customized printed circuit board (PCB) for the PDS. The designed PCB will be discussed in Section 5.6.

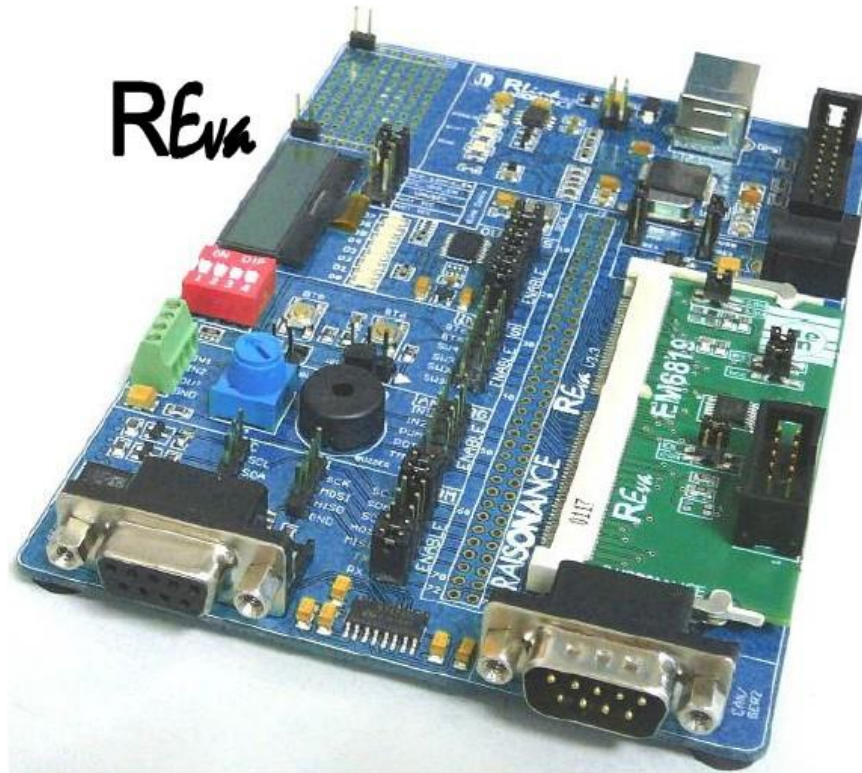


Figure 5.14. The REva mother board for microcontroller EM6819 [73]

The Raisonance CoolRISC 816 development kit is a complete solution for creating software for the CoolRISC 816 family of microcontrollers, including EM6819 [74]. The development kit comprises many different tools that allow projects from simple to highly complex tasks to be developed. The Raisonance development tool has several parts in it. Ride 7 is the integrated development environment, the interface for all the other tools, provides an editor, a project manager and a debugging user interface that can be used either with the simulator or with any of several

hardware-debugging tools. Rkit-C816 includes the specific tools for project development. SIMICE C816 serves as the simulator of the core and most peripheral circuits. RLink-C816 is the JTAG standard emulator with USB interface allowing user to program the C816 on an application board and debug it when it is running.

Figure 5.15 shows the integrated development environment in RLink, which is driven by RIDE [72]. The tool chain includes an editor, a project manager, a GNU C Compiler, an assembler and a linker. The program was coded in C language.

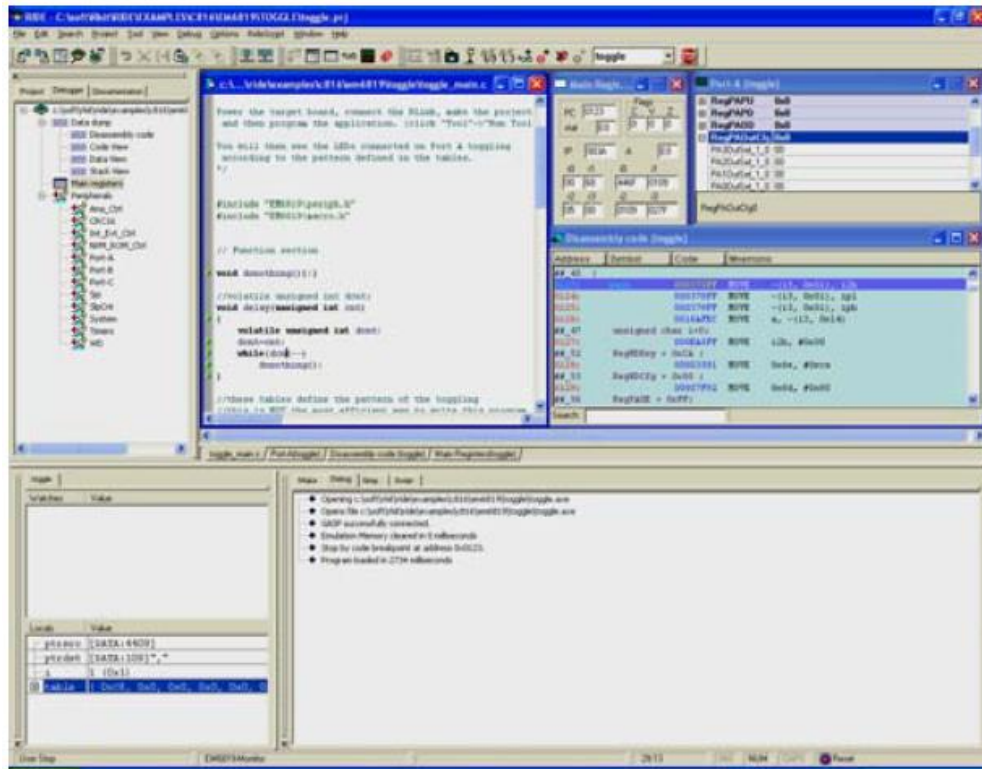


Figure 5.15. Development environment of RLink

Figure 5.16 shows the functional blocks of the system and the routing of signal and power lines. The flow chart of the microcontroller program is shown in Figure 5.17. In the flow chart, V_USB is the output voltage of USB energy harvester

block, V_{Solar} is the output voltage of solar energy harvester block, V_{RF} is the output voltage of RF energy harvester block, V_{Supply} is the output voltage of the system, V_{main} is the output voltage of the main battery array and V_{backup} is the output voltage of the backup battery array.

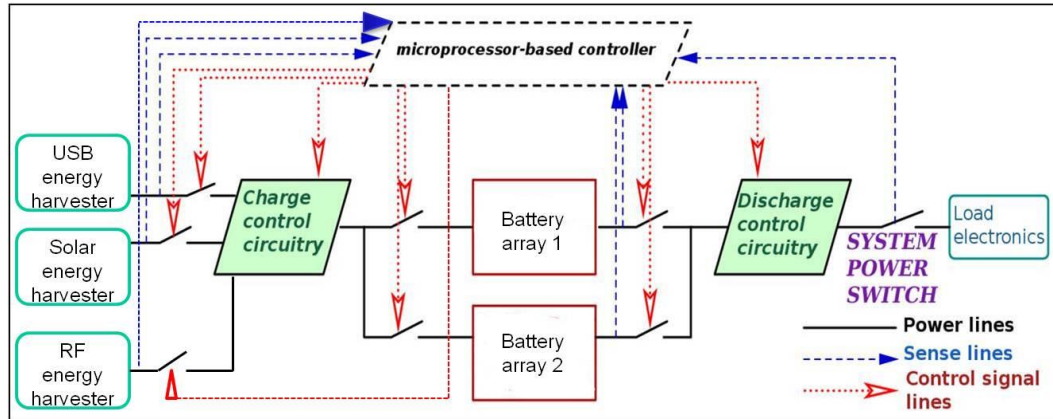
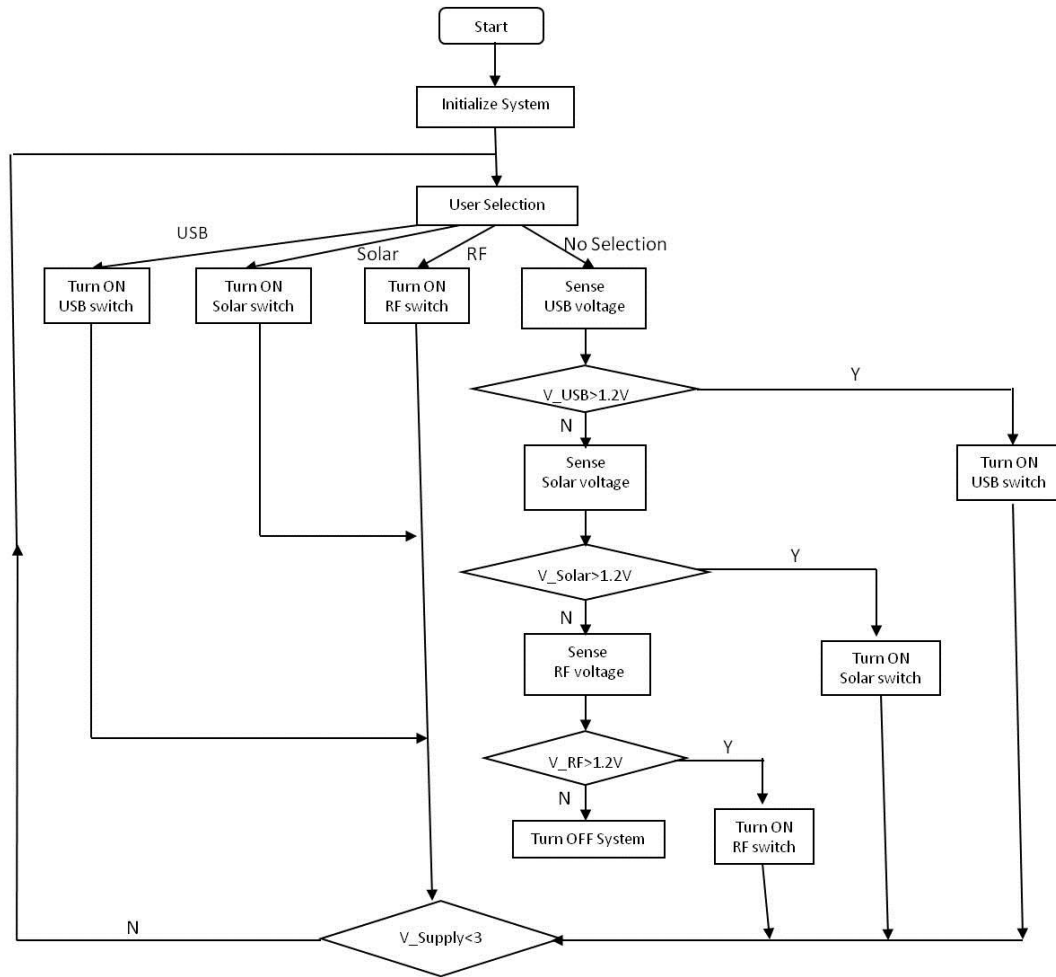
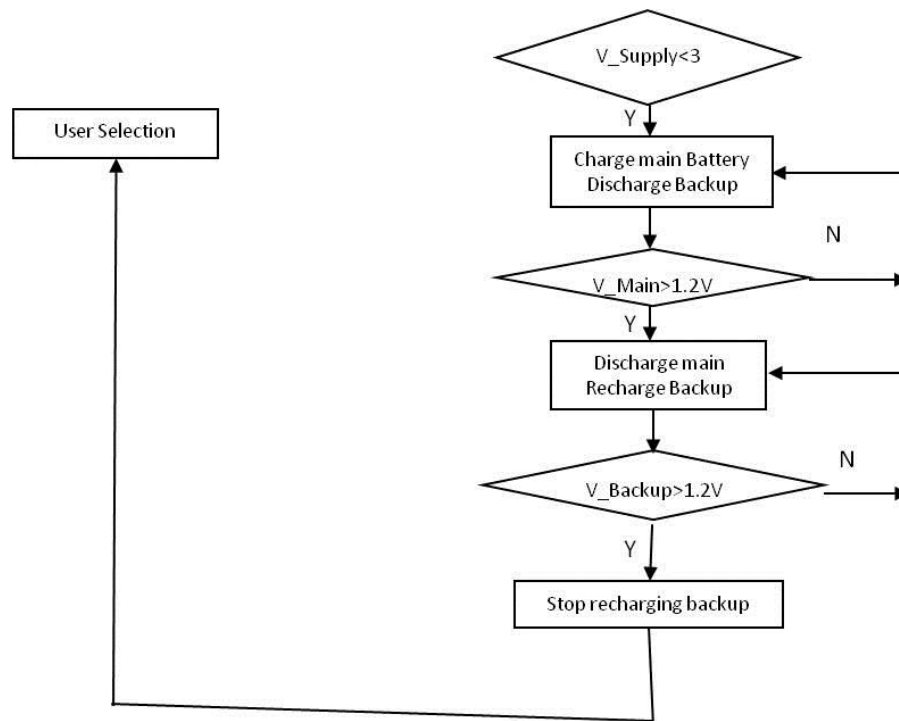


Figure 5.16. Block diagram of the power distribution system and signal/power line routing



(a) Initialization and energy sources selection



(b) Discharge and recharge process

Figure 5.17. Flow chart of the microcontroller program

As discussed before, the system has three power sources: USB power, solar energy and RF energy. Depending on user selection, one of the three will be chosen as the power supply to the system. There two battery arrays are differentiated as the main battery and the backup battery. The main battery delivers power to the power consumption components and the backup battery is only used when the main battery is deeply discharged.

When system is on, the microcontroller initializes the system by setting the clock frequency and enabling input, output and interrupting ports. The user may select one power source out of USB source, solar source and RF source, and the system turns on the power switch of the corresponding power source and turns off the rest two. If user made no selection, the microcontroller would do voltage level

detections and decide for the user. The USB source has the highest priority while the RF source has the lowest. That is to say, if the user does not select any source manually, the USB supply is always selected by the microcontroller as long as it is available. And the RF supply is selected only when USB and solar sources have no voltages.

If the system supply node voltage is higher than 3 V (four battery cells in series), the main battery still has enough energy to drive the circuit, and the system would go back to the starting point of the loop and choose the new power source. If the voltage of the supply node is below 3 V, the main battery is deeply discharged and it should be recharged, and the backup array serves as the supply temporarily. When the main battery arrays is fully recharged (each of the single cell is over 1.2 V), the system will switch back to let the main battery power the load, meanwhile the backup array needs to be recharged to compensate the energy loss. After the backup is fully recharged, the whole loop starts again.

Please refer to Appendix A for the original code.

5.5.3 Printed Circuit Board Design

A printed circuit board (PCB) has been designed using PCB Artist and fabricated by Advanced Circuits. It is a 2 layer standard board with 0.16 cm material thickness and an area of 14.3 cm x 13.8 cm. Figure 5.18 shows the board layout without copper pouring for viewing clearance. The board includes different blocks of the PDS as shown in the figure. In the fabricated board, both sides are poured with copper in order to reduce crosstalk and increase signal stability. A photo of the fabricated PCB without soldered components is shown in Figure 5.19.

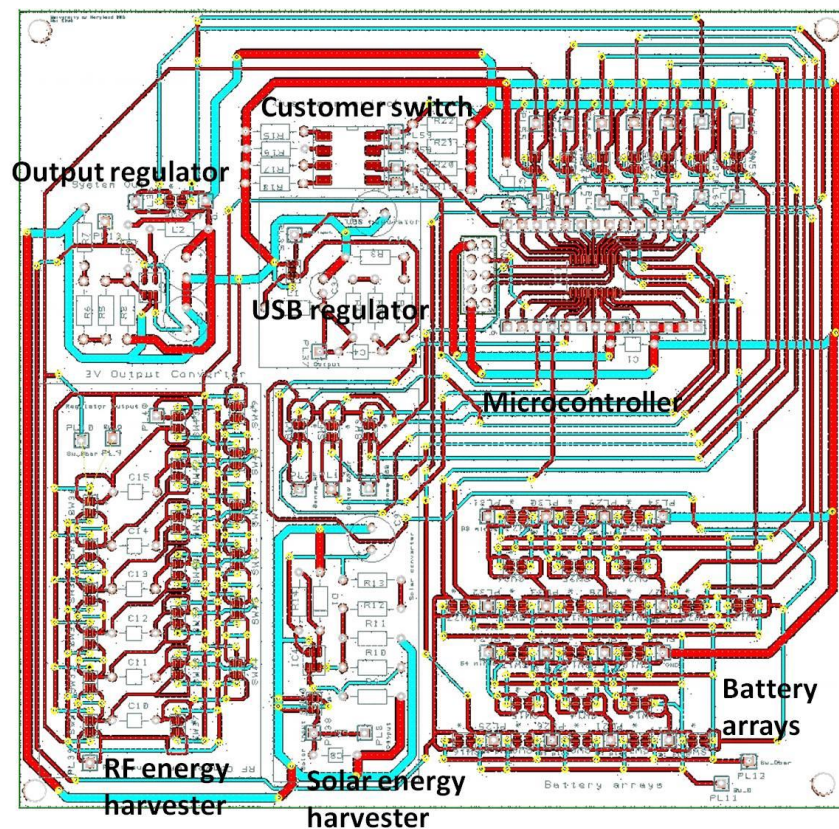


Figure 5.18. Layout of the power distribution system PCB

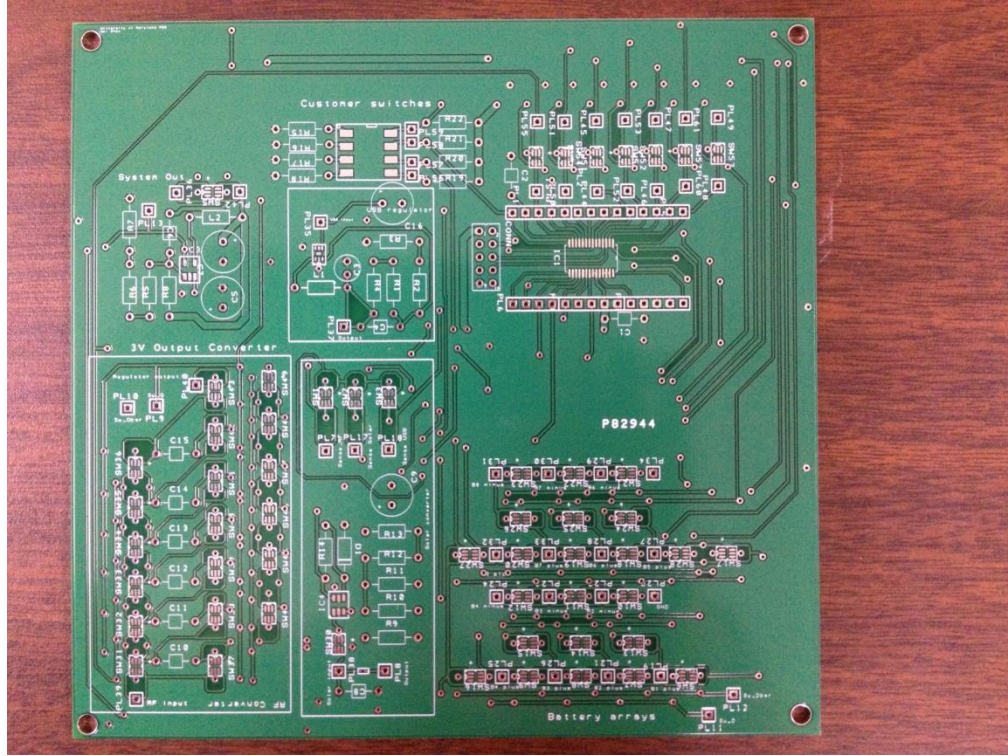


Figure 5.19. PCB of the power distribution system

The SC voltage converter discussed in Chapter 3 was also implemented on the PCB for flexibility. The switches in the converter were also constructed by Si1035X. Therefore, two versions of the SC voltage converter are available including an IC chip based on IBM 130 nm process, and a discrete version mounted on PCB.

The SC voltage converter in PCB version was tested with a 0.16 V constant input to charge a 2200 μF capacitor. The clock signal was 2 Hz square wave. The initial voltage of the capacitor was 0 V. The test stopped when the capacitor voltage reaches 0.75 V. The average input current was measured to be 0.18 mA. Therefore, the charging efficiency can be calculated as follows.

$$E_{\text{stored}} = \frac{1}{2} CV_{\text{cap}}^2 = \frac{1}{2} \times 2200 \mu\text{F} \times 0.75^2 = 0.62 \text{mJ} \quad (5-4)$$

$$E_{input} = V_{input} I_{ave} t = 0.16V \times 0.18mA \times 58s = 1.68mJ \quad (5-5)$$

$$\eta = \frac{E_{stored}}{E_{input}} = \frac{0.62mJ}{1.68mJ} = 37\% \quad (5-6)$$

The efficiency of the SC voltage converter on PCB is a little lower than the SC voltage converter on chip. This may be due to the static and dynamic loss of parasitic components on PCB is larger than it is in the chip. However, this efficiency value is still reasonable for RF energy harvesting.

The board also includes a 219-4LPST DIP switch [75] for the user to select the desired energy source. The switch has four channels. Only three of them are used, corresponding to the three targeted energy sources.

5.6 RF Energy Harvesting Experiments

In the experiment described here, the RF energy harvesting block (including the rectenna, the SC voltage converter in IBM 130 nm process and the battery cell) is tested off the PCB. A commercially available walkie-talkie was used as an RF source generator, placed at 0.5 m distance from the rectenna. It operates using Frequency Hopping Spread Spectrum (FHSS) technology in the 900 MHz ISM frequency band, and has a maximum output power of 1 W [76]. Note that the output voltage of the antenna varies with the distance to the source. The grounds for choosing this distance is that at 0.5 m the rectenna provides an output suitable to be boosted. The rectenna receives a power of 0.255 mW, and a Poynting Theorem calculation yields an input voltage of 1.83 V. Measurement on the output end of rectenna shows an open circuit output voltage around 0.35 V with ripples of mV magnitude. The voltage converter

with the full six stage configuration was operated by a 2 Hz and 50 % duty cycle clock signal. The system set up is shown in Figure 5.20.

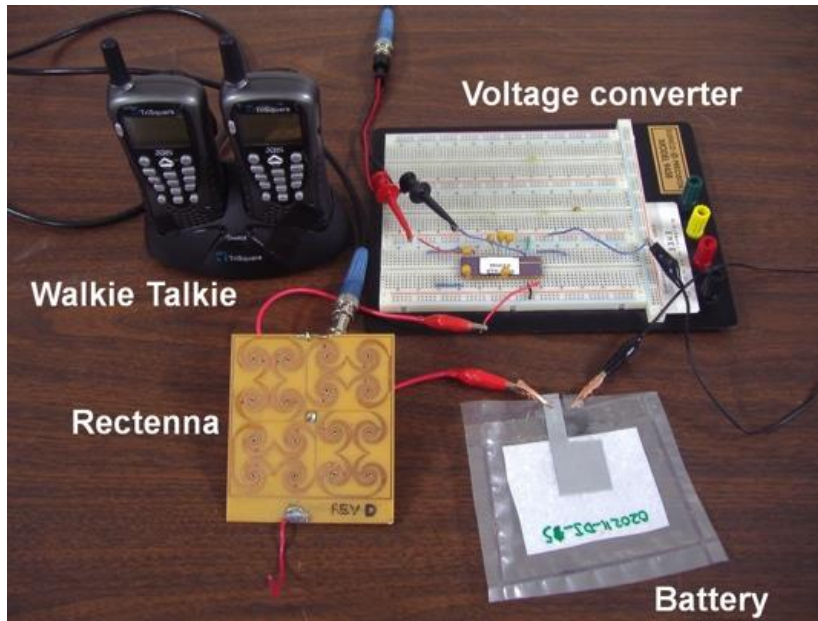


Figure 5.20. Experimental setup of the RF energy harvesting system. The voltage converter is an integrated silicon IC in package being tested on the bread board.

The voltage values were collected by Agilent 34410 operated by a self-designed Labview program remotely. The panel configuration and block diagram of the Labview program are shown in Figure 5.21 and Figure 5.22, respectively.

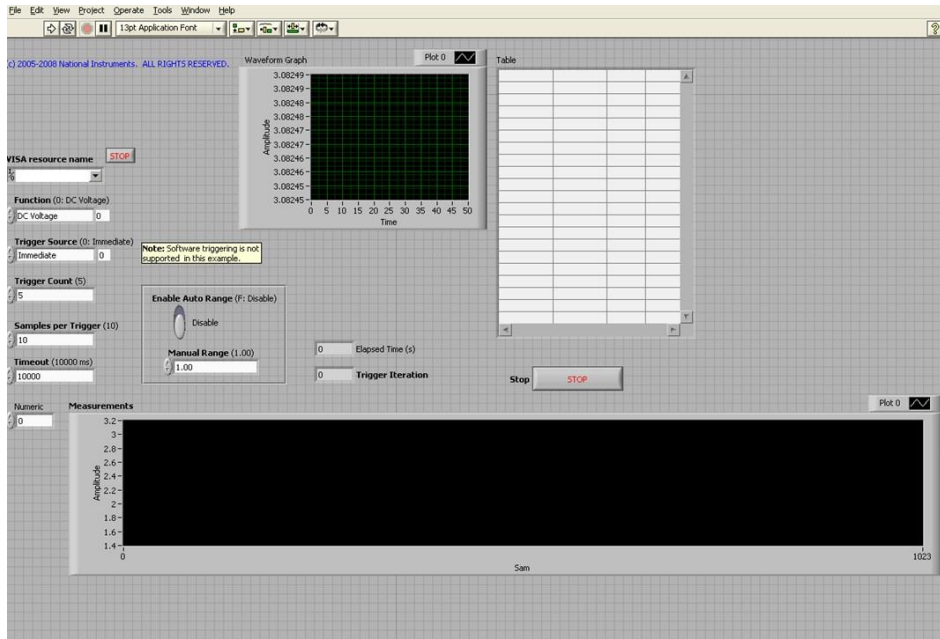


Figure 5.21. Panel configuration of the designed LabView program

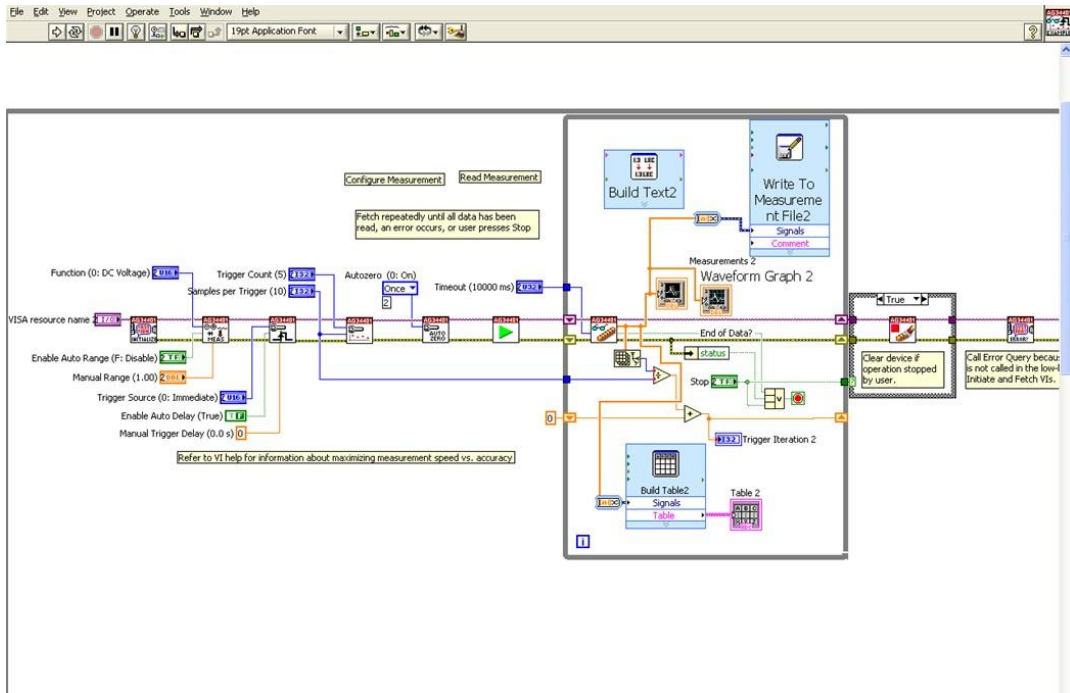


Figure 5.22. Block diagram of the designed LabView program

The test procedure follows three steps for battery re-charge: 1) initial discharge, 2) battery re-charge, and 3) a second discharge. The first discharge of the battery consumes part of its stored energy, hence, it prepares the battery for being recharged, and it is also used as a reference. The purpose of the second discharge is to observe the change in potential after the converter has re-charged the battery.

The experiments were run twice with different load conditions. In the first test, the battery was discharged through a 1 k Ω load for 7 min. As shown in Figure 5.23, discharge curve A, the load voltage dropped from 0.782 to 0.631 V. Secondly, the battery was charged by the energy harvesting system for 1 h, with walkie talkie providing the power. Figure 5.24 shows the potential increase over the charging process (from 0.669 to 0.725 V). Finally, the battery was connected to the 1 k Ω load again for about 6 min, in order to observe the second discharge. As shown in Figure 5.23, discharge curve B, the battery started sourcing energy from 0.710 V. Compared to the load voltage prior to re-charging (0.631 V), the load voltage of the battery has increased after re-charging. Results show that the battery is successfully re-charged, and the system is working properly.

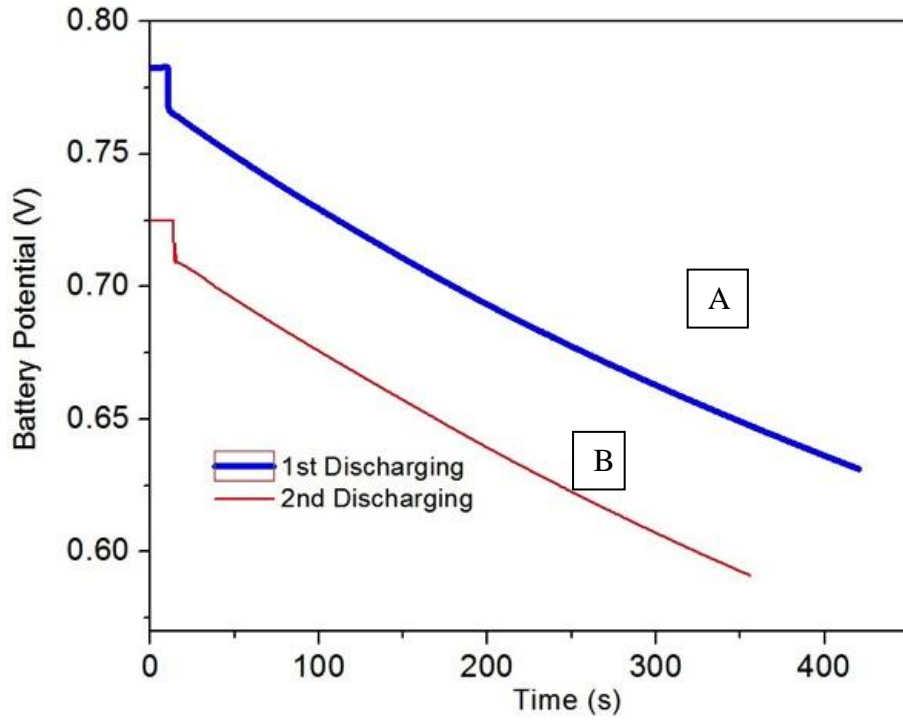


Figure 5.23. Comparison of two discharging processes & the battery potential change during 1 h charging

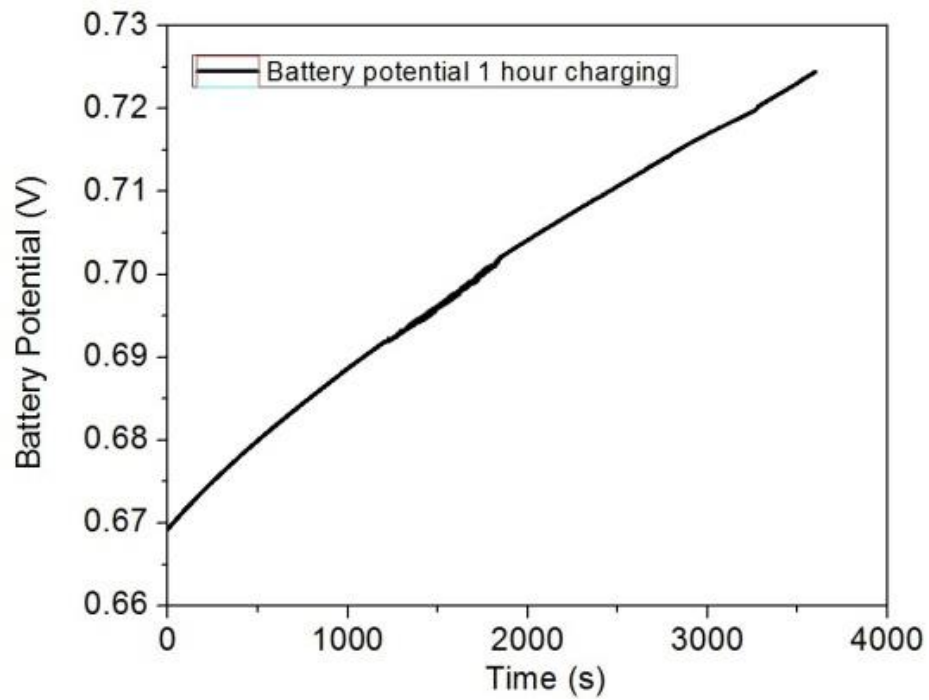


Figure 5.24. Change of battery potential during recharge

The energy harvesting efficiency of this system can be calculated as follows. The walkie talkie uses a small loop antenna to radiate RF signals. According to the derivation in [77], the power radiated from this antenna can be expressed by:

$$P_r = \eta \left(\frac{\pi}{12} \right) (ka)^4 |I_0|^2 \left[1 + j \frac{1}{(kr)^3} \right] \quad (5-7)$$

Where: η is 377 Ohms, k is $2\pi/\lambda$, a is the loop radius and I_0 is the current value flowing in the loop. Here λ is 33 cm. r is 50 cm. So $(kr)^3 \gg 1$, the second term within the bracket can be neglected, and the equation can be treated as far field [77]. We assume the walkie-talkie transmits power isotropically, so the input power of the system can be expressed as

$$P_{input} = \frac{P_{RF}}{4\pi r^2} \cdot A \quad (5-8)$$

Where: P_{RF} is the total power emitted by the walkie-talkie, r is the distance between walkie-talkie and rectenna, and A is the metal area of rectenna. Consequently, the charging efficiency can be calculated as

$$\eta = \frac{E_{store}}{P_{input} \cdot t} = \frac{\frac{1}{2} C (V_2^2 - V_1^2)}{P_{input} \cdot t} \quad (5-9)$$

Where: E_{store} is the energy stored in the battery as a result of the charging operation. The battery cell used in this experiment can be modeled as a 2 F supercapacitor as discussed in Section 4.2. t is the total charging time. A charging efficiency of 5.8 % has been achieved, as shown in Table 5-5. This calculation method can be named as the “capacitance modeling method”.

Table 5-5. Values in calculation of recharging efficiency using “capacitance modeling method” in the first experiment

E_{store} [mJ]	t [sec]	P_{input} [mW]	$P_{converter}$ [mW]	η [%]
105.9	3600	0.5092	0.00384	5.8

To verify this efficiency, another calculation is performed. The final battery potential of the first discharge, 0.631 V, is used as a reference. Next, the output power of the second discharge is integrated over the time period from the beginning of discharge, till the voltage drops back to 0.631 V. The integration result is the extra energy that is recharged into the battery. This yields a stored energy of 118.5 mJ, and an overall efficiency of 6.5 %. This calculation method can be named as the “voltage reference method”, with the calculation equation shown as follows:

$$E_{store} = \int_0^{t_d} \frac{V^2}{R} dt \quad (5-10)$$

where t_d stands for the time from the beginning of second discharge to till the voltage drops back to that before the recharge. The related values in this calculation are shown in Table 5-6.

Table 5-6. Values in calculation of recharging efficiency using “voltage reference method” in the first experiment

E_{store} [mJ]	t_d [sec]	P_{input} [mW]	η [%]
118.2	261	0.5092	6.5

A second test was repeated similarly to the one described above, with a different a discharging load and discharging time. Firstly, the battery was discharged through a 500 Ω load for 9 minutes. As shown in Figure 5.25, discharge curve A, the load voltage dropped from 1.15 to 0.83 V. Secondly, the battery was charged for 1 h by means of the energy harvesting system, with the walkie-talkie providing the power. Figure 5.26 reveals the potential increase over the charging process (from 0.89 to 1.16 V). Finally, the battery was connected, again, to the 500 Ω load for 173 s, in order to observe the second discharge. As shown in Figure 5.25, discharge curve B, the battery started sourcing energy from 0.90 V (There was an initial voltage drop of ca. 0.2 V, from the open circuit voltage to the load voltage. Load voltage was taken as the actual voltage of the battery). Compared to the load voltage prior to re-charging (0.83 V), the load voltage of the battery has increased after re-charging and the battery is successfully re-charged. Table 5-7 shows the charging efficiency calculation based on the “capacitance modeling method” in this test. The efficiency value with this method is 6.6 %. On the other hand, using the “voltage reference calculation”, the total energy conversion efficiency is 7.7 %. The related values are shown in Table 5-8.

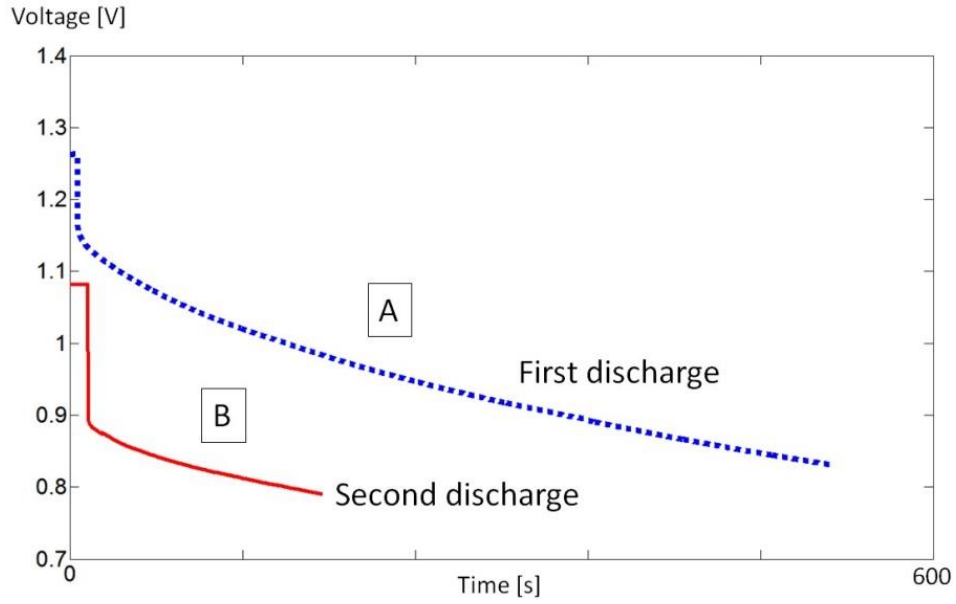


Figure 5.25. Comparison of the first and second discharge processes (curves A and B, respectively) of the second test

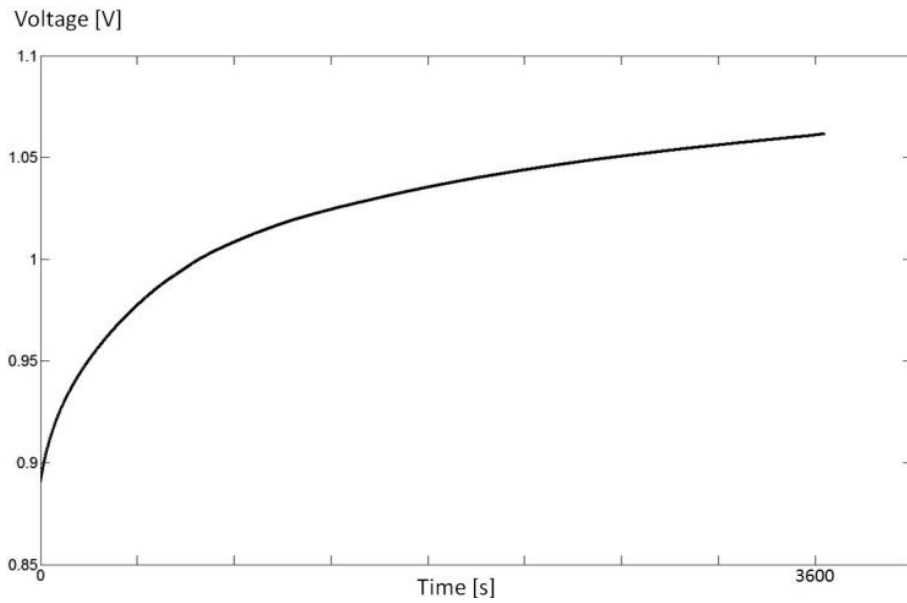


Figure 5.26. Change of battery potential during charging over about 1 h of the second discharge

Table 5-7. Recharging efficiency calculation using “capacitance modeling method” of the second RF energy harvesting system test

E_{store} [mJ]	t [sec]	P_{input} [mW]	$P_{\text{converter}}$ [mW]	η [%]
121.1	3600	0.5092	0.00384	6.6

Table 5-8. Values in calculation of recharging efficiency using “voltage reference method” in the second experiment

E_{store} [mJ]	t_d [sec]	P_{input} [mW]	η [%]
140.9	118	0.5092	7.7

A comparison of the two experiments and their efficiencies are shown in Table 5-9.

Table 5-9. Comparison of two RF energy harvesting experiments and their efficiencies calculation

	Discharge load	“Capacitance modeling” efficiency	“Voltage reference” efficiency
First test	1 k Ω	5.8 %	6.5 %
Second test	500 Ω	6.6 %	7.7 %

In the typical operation of the PDS, four battery cells will be recharged in parallel, which will present an effective capacitance 4 times the single cell. In order to verify the RF recharging still works, a third test was run to recharge 4 batteries in parallel with the RF energy harvesting block.

Firstly, the batteries were discharged in series through a 1 k Ω load for over 14 minutes. As the blue discharge curve shown in Figure 5.27 the load voltage dropped from 4.90 V to 3.71 V. Note that the voltage is about four times as high as the previous experiments because four battery cells were placed in series. Secondly, the batteries were charged for 1 h by the RF energy harvesting block, with the walkie-talkie providing the power as the same way in previous experiments. Figure 5.28 shows the potential increase over the charging process (from 1.03 to 1.14 V). Finally, the battery was connected, again, to the 1 k Ω load for 283 s, in order to observe the second discharge. As shown in Figure 5.29, the battery started sourcing energy from 3.72 V. Compared to the load voltage prior to re-charging (3.71 V), the load voltage of the battery has increased after re-charging and the battery is successfully re-charged. Table 5-10 shows the charging efficiency calculation based on the “voltage reference calculation” in this test. The efficiency value with this method is 7.1 %. This is slightly smaller than the best value we have observed for single battery recharge. This may be caused by the internal resistance of battery cells that give rise to more power loss during recharging.

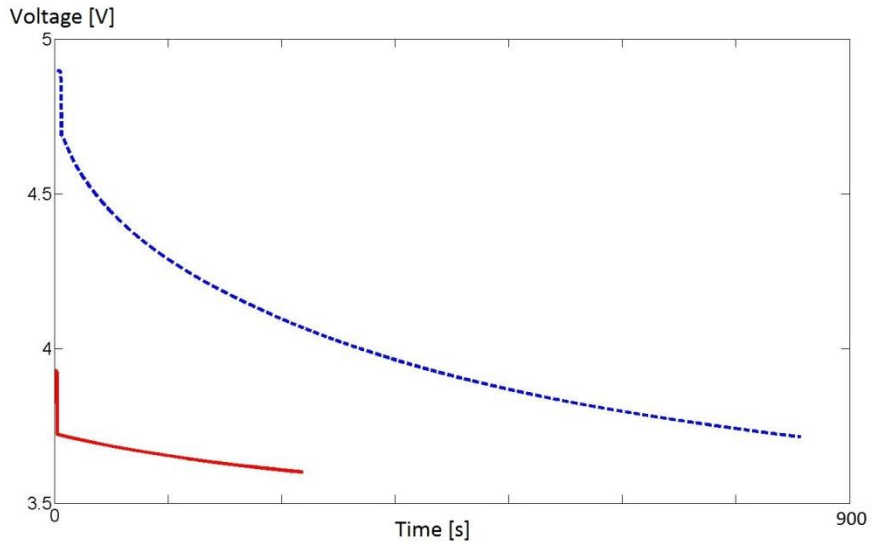


Figure 5.27. The two discharge profiles of four batteries recharging experiment

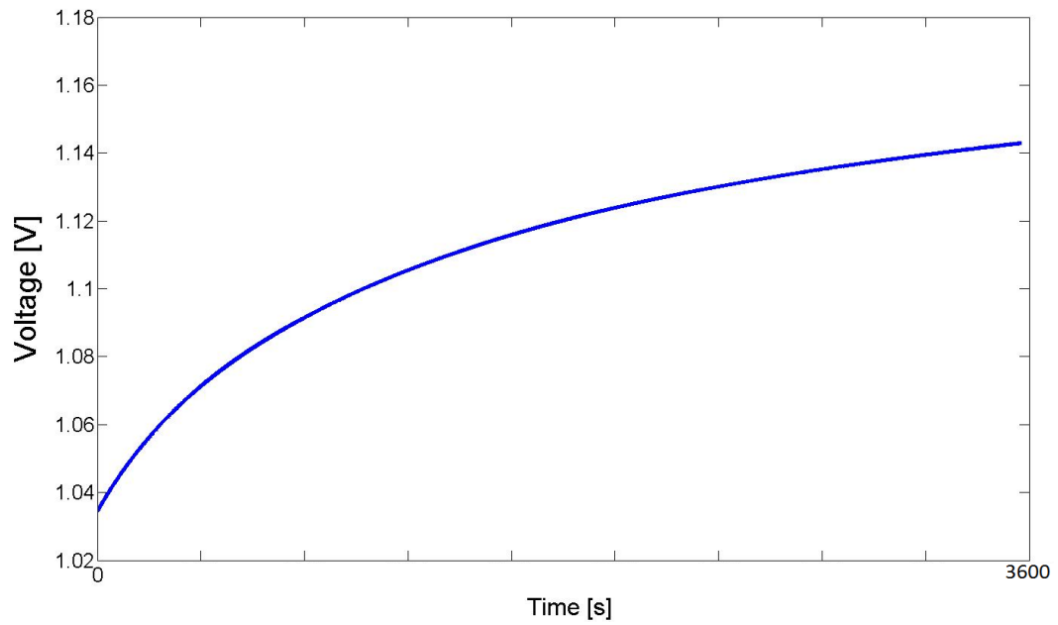


Figure 5.28. The voltage change during recharge of 4 batteries in parallel

Table 5-10. Values in calculation of recharging efficiency using “voltage reference method” in 4 battery experiment

E_{store} [mJ]	t_d [sec]	P_{input} [mW]	η [%]
130	11.4	0.5092	7.1

5.7 Discussions of the RF Energy Harvesting Experiments

Another way to measure the recharge process of a secondary battery is to measure the input voltage and current of the battery cell. This is not entirely accurate for the system described here. In that case described, a voltmeter and a current meter have to be used at the same time when performing the charging experiment. The resistance of the voltmeter, current meter and the internal resistance of the battery cell will all consume part the energy that we calculate by integrating the current and voltage over time. In other word, it will increase the apparent efficiency by spuriously including energy that is not stored in the battery cell (but rather, delivered to “parasitics.”) Additionally, the switching nature of the SC voltage converter makes the input current very difficult to measure as it appears to spike constantly. The voltage and current data were collected by the Agilent 34410 operated remotely by LabView. The sampling rate in the program is close to the SC converter switching frequency and thus is inaccurate to measure the exact input current directly. To address this issue, two other methods were developed and showed similar results as shown above. Therefore, the methods thus developed are fairly accurate ways to calculate the efficiency.

The harvesting experiments described here neglect the RF waves reflected from the building walls. The reflection coefficient of electromagnetic wave is defined as [78]:

$$\Gamma = \frac{Z_L - Z_S}{Z_L + Z_S} \quad (5-11)$$

where Z_S is the impedance toward the source, Z_L is the impedance toward the load. In the experiment, Z_S is the impedance of air, approximately 377 Ω . The impedance of building walls can be reasonably estimated to be that of concrete:

$$Z_S = \sqrt{\frac{\mu_S}{\epsilon_S}} \quad (5-12)$$

where μ_S is the magnetic permittivity and ϵ_S is the electrical permittivity. Most common dielectric materials, including concrete are nonmagnetic. It makes μ_S very close to that of air [79]. The relative electrical permittivity of concrete can be estimated to be 3. So $Z_S = \frac{Z_L}{\sqrt{3}}$, and $\Gamma = -0.268$, where the minus sign stands for a 180 degree phase shift. Reflectivity generally refers to the ratio of reflected electromagnetic wave power to the incident wave power, and is usually defined as the magnitude squared of the reflection coefficient [80]. In this case, the reflectivity is 0.07, which means only about 7 % of the radio waves hitting the walls will be reflected. Further, the reflected wave power will attenuate as $\frac{1}{r^2}$, where r is the distance that the waves travel. Assume the radio wave from the walkie talkie travels 3 m more to the nearest wall, and then travels another 3 m to the rectenna, the power density will decrease to be $\frac{1}{36}$ of the initial output. Combing the 7 % reflection ratio,

the power density of the reflected wave to the rectenna can be estimated to be $0.07 \times$

$\frac{1}{4\pi(36)} \approx 0.00015$. The direct incident power portion of the rectenna is

$\frac{1}{4\pi(0.5m)^2} = 0.32$, which is more than 3 magnitude larger. So the reflected part of the

power can be reasonably neglected.

Note that RF energy is an exceptionally weak environmental source. The input source in the experiment shown above was chosen largely for its availability and because it allows us to study charging efficiencies at the lower power extreme. Beamed sources are applicable in actual use for higher power needs. They emit over a limited solid angle (rather than over the full $4\pi^2$ of a non-directional antenna). For example, microwave magnetron type sources are available of 1000X the power output used in the study. The output from these sources can be beamed into a target area of approximately $10\lambda^2$ (where λ is the source wavelength), leading to at least one order of magnitude increase in power on target. Between the higher power of the source and the compact nature of the beam, a 10^4 X increase in incident energy is possible. Therefore, when operated in a beamed-energy mode, we can expect 0.1 – 1.0 W output power from our energy harvesting system.

5.8 Power Budget of the PDS

In order to operate normally, the PDS must have a positive net power. Otherwise, the microcontroller will shut down the system, and all the operations will be stopped. This section will examine each case with only one power source is

available. When multiple power sources are available, the PDS will have a larger net power budget.

Let us first examine the worst case scenario, when only RF energy is available. According to the previous experiment results, the energy stored in the battery cells is 130 mJ in 3600 s. The power can be provided by this harvested energy is 36.1 μW . The battery arrays provide power through a voltage regulator with an efficiency of 96 %. The final output power is therefore 34.7 μW . This power is used to drive the microcontroller and the possible load. As described previously, the microcontroller consumes less than 6 μW in standby mode, and 40 μW in operation. In practice, the microcontroller works in standby mode most of the time, and only executes the functions occasionally by sensing the voltages and providing commands. The real duty cycle depends on the application. If the load consumes comparatively more power, the duty cycle of microcontroller will be larger, since it needs to switch the battery arrays more often, and the frequency of giving commands to the system is higher. On the other hand, if the load does not consume much power, the duty cycle is smaller.

If the system is used in a situation where only RF energy is available, more likely than not, the load will be very power efficient (for example, a low power wireless sensor). The battery should be able to power the sensor for a very long time (likely several days) before it needs to be recharged. In a conservative estimation, let us assume the duty cycle is 20 %, which should be far larger than the practical situation. In this case, the average power consumption of the microcontroller will be:

$$P_{mc_ave} = 40\mu\text{W} \times 0.2 + 6\mu\text{W} \times 0.8 = 12.8\mu\text{W} \quad (5-13)$$

Therefore, the power can be delivered to the load is:

$$P_{load} = 34.7\mu\text{W} - 12.8\mu\text{W} = 21.9\mu\text{W} \quad (5-14)$$

As will be shown in Section 6.2, this power is sufficient to supply the needs of a low power wireless sensor node in normal operation (the power consumption is 19 μW).

If we calculate the total efficiency from receiving the RF power to the power that can be finally delivered to the load, it is:

$$\eta = \frac{P_{load}}{P_{in}} = \frac{21.9}{509.2} = 4.3\% \quad (5-15)$$

Note that in the experiment of RF energy harvesting, the input power source was placed to study the PDS performance at the lowest input power limit, and that is the data used to estimate the power budget here. If the input power level is higher, the efficiency will be higher, and the power budget will be better.

If only the solar energy is available, the solar cell in the PDS is able to provide about 100 mW under full sun condition. As shown in Section 5.1, the solar energy harvesting block is able to recharge at an efficiency of 47%. So the energy delivered to the battery is 47 mW. After the voltage regulation block, the output power becomes 45.1 mW. Even if we assume 100% duty cycle of the microcontroller (no standby mode), the power it consumes is only 40 μW , which would be negligible to the total power available.

The USB recharging block serves as a backup power source for the PDS. If a USB power port is available, the battery arrays will be charged up rapidly and the PDS will recover to full power conditions in minutes. The evaluation of the power budget in this scenario will be trivial.

5.9 Investigation of Alternative Solutions to the RF energy harvesting block

There are several other topologies in the literature for rectifier circuit used in RF energy harvesting. One of the widely used rectifier circuit is Villard voltage doubler. A multistage dual band RF energy harvester based on an resonant inductive coupler and Villard voltage doublers was reported by Li et al in [44] [81] [51] [82] [83].

Initial efforts were made to use this circuit topology in the PDS described here. Li has shown that the dual band energy harvester obtains over 9% efficiency for two different bands (900MHz and 1800MHz) at an input power as low as -19dBm. The DC output voltage of this harvester is over 1V. With the microstrip antenna and the dual band RF energy harvester Li also described, the circuit was able to generate 1 V from input powers as low as -3 dBm. This input power level was higher than that required by the RF energy harvesting block has achieved as shown in Section 5.6 utilizing the switched capacitor approach. Additionally, the output 1 V is not high enough to recharge the battery with its high capacitance. Li's results were generated

by an optimized resistive load not usable in the battery charging network described here.

The first test was run by using a receiving antenna and dual band RF energy harvester. The RF power came from a network analyzer through a coaxial cable and a transmitting antenna. The circuit was able to generate 0.2 V from an RF signal as low as -16.5 dBm at 940 MHz.

To be utilized in the PDS, a new RF energy harvesting block was formed by the receiving antenna and dual band RF energy harvester and the SC voltage converter described in Chapter 3. The input power was the same as described above, since 0.2 V is suitable to be boosted by the SC voltage converter and generate a voltage to recharge the battery. The normal operation of the SC voltage converter in the PDS is shown in Figure 5.29. The yellow waveform is the input signal, about 0.2 V constant. The blue waveform is the output signal, a square waveform with peak value of 1.4 V. And the output voltage of this new RF energy harvesting block was shown in Figure 5.30. The input voltage dropped to near zero when the six capacitors were shifted into parallel configuration for charging. And the output voltage was square wave but the peak value was only about 0.2 V. This was not enough to charge a large capacitor or the battery. This figure indicates that the SC voltage converter was not driven properly by the dual band RF energy harvester. The charge was not adding up to the expected value (six to seven times 0.2 V). This was because the RF energy harvester was not sourcing enough current (or power) to charge the capacitors in the SC voltage converter. So all the six capacitors were partially charged, and provide an output voltage much lower than the ideal value.



Figure 5.29. Normal operation of the SC voltage converter in the PDS (yellow waveform is the input signal, blue waveform is the output signal)



Figure 5.30. The operation of SC voltage converter working with the dual band (yellow waveform is the input signal, blue waveform is the output signal)

This RF energy harvesting block was then tested to charge two large capacitors, 100 μF and 2200 μF . The charging efficiency can be calculated as follows. Assuming the initial voltage of the capacitor is 0. The energy stored in the capacitor is:

$$E_{cap} = \frac{1}{2} CV_{sat}^2 \quad (5-16)$$

where V_{sat} is the saturation voltage of charging. The input energy of the block is:

$$E_{in} = P_{in} t \quad (5-17)$$

where P_{in} is the output power of the network analyzer, and t is the total charging time.

Therefore, the efficiency can be expressed as:

$$\eta = \frac{E_{cap}}{E_{in}} \quad (5-18)$$

Note that the efficiency calculation is a conservative estimation based on the assumption that all the power transmitted from the network analyzer is received by the circuits. However, this is not true because only part of the energy from the transmitting antenna will be received by the receiving antenna. Therefore, the calculation results of the efficiency will be smaller than what they really are. During experiments, the two antennas were placed at a certain distance and angle that the received power reaches the maximum value. The experiment results are summarized in Table 5-11. The results show that the capacitor can only be charged up to a fairly

low value. The larger the capacitance is, the lower the saturation voltage. The efficiency is also low.

Table 5-11. Large capacitors experiment results of the dual band RF energy harvesting block

Capacitor value [μF]	V_{sat} [V]	Charging time	P_{in} [dBm]	η [%]
100	0.27	2 minutes 8 seconds	-13	0.057
2200	0.03	5 minutes 30 seconds	-13	0.006

In order to generate a larger output voltage in the switched capacitors, and considering the weak driving ability of the circuits, smaller value capacitors were used in the SC voltage converter. The six 100 μF capacitors were replaced by 1 μF capacitors. The experiments were conducted again to observe the saturation voltages and efficiency. However, in this set of experiments, multiple clock frequencies were tested to find the optimum one for capacitors with new values. The test results are summarized in Table 5-12. It indicates that as the clock frequency increases, the charging time decreases, so the efficiency increases. In the table, only the highest efficiencies are shown. When charging the 2200 μF capacitor, the energy conversion efficiency reached 2.6 %. However, the saturation voltage was still not enough to be used in the PDS.

Table 5-12. Large capacitors experiment results of the dual band RF energy harvesting block with 1 μF capacitors in the SC voltage converter

Capacitor value [μF]	V_{sat} [V]	Charging time	P_{in} [dBm]	Clock frequency for SC converter [Hz]	η [%]
100	0.2	4 minutes	-12	2	N/A
100	0.2	3 minutes 34 seconds	-12	20	N/A
100	0.2	1 minute 26 seconds	-12	200	N/A
100	0.2	15 s	-12	2k	N/A
100	0.3	1 minute 18 seconds	-12	2k	N/A
100	0.2	2 s	-12	20k	1.6
100	0.3	7 s	-12	20k	1.07
2200	0.2	28 s	-12	20k	2.6

In conclusion, because of the comparatively weak driving ability of the dual band RF energy harvester, it is hard to make it compatible to the PDS described in this dissertation. The reason we chose a SC voltage boost converter is that it not only generates a higher voltage, but it uses capacitors to store the charges that are harvested as well, providing a better driving ability for supercapacitors and batteries

than the dual band RF energy harvester. However, as showed in this Section, this dual band RF energy harvesting block is capable for harvesting energy from very low power level, and has potential in different applications where the load does not require great driving ability.

Chapter 6: Potential Applications Design and Measurements

One of the earliest proposed applications of wireless powering is in the area of biology pacemaker [84]. In this dissertation, several potential applications have been designed or surveyed in the following sections for the proposed power distribution system, including an ultra-low power neural oscillator, a wireless sensor network and a prosthetics system [85]. This chapter provides a reference for future implementation of the PDS to the specific applications.

6.1 An Ultra-Low Power Tunable Neural Oscillator for Biological Rhythmic

Behaviors

6.1.1 Neuron Oscillation Overview

Animals, including humans, are systems of complicated neural networks [86]. The electrical properties of neuron cells, combining with synapses, enable brain circuits to perform the prodigious feats of computation that make intelligible the torrent of sensory information confronting us each second. By combining neurophysiologic principles with silicon engineering, researchers are able to produce analog integrated circuits with the functional characteristics of real nerve cells and synapses. The silicon neural system represents a step towards constructing artificial nervous systems that use more realistic principles of neural computation than existing electronic neural networks [87]. Biological neurons consist of a cell body with dendrites branching-out from it, and an axon emerging from the cell body generally in

the opposite direction. A typical neuron structure is shown in Figure 6.1. The majority of the neuron's surface (cell membrane) is covered with synaptic sites. Neurons communicate with each other via a variety of synaptic arrangements: Axodendritic (Axon to Dendrite), Dendrodendritic (Dendrite to Dendrite), Axoaxonic (Axon to Axon), and Reciprocal Synapses [88]. Mimicking the operation of neuron cells and synapses in silicon circuits is a subject of ongoing research interest. In addition to high-level features such as ability to perform complex pattern recognition and motor control, autonomous learning, adaptability etc. also the low-level features, such as robustness against noise and fault tolerance, make the brain-inspired system an attractive alternative computing model which could be appropriate for designing systems in contemporary and future integrated circuit technologies [89].

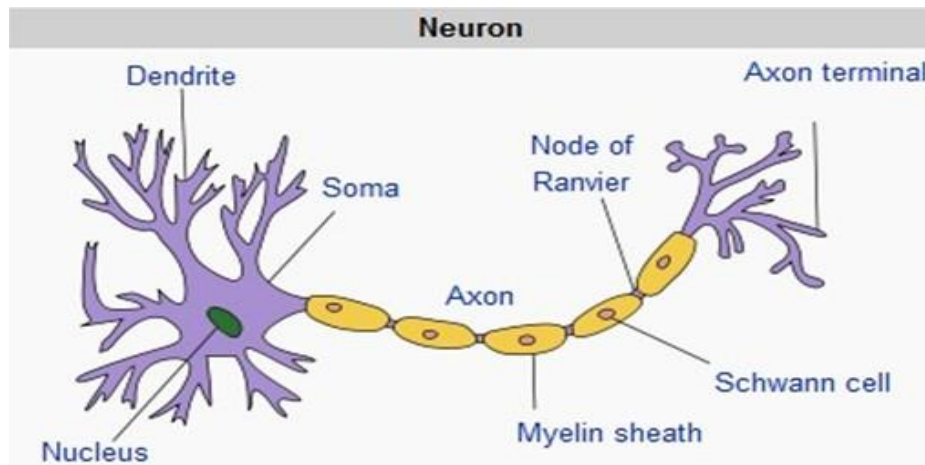


Figure 6.1. Structure of a typical neuron. Adapted from [90].

Among various functions of neural network, oscillatory or rhythmic behaviors exist in almost every animal and most of them are produced without receiving any particular extrinsic oscillatory stimulus [91]. Some of the earliest

experiments in physiology were aimed at understanding the underlying mechanisms of rhythmicity in nerve axons. The most obvious roles for rhythmic activity occur in motor activities such as animal gaits, respiratory rhythms, and feeding and mating patterns, and also in human electrocardiographic (ECG) and electroencephalographic (EEG) signals. There is a major line of research in the computational intelligence field that seeks to mimic a specific aspect of biological systems, i.e., their rhythmic nature, and exploits this feature for solving a wide class of problems encountered in biomedical and technical sciences [91].

An ultra-low power neural oscillator with tunable duty cycle and frequency is designed and simulated in Pspice 16 using 1.2um CMOS process [92]. The building blocks for this design are discussed in Section 6.1.2. In Section 6.1.3, analysis of the whole neural network will be presented. The simulation results in Pspice will be shown in section 6.1.4.

6.1.2 Research Background

The mathematical description of the neural oscillator is addressed in detail in Matsuoka's works [91]. He proved that neurons generate the rhythmic patterned output and analyzed the conditions necessary for the steady state oscillations. Because of the simplicity, the neuron model is very often used to design oscillator circuits. Part count and low power advantages obtained over other approaches such as the Stein neural model, the Van der Pol oscillator, and the HitzHugh-Nagumo model

[93]. In recent decades, more models for neural oscillator and different applications based on Matsuoka's work have been proposed [94].

Typically, a compact neural network is made up of neuron bodies and synapses. The research of spiking neuron models has started many decades ago, beginning with Hodgkin-Huxley's pioneering work in 1952 [95]. While this detailed approach produces a comparatively accurate model, it is computationally intensive and requires estimation of a large number of free parameters. Since then, many models have been made in order to reduce the complexity of the original one. Typically however, reducing the model complexity also reduces the biophysical accuracy and the number of neural behaviors that can be reproduced by the model [96]. The leaky integrate-and-fire (LIF) Model is an applicable to many theoretical studies in neurobiology. Izhikevich reviewed ten models including Hodgkin-Huxley and LIF, comparing them with his own approach [97]. His simplified approach (hereafter denoted as "IZH"), contains only two coupled differential equations and yet is able to reproduce many complex neural behaviors.

On the other hand, as a critical element in spike-based neural computation, synapse function is modeled in many different circuit implementations with different computational goals in mind. In many computations, a narrow, square pulse of current is all that is necessary to model the synaptic current. In other situations, a longer post-synaptic current profile is desirable to extend the effects of extremely short spike durations or to create a specific time window of interaction [98].

In this design, two circuits are integrated, one for neuron cell and another for synapse, and build a compact neural network achieving oscillation behavior based on

them. This novel neural oscillator is tunable in both frequency and duty cycle. The potential applications of this circuit include image texture analysis, robot control, artificial neural system design, etc. [86] [87] [94].

The model of neuron cell used in this dissertation starts with a report by Jayawan H. B. Wijekoon and Piotr Dudek [99]. The proposed circuit is loosely based on the Izhikevich neuron model [97]. The synapse circuit that this design based on is presented by Rock Z. Shi, and Horiuchi [100]. The circuit consists of eight transistors and one capacitor.

6.1.3 Circuit Structure and Operation

The block diagram of the oscillator is shown in Figure 6.2. It consists of 3 neuron circuits and 4 synapse circuits, with a Schmitt trigger to control the oscillation. The operation of each block is discussed below.

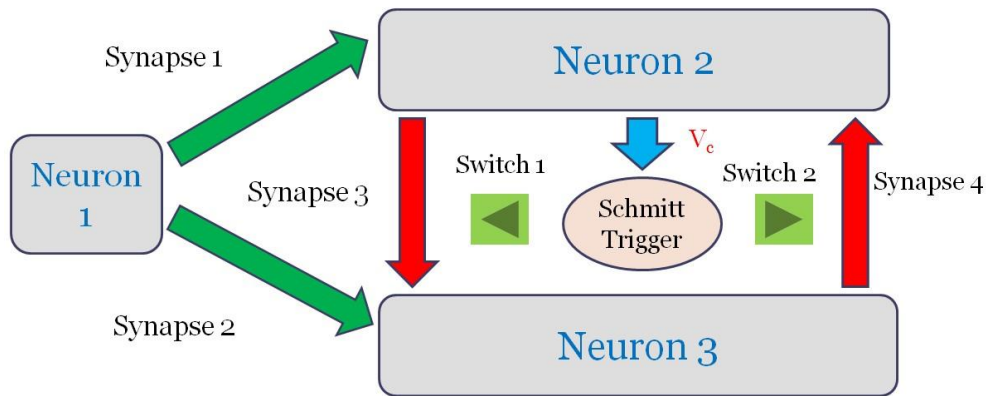


Figure 6.2. Block diagram of the oscillator

A. Neuron circuit

As shown in Figure 6.3, the implemented neuron model consists of two state variables: “membrane potential” (V) and “slow variable” (U) that are represented by voltages across capacitors C_v and C_u respectively. The circuit comprises three functional blocks: membrane potential circuit, slow variable circuit and comparator circuit (the transistors M1 and M2 are shared by the membrane potential and slow variable circuits). In the membrane potential circuit, the capacitor C_v integrates the postsynaptic input current, plus internal currents which depend on the state of the cell. Similarly, in the slow variable circuit the capacitor C_u integrates the currents that non-linearly depend on U and V . The comparator detects the spike and generates pulses (V_A and V_B) that perform the after-spike reset. Various spiking and bursting firing patterns are obtained by tuning two voltage parameters, V_c and V_d , which control the reset mechanism. Figure 6.4 shows the change of U and V with the input current. A detailed analysis of this circuit can be found in [99].

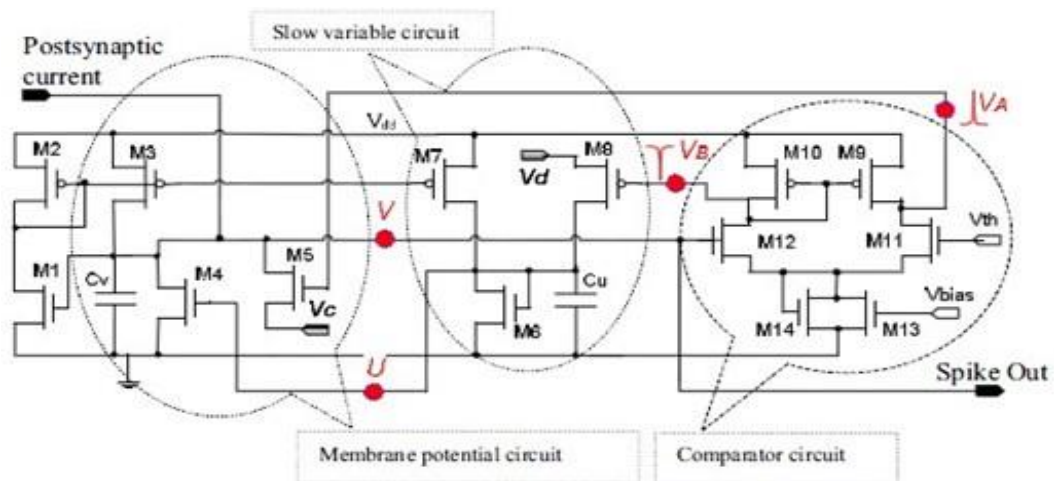


Figure 6.3. The compact silicon neuron circuit [99]

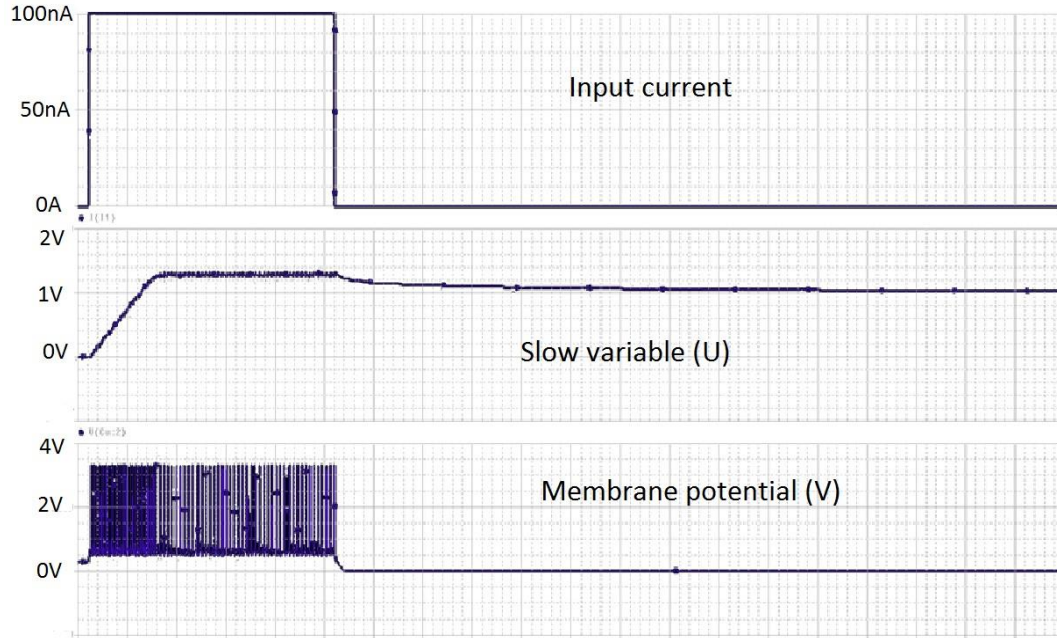


Figure 6.4. Change of Slow variable and Membrane potential with input

B. Synapse Circuit

As shown in Figure 6.5, all transistors are operated in the subthreshold region. Input voltage spikes are applied through an inverter (will be shown later) onto the gate of the PMOS M1. V_{τ} sets the current through M7 that determines the time constant of the output synaptic current. The voltage on the capacitor is converted to a current by transistor M6, sent through the current mirror M4 – M5, and into the source follower M3 – M4. The drain current of M8, a scaled copy of current through M6 produces an inhibitory current. A simple PMOS transistor with the same gate voltage as M5 can provide an excitatory synaptic current. Both of these two kinds of synapse configuration will be used in the oscillator design. A more detailed analysis can be found in [100].

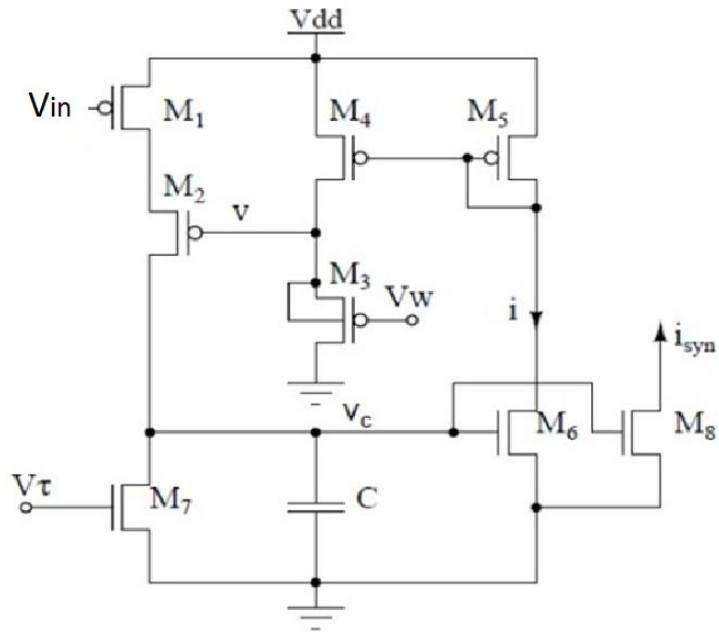


Figure 6.5. Circuit diagram of the synapse [100]

C. Schmitt Trigger

A Schmitt Trigger (ST) is implemented to control the oscillation. The circuit structure is shown in Figure 6.6 and the typical transfer curves of the Schmitt trigger are shown in Figure 6.7. Curve A in Figure 6.6 corresponds to the output of the Schmitt trigger changing from a low to a high, while curve B corresponds to the output of the Schmitt trigger changing from a high to a low. The hysteresis present in the transfer curves is used to control the system.

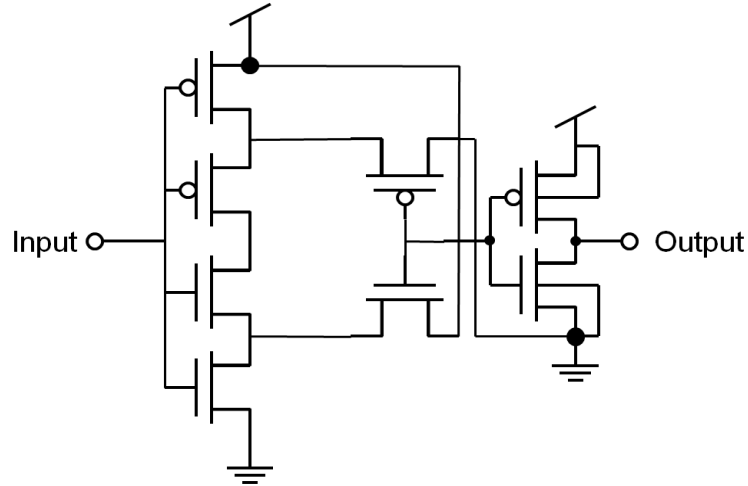


Figure 6.6. Circuit diagram of the Schmitt Trigger

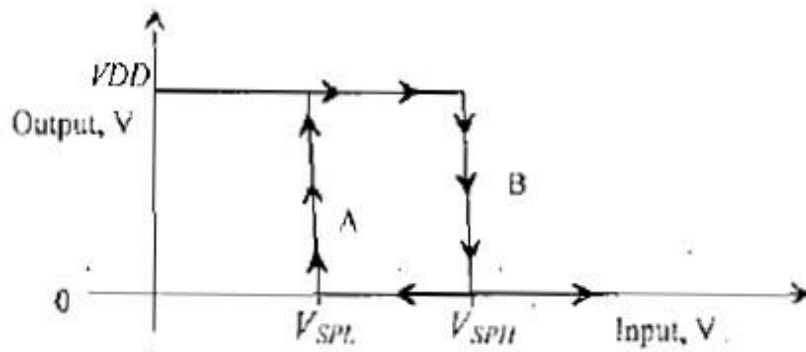


Figure 6.7. Schematic and transfer curves of Schmitt trigger

A detailed analysis of the ST can be found in [55]. The relationship between the transition voltages and the size of transistors is given by the following equations:

$$\frac{\beta_1}{\beta_2} = \frac{W_1 L_3}{L_1 W_3} = \left(\frac{VDD - V_{SPH}}{V_{SPH} - V_{THN}} \right)^2 \quad (6-1)$$

$$\frac{\beta_5}{\beta_6} = \frac{W_5 L_6}{L_5 W_6} = \left(\frac{V_{SPL}}{VDD - V_{SPL} - V_{THP}} \right)^2 \quad (6-2)$$

D. Oscillation

As shown in Figure 6.2, Neuron 1 serves as a driving source for Neuron 2 and Neuron 3. Its firing must be continuously to maintain oscillation in the system. It releases excitatory synaptic pulses, shown as green arrows that serve as input to the oscillating pair. Neuron 2 and 3 fire one after another. And while one of them is firing, it creates neural inhibition, shown as red arrows, to prevent the other one from becoming active.

The control block of this system is a Schmitt Trigger (ST). It receives signal from Neuron 2 (discussed in next paragraph), and provides a digital signal to control two switches (digital use of nFET). However, Switch 1 is directly controlled by the output of ST, while Switch 2 is controlled by the ST through an inverter. So the two switches are controlled in opposite logic levels. Here, Switch 1 enables Synapse 3, and Switch 2 enables Synapse 4, so only one inhibitory synapse will be effective, that is, only one neuron (neuron 2 or 3) will fire, while the other one will be silenced by the inhibitory synapse.

The exact input of the ST is V_c in Synapse 3, the voltage of capacitor C as shown in Fig. 3. Simulation shows that V_c increases when neuron 2 fires; and V_c decreases when neuron 2 is inactive. Consider that at beginning neuron 2 is firing and neuron 3 is inhibited by synapse 3 from neuron 2. Therefore, the input of the ST (V_c) increases until it reaches the upper high transition voltage of the trigger, V_{SPH} , then the trigger's output flips from 1 to 0; and that flip will change the states of the two switches, turning Switch 1 on and Switch 2 off, which shuts off synapse 3 and turns on synapse 4. And synapse 4 starts to suck current out of neuron 2's input, so neuron 2 stops firing, and neuron 3 becomes active. Then, V_c will decrease until it reaches

the lower limit of Schmitt trigger (V_{SPL}), and the trigger flips back, completing a whole period of the oscillation.

E. Tunability

1) Duty cycle: From previous analysis, it could be inferred that the firing time for neuron 2 in one period is determined by the rising speed of V_c in synapse 3, and the firing time for neuron 3 is determined by the falling time of the same voltage. So tuning the rise and fall times would change the duty cycle. This speed is also the charging speed of the capacitor C in synapse 3, shown in Fig. 4, which is controlled by V_τ . By adjusting this bias voltage, we are able to achieve variable duty cycles.

2) Frequency: Since the input voltage of the Schmitt trigger is confined between two transition voltages of the trigger, the frequency of oscillation is controlled by the difference of those two voltages, namely V_{SPH} and V_{SPL} . If the difference is small, the time for V_c to move between them would be small, and the frequency would be large, and vice versa. The range of operation frequency is determined by $V_{SPH} - V_{SPL}$, which could be designed to close to 0, or close to the supply voltage. The switching speed of the circuit is another important factor that affects the frequency range. The frequency is not determined by Neuron 1 (the driving neuron).

6.1.4 Simulation Results

The design is constructed with 1.2 μm CMOS process in Pspice 16.01. It consists of 90 transistors, with a supply voltage of 5 V. Note that in the simulation results, the spikes are so dense that they look like solid rectangles.

1) Symmetrical Oscillation: A 1 μA constant current input is applied to the source neuron (neuron 1 in Figure 6.3). Neuron 2 and 3 are set to be completely symmetrical. The transition voltages of the Schmitt trigger are $V_{\text{SPH}}=1.1$ V, and $V_{\text{SPL}}=1.3$ V. The transient simulation result is shown in Fig. 6. It could be seen that after a certain amount of time to stabilize, the oscillating pair starts to fire symmetrically. In this case, the oscillating frequency is 20 kHz. The total power dissipation is 75 μW . This power consumption is larger than the power stored in the battery cell in experiment described in Chapter 5 (39.1 μW). However, the experiment only tested the RF energy harvesting with a comparatively weak power source. With the help of solar energy harvesting block and the USB recharging block in the PDS, or with a stronger RF power source, this power consumption can be easily satisfied. The red (light) part represents neuron 2, and the blue (dark) part stands for neuron 3, shown in Figure. 6.8.

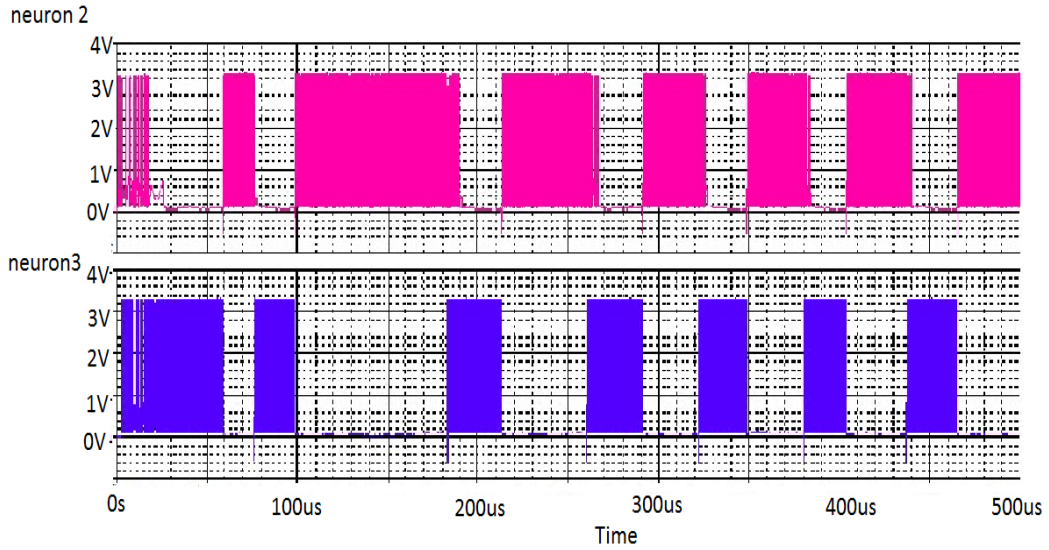


Figure 6.8. Symmetrical oscillation

2) Tuning of duty cycle and frequency: According to the analysis in Section 6.1.3, duty cycle of this oscillator is controlled by V_τ in neuron 2. Figure 6.9 shows a simulation result of different V_τ (0.64V for the upper figure, and 0.62V for the lower one). It can be seen that a larger V_τ gives rise to a larger duty cycle of neuron 2, which is consistent with the previous analysis. Again, red part is neuron 2, and blue part is neuron 3.

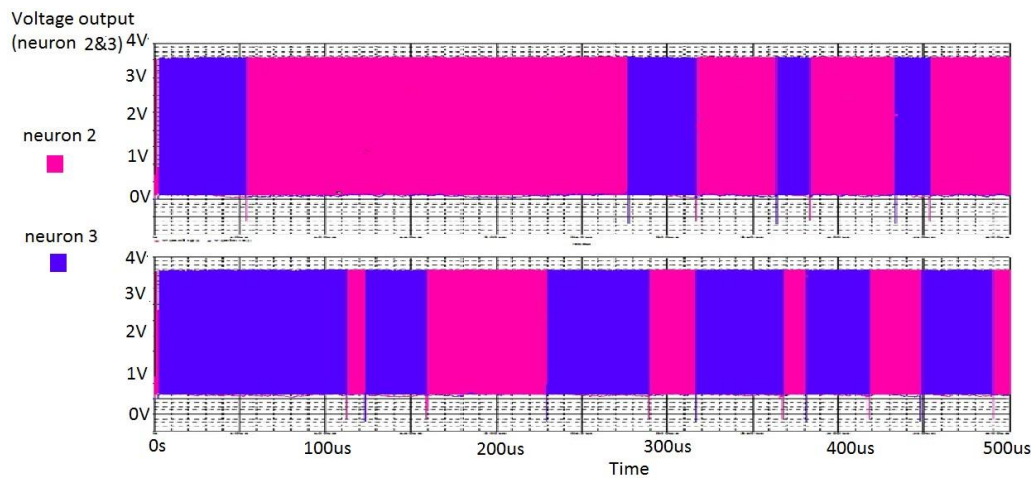


Figure 6.9. Tuning of the duty cycle

Also, the tuning of frequency is realized by adjusting the difference between V_{SPH} and V_{SPL} of the Schmitt trigger. The following figures show different frequencies of the oscillator. Figure 6.10 sets $V_{SPH}=1.1V$ and $V_{SPL}=1.3V$, while Figure 6.11 uses $V_{SPH}=1.2V$ and $V_{SPL}=1.6V$. The frequency of former oscillating pattern is 20 KHz, which is larger than 3.7 kHz, the latter one's frequency.

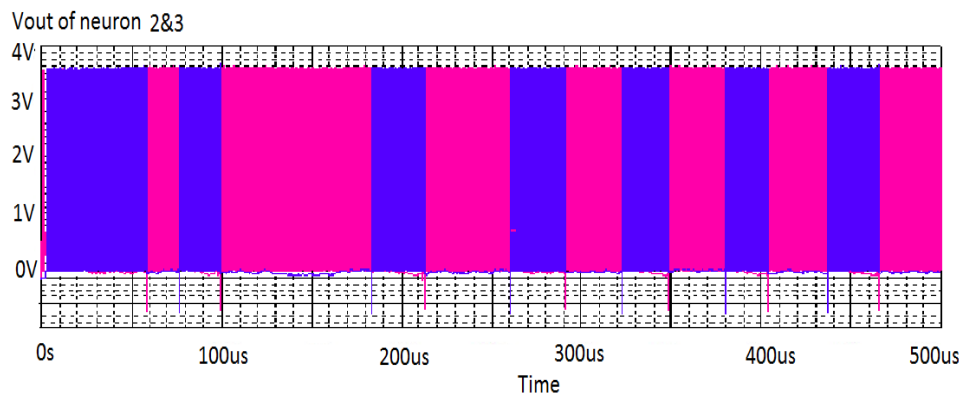


Figure 6.10. High frequency oscillation

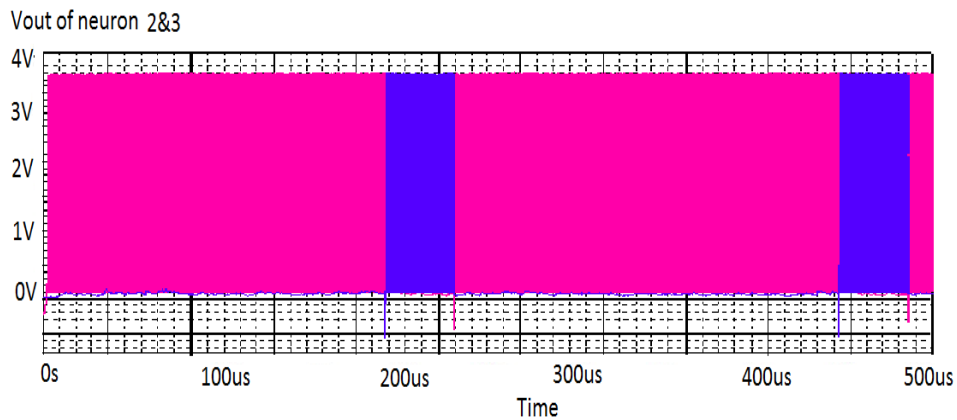


Figure 6.11. Low frequency oscillation

6.2 Wireless Sensor Networks

As described in Chapter 1, the wireless sensor network (WSN) has become a prominent area of system research and is enjoying broad application in pervasive computing, location tracking, and health monitoring of medical patients and commercial buildings [3]. A WSN is composed of sensor nodes which could be powered by batteries or harvesting ambient energy from the surrounding environment. Typical ambient energy sources include solar energy, radio frequency (RF) energy, thermal energy, whose power densities are a few tens to hundreds of $\mu\text{W}/\text{cm}^3$. The PDS presented in this thesis can serve as the core part to power a wireless sensor.

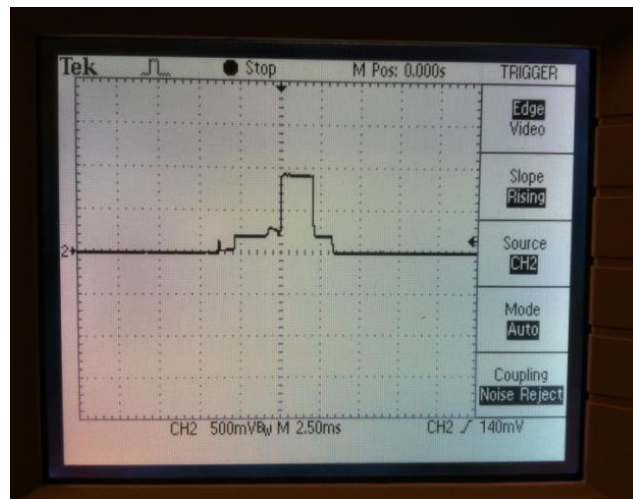
As a case study, we consider energy consumption of industrial wireless sensors for distributed wireless monitoring. We make use of the data obtained from Resensys SenSpot sensors [101], which have the target applications of structural monitoring and wireless distributed sensing in industrial settings. Figure 6.12 displays a captured plot of a Resensys SenSpot sensor current consumption during a typical measurement of the RF transmission of a 100-byte long packet at a power level of 16 dBm. While capturing this plot the time axis is at 2.5 ms per division and the vertical axis has 200 mV per division. Careful inspection of this plot shows that during transmission, the sensor consumes energy in three intervals:

(1) An interval with length of 3ms, during which the voltage across the 4.7Ω resistor is 200 mV. Therefore, the current consumption of the sensor is $200 \text{ mV}/4.7 \Omega=42 \text{ mA}$. The total energy consumed during this interval is $24 \text{ mA} \times 1.8 \text{ V} \times 3 \text{ ms}=130 \mu\text{J}$.

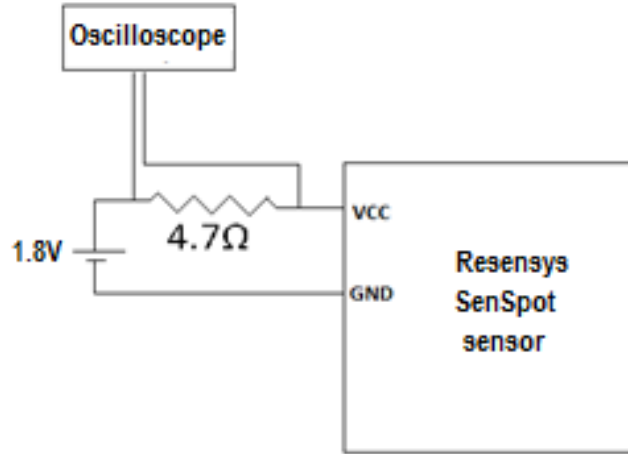
(2) A second interval with length of 2ms during which the voltage across the 4.7Ω resistor is 490mV. Therefore, the current consumption of the sensor is $490 \text{ mV} / 4.7 \Omega = 104 \text{ mA}$. The total energy consumed during this interval is $104 \text{ mA} \times 1.8 \text{ V} \times 2 \text{ ms} = 374 \mu\text{J}$.

(3) A third interval with length of 1.5ms, during which the voltage across the 4.7Ω resistor is 200mV. Therefore, the current consumption of the sensor is $200 \text{ mV} / 4.7 \Omega = 42 \text{ mA}$. The total energy consumed during this interval is $42 \text{ mA} \times 1.8 \text{ V} \times 1.5 \text{ ms} = 65 \mu\text{J}$.

By adding together the energy values consumed in the above three intervals, the total energy consumption of the sensor for transmission of a 100 byte packet is calculated to be $569 \mu\text{J}$.



(a)



(b)

Figure 6.12. Current consumption of a Resensys sensor while sensing and transmitting. The left circuit shows the utilized test circuit (picture, courtesy of Resensys LLC, www.resensys.com).

To calculate the average energy consumption, we further assume that the period of taking samples and transmitting them is 30 s. As a result, the total power consumption of the sensor is calculated by dividing the total energy during each 30-s interval by the duration:

$$P_1 = \frac{E}{T} = \frac{569 \mu J}{30 s} = 19 \mu W \quad (6-3)$$

In comparison, the average power stored in our RF energy harvesting block is $140.9 \text{ mJ}/3600 \text{ s} = 39.1 \mu \text{W}$, as shown in Chapter 5. If the PDS was employed with only RF power available, the average output power is $21.9 \mu \text{W}$. In both of the scenarios, it is sufficient to drive the sensor. As mentioned, the input power is chosen to be exceptionally weak in the test. Higher output power is expected with a stronger input source.

It must be noted that the above power includes the RF transmission and measuring samples. The other source of power consumption in Resensys SenSpot sensors is the consumed energy during sleep mode. However, while in sleep mode, the current consumption is about $0.1 \mu\text{A}$ (or $0.18 \mu\text{W}$ at 1.8 V), which is negligible compared to the energy consumption required for taking samples and RF transmission.

Figure 6.13 shows the sensor running experiment with three batteries in series. The test was run for 24 hours. The sensor was working normally until the batteries dried out at the end of the test. One point worth mentioning is that the batteries' package was not optimized in this test. Better sealed package is available which would prolong the lifetime of the batteries significantly.

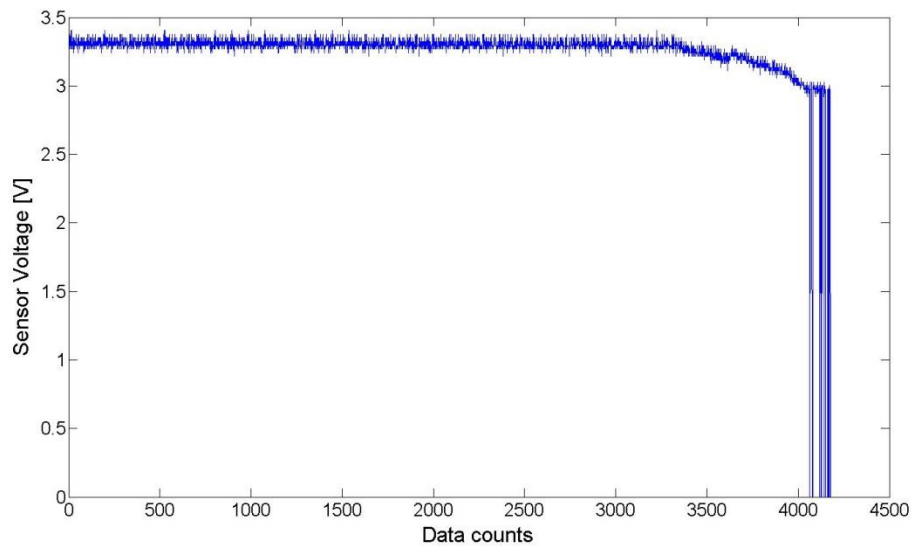


Figure 6.13. Resensys sensor running test for 24 hours with 3 battery cells in series

Due to the low power density level of the harvested energy, power management issues need to be addressed carefully to make optimal usage of the harvested energy, and special attention should be taken to design ultra-low power and high efficiency power management modules. The potential fluctuations appearing in the power source would disturb degrade the function of high sensitivity circuits of the load. As a result, a voltage regulator is needed to ensure that a stable voltage is available to the load electronics even when potential fluctuations appear in the power source. In the PDS, a commercial regulator was used to achieve this goal.

6.3 Brief Examination of a Prosthetics System

One possible duty cycle and the energy need of an electronic device that operate prosthetics for a run time of 1 year are listed in Table 6-1.

Table 6-1. Cycle of a Prosthetic Electronic Device

Power [mW]	Pulse duration [s]	Sleep Power [μ W]	Pulse Interval [s]	Run Time [days]	Total Energy [Wh/ye]
200	0.8	25	10	365	132

The specific volumetric capacity of the Zn-RuO₂·xH₂O battery is in the range of 233-500 mAh/cm³, with an average capacity of 367 mAh/cm³. One can consider that a volume of 30 cm³ is available for the power source in the prosthetic device. These specifications afford the calculations shown in Table 6-2, where the first

column contains specific volumetric capacity values obtained per unit volume of the power system. Listed are the capacity and energy values for the maximum, minimum, and the average capacity value of the zinc-ruthenium (IV) oxide cell described in this paper.

Table 6-2. Run times calculated for a prosthetic device operated with a 3 cm³ Zn-RuO₂·xH₂O battery

	Sp. Capacity [mAh cm ⁻³]	Energy [Wh]	Run Time [da]
Minimum	233	6.99	19.3
Maximum	500	15.0	41.5
Average	367	11.0	30.4

As demonstrated by data in Table 6-2, the ultrathin battery can supply energy meeting the requirements for the prosthetic device operated as in Table 6-2 for 19.3-41.5 days. As these batteries are suitable for being recharged by solar cells and RF energy, they offer a significant capability for extending the above operation time.

While RF energy is emphasized as the input source in this paper, the system is also suitable for use in many other energy harvesting schemes, including solar energy harvesting. Light intensity for outdoor lighting conditions typically corresponds to 10-100 mW/cm² [102]. This energy can be harvested at the power density of at least 15 mW/cm² [103]. A solar panel with 4 cm² footprint and 50 μm thickness [104] (its total volume being 0.02 cm³) can harvest 480 mWh energy per day (assuming 8 h of daylight). Consider the prosthetics system discussed above. In order to operate the

device according to the duty cycle in Table 6-1, a daily average energy of 361.4 mWh is needed. Hence, the harvested energy can cover for the power need of the device; namely, it can operate the prosthetic device by daylight and, in the meanwhile, can recharge, at 75 % efficiency, the Zn-RuO₂·xH₂O battery system, which takes over the powering by night or during unfavorable meteorological conditions. A great advantage of the flexible power source over the traditional volumetric batteries is that it can be distributed evenly over the prosthetic surface. Some other scavengers considered include vibrational and thermoelectric devices.

6.4 An Evaluation of Powering Unmanned Aerial Vehicles (UAVs)

A UAV is defined as “a powered, aerial vehicle that does not carry a human operator, uses aerodynamic forces to provide vehicle lift, can fly autonomously or be piloted remotely”. These devices have been increasingly used in recent years in a wide range of applications, including: weather and atmospheric research, reconnaissance and surveillance, conventional combat roles, and, most notably, in military mission areas, commonly categorized as “the dull, the dirty, and the dangerous” [105] [106]. The most challenging problem in a modern UAV refers to the source of power [107]. Two commonly used power sources for UAVs are batteries or fuel. However, the electric powered UAV provides a relatively longer endurance capability, and it is also considered to be environment friendly in terms of emissions free and silent propulsion [108]. But the endurance of such aircrafts is restricted by the energy storage capacity of the battery. Several other energy sources

have been studied to increase the endurance, and solar power system attracts the most attention [107]. However, solar cells cannot provide enough energy at night or when the UAV flies in shadows or cloudy weather. This brings up the need for intermediate energy storage between the solar cells and the UAV, and the need for other energy sources to provide extra power.

An ideal system would be flexible, capable of drawing energy from a variety of sources, storing that energy and delivering it to the empowered system. The system described in this dissertation is aimed at assessing the transduction efficiency of the various components of such a system, as well as the grouped efficiency of the completed system. While the RF source used cannot, of itself, propel the UAV, multiple, low energy sources, will contribute significantly to the propulsion and operating budget of the aircraft without impinging on payload volume or overall system weight.

A commercially available radio controlled Ember 2 airplane and an airplane motor EM400 with an EP1260 propeller were tested with battery banks [109]. Their photos are shown in Figure 6.14 and Figure 6.15. The power requirements for them are summarized in Table 6-3.

Table 6-3. Power requirements of the tested airplane and motor

Airplane/ Motor	Voltage	Current	Power	Battery capacity
Ember 2	3.7 V	350 mA	1.3 W	70 mAh
EM 400 (motor)	7.2 V	1.3 A	9.36 W	N/A



Figure 6.14. Ember 2 airplane



Figure 6.15. EM400 motor with EP1260 propeller

Conservatively in calculation, the Ember 2 airplane can be operated with a battery bank, which consists of 16 ultrathin batteries, connected 4 in parallel to form a high power module, with 4 such modules in series, for supplying the required voltage. Such a battery bank can source 1 A current at a voltage exceeding 3.7 V for at least 6 minutes, which enables the flight of the airplane with all the added battery mass. Since the batteries are very light and thin, more batteries can be easily stacked to increase the run time.

The total mass of 16 galvanic cells is currently in the mass range of 25.5-26.5 g, which is comparable to the mass of the airplane (ca. 16.5 g), but exceeds the mass of the currently used Li-Polymer battery (ca. 3.4 g). We aim, however, to further reduce the mass of our batteries by (i) thinning down the packaging materials, (ii) thinning the electrodes, and (iii) stacking ultrathin batteries, which would enable for

using both sides of the zinc anode, while also allows to save on the mass of packaging materials (using one case for the battery bank, rather than one separate case for each individual cell). The packaging materials represent 11.2 - 13.5 wt.% of the total mass of an individual galvanic cell, hence, packaging together 6-8 batteries in the same case would save ca. 10 wt.% of the overall mass, as compared to the mass of individually packaged cells. Also, the weight of the intermediate storage system is distributed over the flight surfaces of the airframe and does not intrude in the cargo volume, as a battery does. All these developments should bring the equivalent mass/endurance of the battery bank comparable to that offered by the Li-Polymer battery, offering the advantage of a more uniform mass distribution along the wings and a chemistry, which is safe in operation and do not pose any environmental threats. As the storage system is spread over the airframe, it does not impinge on the cargo volume of the UAV.

Based on the analysis, several tests were run to verify the possibility of powering the Ember 2 airplane with the batteries, as shown in Figure 6.16. Each test ran for more than 10 minutes and the change of voltage was measured. The following figures show the measurement results with different battery configurations. Figure 6.17 shows the experiment in which 2 batteries are used in series as a group, and 3 such groups are employed to power the airplane. Figure 6.18 shows the experiment with 3 batteries in series as a group, and 3 such groups are used to power the airplane. Figure 6.19 shows the experiment in which 4 batteries are used in series as a group, and 3 such groups are employed to power the airplane. The battery number in series determines the voltage level, and the group number determines the current sourcing

ability. The batteries' voltage decreased as the plane motor kept running. The results show that 4 batteries in series and 2 groups in parallel have the best voltage profile among the three. The plane motor didn't stop in any of the test.



Figure 6.16. Ember 2 airplane and battery arrays

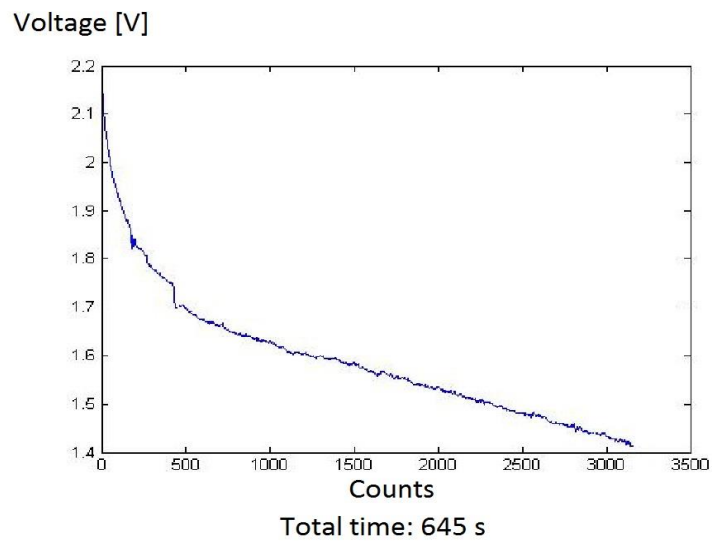


Figure 6.17. The Ember 2 airplane test with 2 batteries in series as a group, and 3 such groups in total to power the airplane

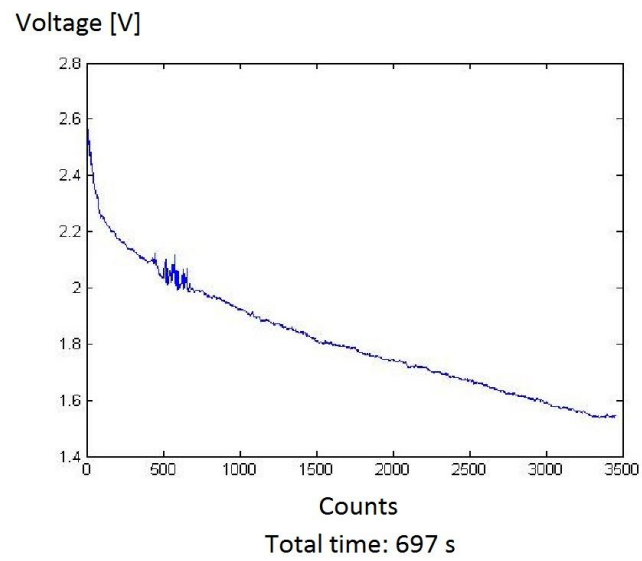


Figure 6.18. The Ember 2 airplane test with 3 batteries in series as a group, and 3 such groups in total to power the airplane

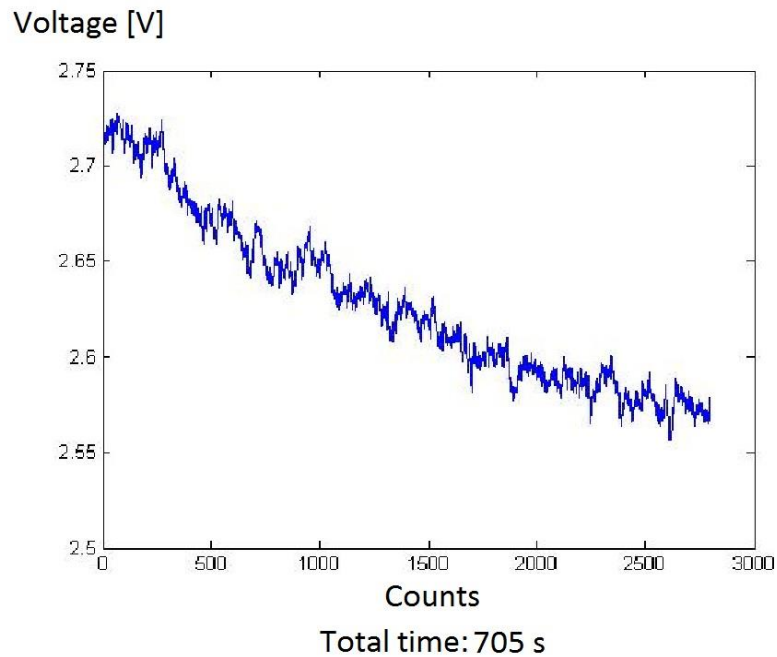
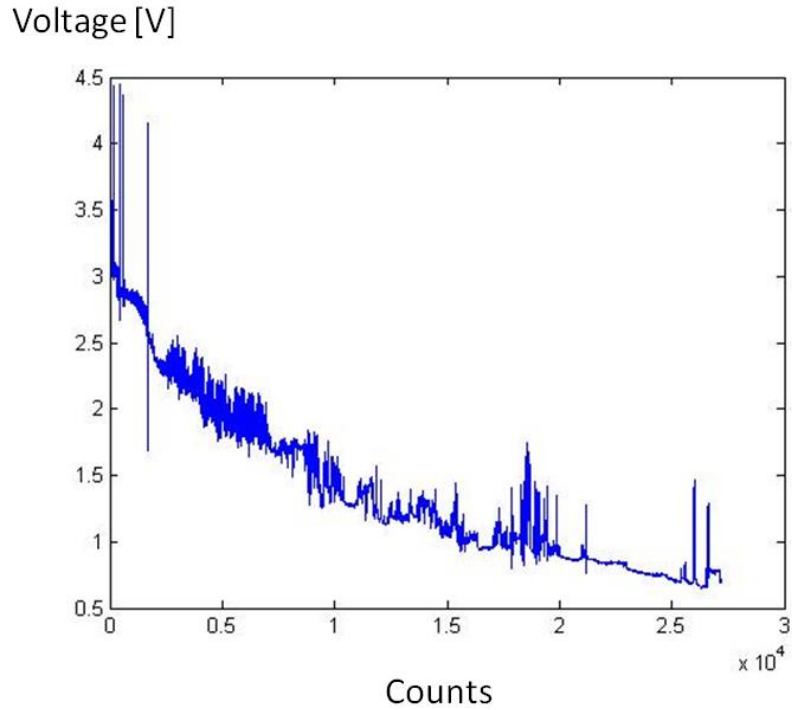


Figure 6.19. The Ember 2 airplane test with 4 batteries in series as a group, and 2 such groups in total to power the airplane

In the last test of Ember 2 airplane, 4 batteries were connected in series and 3 such groups were used. The battery bank kept running the plane for over 3 hours (11060 s to be exact) until the motor stops. Figure 6.20 shows the voltage change during the experiment. Note that in all the Ember 2 airplane tests, the plane was not allowed to fly for testing purpose. But the plane was able to run forward at a high speed if it could.



Total time: over 3 hours

Figure 6.20. The Ember 2 airplane test with 4 batteries in series as a group, and 3 such groups in total to power the airplane for over 3 hours

The EM400 motor with EP1260 was also tested with 4 batteries in series as a group, and 2 groups in total to power them. The voltage profile during the test was shown in Figure 6.21. The propeller was running during the whole experiment.

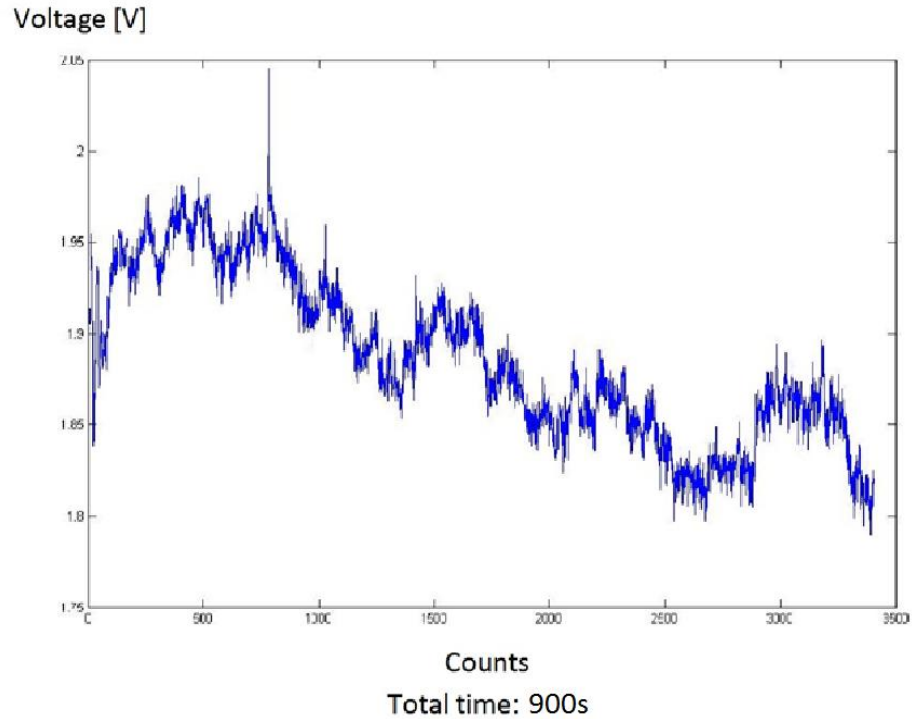


Figure 6.21. The EM400 motor and EP1260 propeller test with 4 batteries in series as a group, and 2 such groups in total for 900 s

The commercially available off the shelf (COTS) batteries for UAVs are typically Lithium Polymer batteries, which have a specific power of as high as nearly 2400 W/kg and energies on the order of 140 to 160 Wh/kg [110], which is currently better than our battery. However, the battery cell described in this paper has several advantages over COTS batteries. Advantages include burst power energy supply, a thin and flexible format, low recharging voltage and non-toxicity. Additionally, because of the thin and flexible format, the batteries can be easily mounted on the wings of airplanes, as shown in Figure 6.22. They can also be easily stacked to create more driving power. Although the specific power and energy are important factors in the market of UAVs, the flexible battery presented in this thesis is another

competitive option as a power source. Further improvements are needed in both batteries cells and the energy harvesting system for PDS to be utilized in UAVs.



Figure 6.22. Battery banks mounted an UAV wing

Chapter 7: Conclusions

7.1 Summary of Contributions

Driven by the development of autonomous wireless electronic systems, energy harvesting has gained increasing interest from academia as well as industry. The power distribution system this thesis presented is a multi-source integration including energy harvesting, power conditioning, energy storage and power regulation. The system is to meet the power management demands of low power applications such as ad hoc distributed networks. It is adjustable in several blocks and is able to provide a variety of outputs and functions. The solutions provided by this system for energy harvesting and power distribution in general can be adopted in many forms by modifying one or a few sub-blocks.

The radio frequency energy harvesting block proposed in the PDS addresses two fundamental challenges in RF energy harvesting: how to harvest the RF energy while it is so weak, and how to use the RF energy efficiently. A literature survey is conducted to prove that there is usable RF energy in the ambient space with vastly different power densities, frequency values, polarizations and other signal characteristics. Consequently, the RF energy harvesting block utilizes a wide band rectenna with frequency independent elements in order to receive RF energy as much as possible. The rectenna design weighs the tradeoff between wide receiving band and high energy conversion efficiency. If a specific RF signal frequency is targeted in an application, the wide band rectenna can be easily replaced by a rectenna focusing on single frequency and the efficiency will be higher.

The system adopted a Ruthenium based flexible thin film battery as the energy storage medium. This secondary battery cell enjoys exceptionally low recharge voltage and the highest specific energy capacity in all known thin film batteries, which is very suitable for RF energy harvesting. The thesis studied the charging requirements of the battery cell when it's used in a RF energy harvesting block.

In order to recharge the battery from the weak RF power, the voltage must be boosted with comparatively high efficiency. A switched capacitor voltage boost converter was designed and fabricated in both an IC version and a PCB version. It is chosen because its comparatively high efficiency and compact design form. The converter is able to provide output up to seven times the input voltage. Chapter 3 analyzes the operation and the major power losses in the converter. A number of experiments were conducted to verify the functionality of the circuit. It is able to drive loads such as super capacitors and battery cells.

The whole RF energy harvesting block includes the broad band rectenna, the SC voltage boost converter and the Ruthenium based thin film battery cell. The RF block was able to harvest energy from a commercially available walkie talkie from power density as low as $30 \mu\text{W}/\text{cm}^2$, and store the energy in the battery cell with total energy conversion efficiency up to 7.7%. The efficiency calculation is a conservative estimation assuming the power source was transmitting at maximum power all the time. This block is the first demonstration to harvest RF energy with a broad band rectenna and store the energy in a Ruthenium based thin film battery cell. The block structure is proven to be successful and is useful in many applications.

A survey of different energy harvesting schemes was completed before integrating the power distribution system. The RF block is used as the core of the system, and more functional blocks are included. A solar cell recharging block is constructed by a solar cell and a charging protection circuit. The circuit uses negative feedback mechanism to prevent the battery from over charging. It also controls the current to flow in only one direction. A USB recharging block is implemented as the backup power source. At the output end, the system includes a voltage regulator to improve the battery discharge profile and provide stable output to the load. Two battery arrays serve as the energy storage block. Each array consists of 4 flexible thin film battery cells. They are in parallel format when they are recharged in parallel and in series when they provide power to the load.

The whole system is controlled by a self-programmed ultra-low power microcontroller. The source code is developed in C. It smartly chooses the best power source available, monitors the battery array status and controls the system operation. It determines which battery array to use and which one to recharge. A four channel user select switch can provide flexibility to users to choose which energy source they want. The microcontroller will shut down the whole system when there is not enough energy to harvest in the ambient space or from USB. A prototype PCB is designed and fabricated including most of the components in the PDS.

The functions of all the blocks in the PDS were tested and verified. The system provides a complete solution for low power applications aiming at ambient energy as its power source.

An alternative of the RF energy harvesting block was described and tested to verify its compatibility with the system. It is a dual band harvester utilizing multi-stage voltage doubler circuits. It is able to harvest RF energy from as low as -25.5 dBm and generate 1 V across an optimized load. But it is not capable of driving the SC voltage boost converter by receiving the RF power from an antenna. In order to use it in the PDS, a redesign of the antenna and the output stage of the harvester may be needed.

Several potential applications of the PDS were investigated. An ultra-low power analog neural oscillator was designed. It is tunable in both frequency and duty cycle. It can be used in brain-inspired circuits, VLSI systems for spiking neural networks simulations and hybrid silicon/biology systems with the PDS as its power source. A wireless sensor node from Resensys was characterized in its power consumption and tested with the battery cell. Its extremely low power consumption can be powered solely by the RF energy harvesting block in the PDS. A medical prosthetics system was measured and characterized focusing on its power consumption. It is introduced as a potential application to the PDS by means of solar energy harvesting. A number of experiments were run to use different battery banks powering a commercial UAV and a motor/propeller combine. The thin film battery cells can be distributed on the plane body since they can be easily stacked or folded. Although the ambient RF energy may be too weak to power a UAV, solar energy and high power beaming can provide more stable power supply to it.

7.2 Future Work

7.2.1 Possible Improvements of the Power Distribution System

The PDS presented in this thesis has demonstrated its various functions successfully through extensive experiments. The next step to improve the PDS would be to fully integrate all the components onto the same board. Some subsystem elements are still off the board, such as the wide band rectenna, the solar cell and the battery arrays. The PCB described in the thesis is prototype test board. Eventually, the final board design would include every component on it.

Due to the restrictions of RF source in the lab, the RF block was only tested by a commercially walkie talkie at a specific frequency 900 MHz. Experiments with signals of multiple frequencies and power levels will be helpful to verify the wide band performance of the RF block. Expected experiment results of the rectenna can be found in [15]. Additionally, the solar cell block was only tested by an artificial indoor light source, due to the difficulties to conduct the experiments under full sun conditions with all the necessary lab equipments. However, the specifications provided by [62] could provide some projections of the possible performance of the system under full sun conditions.

As discussed in Chapter 2, the ambient RF signals have multiple frequencies, power levels and polarizations. Therefore, the rectenna chosen in the PDS is wide band in order to harvest as much power as possible at the same time. However, the wide band feature is achieved by sacrificing matching the impedance in almost all the frequency bands, thus decreasing the energy conversion efficiency. A wide band antenna with a tunable matching network is able to provide a solution to conquer this

dilemma. A basic block diagram for such kind of system is shown in Figure 7.1. The tuning network should be controlled by a sensing system that knows the strongest signal frequency in the ambient space and modify the matching network to provide maximum power transfer. The matching network can be constructed by capacitors, inductors and controlling switches. The capacitors and inductors could be either on-chip or off-chip. We can expect that the more accurate the matching network is constructed to be, the more components will be needed.

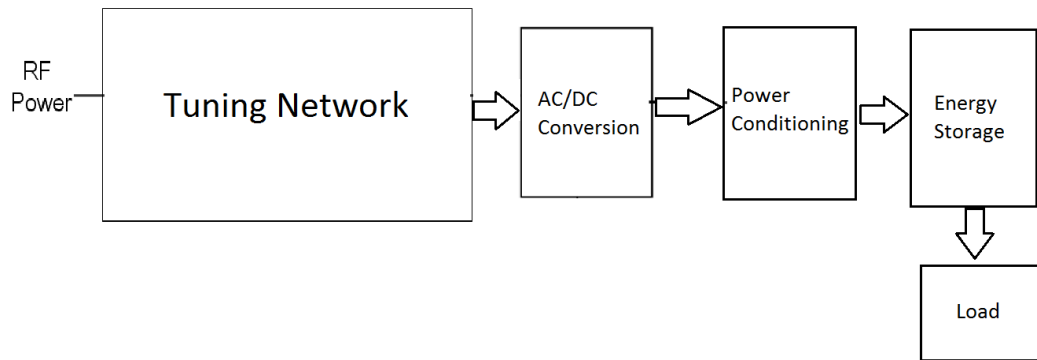


Figure 7.1. Power distribution system with a tuning network to match the impedance while keep the wide band harvesting feature

Power management circuit is the core of a PDS. In the case of solar energy harvesting block, it is important to track the point of maximal generated power (referred as MPP for maximum power point). Figure 7.2 shows a typical I-V and P-V curves of a solar cell with the mark of MPP. However, as the MPP varies with irradiance and temperature [3], an MPP tracker (MPPT) is often used in modern solar energy harvesting to extract the maximum power. It typically includes a dc to dc converter and an algorithm to control the operation. The controller will force the solar

cell to work at (or near) MPP regardless of the load or input conditions. The dc to dc converter can be implemented by several topologies introduced in Chapter 1, such as the switching voltage converter and SC voltage converter. In the case of low power solar energy harvesting, the MPPT circuit must be power efficient, and the algorithm design should be simple. Based on the control mechanism, the MPPT methods can be categorized into two classes: direct and indirect. The direct control methodology is closed loop and characteristics of the solar cell are needed beforehand. The indirect method is open loop and the control is based on empirical database. Therefore, an MPPT circuit could be implemented in the future to improve the system performance in terms of solar energy harvesting. A few methods for achieving MPPT in low power system have been reported recently [111] [112] [113].

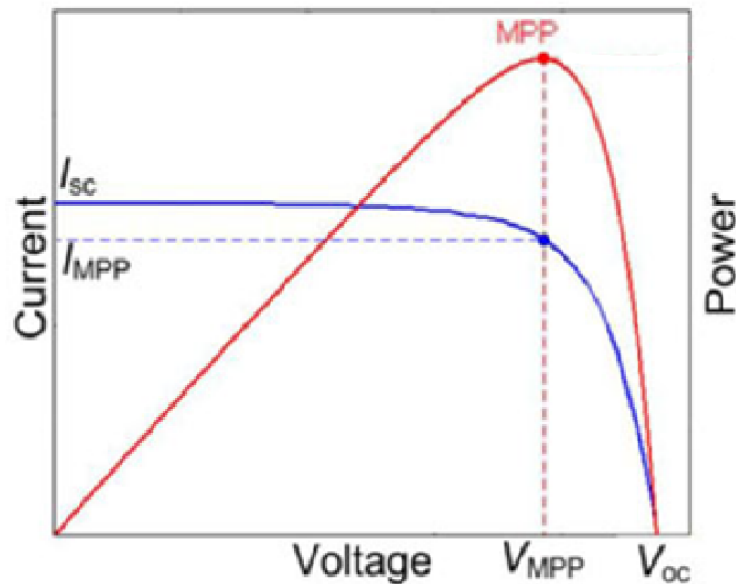


Figure 7.2. I-V and P-V curves of a typical solar cell with the MPP marked

In the current PDS in this thesis, only one power source is utilized at a time. One possible future direction is to harvest energy from multiple sources simultaneously. This may require more battery arrays and control implementations. The energy from different sources has to be conditioned and stored without conflicts and used to drive the loads together. While only three harvesting schemes are implemented in the system, more energy sources can be employed to expand the harvesting ability of the PDS depending on the specific applications. Possible additions may include vibrational energy, thermal energy, electromagnetic energy and biochemical energy.

7.2.2 Future Research Trends and Challenges in Energy Harvesting

Energy harvesting has been an interesting research topic for a few decades, and great effort has been made in related research and commercialization, especially in large scale power generation. However, the low power energy harvesting still has tremendous research potential and there are many outstanding issues to address.

There are basically two major challenges faced by the researchers of energy harvesting focusing on low power applications. First, the amount of power harvested by the devices using various schemes is usually too small to power most of the electronic applications directly. Second, a standard design guideline for low power energy harvesting systems has not been established. Depending on the applications and power sources, the system design procedure and parameter requirements are vastly different. The key technologies in this field would be finding the innovative

methods to condition and store the weak power from the ambient space. These are the challenges that this thesis is trying to address and provide solutions for.

Currently most of the research in the literature focuses on how to design the harvesting devices, instead of trying to construct a system that could efficiently store the energy and use it. Even less literature research connects the potential applications to the harvesting scheme and emphasizes the power management issues. More application specific approaches and design method are needed to utilize the current technologies of low power energy harvesting. One of the barriers in low power distribution system design is the lack of a standard process for designers to characterize the power source, choose the proper circuits for power conditioning, select the energy storage medium and develop the suitable control algorithm for a specific application. Therefore, such design process guideline is necessary in the future and it takes extensive efforts to develop it by studying key parameters and models in a power distribution system.

The trend to integrate more than one energy source in a single system is also necessary to overcome the shortcomings of each power source. The whole system should be totally stand alone and is able to withstand the temporary lack of any source due to regular or special reasons. Experiments are needed to prove the reliability and robustness of the system and energy harvesting techniques before using them in practice. This integration will be made easier if a standard can be established to compare the characteristics and capabilities of different energy sources in order to implement them into the same design.

Finally, the design of a power distribution system is a complicated project involving the characterization of available power sources, harvester materials/devices selection, signal conditioning circuit design, power management optimization, storage medium implementation, control algorithm and interface between different blocks and the load. More future studies are needed to address these issues in an integrated perspective, which requires knowledge in several different disciplines.

7.3 Conclusions

Energy harvesting has become a prominent research area and continues to grow in aspects such as materials, circuits design and system integration. Typical energy sources include solar energy, thermal energy, kinetic energy and RF energy. While RF energy exists almost ubiquitously in the environment, it is usually very weak. These features have made RF energy a viable source for low power electronics, yet very challenging to obtain significant amounts of energy fast and efficiently from the ambience. This thesis reports an end-to-end power distribution system with a focus on RF energy harvesting.

In the RF energy harvesting block, a broadband dual-circularly polarized spiral “rectenna” was designed and fabricated. A rectenna is a hybrid of antennas and Schottky diodes. It is designed based on Harmonic Balance analysis, performed in the frequency domain Fourier space and divides the circuit into a linear and a nonlinear part. The whole rectenna consists of 16 single spiral elements.

A switched capacitor voltage boost converter was designed and fabricated using the IBM 8RF LM 130 nm CMOS process with 6-2 metal option. It can be used

with six external capacitors and provides a maximum available output voltage seven times the input voltage. A user can select the output multiplication factor from the minimum (1x input) to the maximum (7x input). The converter has been tested to charge large capacitors and secondary batteries, with an efficiency as high as 40.53%.

A lightweight flexible thin film battery cell is equipped with a metallic zinc anode and hydrated ruthenium (IV) oxide cathode. In a power delivery system it provides the desired properties of both capacitors and galvanic cells and can be recharged at an exceptionally low voltage of 1.2 V. Also, the cell demonstrates a specific charge capacity of 84.4 mAh/cm² of projected electrode area, which is, so far, the largest value reported for thin film cells. Furthermore, the battery is less than 0.5 mm thick (prior to the optimization of packaging materials) and flexible. As the battery utilizes aqueous electrolytes, it is safe to operate in a number of settings and surroundings.

An RF energy harvesting block including all three components described above was tested with a commercially available walkie-talkie was used as an RF source generator, placed at 0.5 m distance from the rectenna. It operates at 900 MHz with a maximum output power of 1 W. The system was able to collect the weak RF power and condition it to store in the battery cell. The energy conversion efficiency is as high as 7.7 %. Besides the RF energy harvesting block, the PDS includes a solar energy harvesting block, a USB recharging block, a customer selection block, two battery arrays, a control block and an output regulation block.

A number of potential applications are also investigated including an ultra-low power tunable neural oscillator, a wireless sensor used in large scale networks, medical prosthetics and unmanned aerial vehicles.

Appendix A: Original C Code for the Microcontroller (excluding the library files that are called)

header.h

```
//- Description      :  
//-                  Common Header File  
//-----  
-----  
  
// Definitions section  
#ifndef __HEADER_  
#define __HEADER_  
  
//-----  
-----  
  
// Include section  
//-----  
-----  
  
#include "Lib6819\periph.h"  
#include "Lib6819\macro.h"  
#include "Lib6819\Types.h"  
#include "Lib6819\ports.h"  
#include "Lib6819\vld.h"  
#include "Lib6819\clock.h"  
#include "Lib6819\timers.h"  
#include "Lib6819\irqmsk.h"  
#include "Lib6819\watchdog.h"  
#include "Lib6819\slpcntwakeup.h"  
#include "Lib6819\pwrmodes.h"  
  
#include "sysinitialize.h"  
#include "howto_vld.h"  
#include "customerselection.h"  
#endif
```

howto_vld.h

```
//function prototypes  
//-----  
//-----  
  
void fConfigVLD_main_VS2(void);  
void fConfigVLD_Backup(void);  
void fConfigVLD_SupplyNode_VS1(void);
```

```

void fConfigVLD_SenseA_USB(void);
void fConfigVLD_SenseB_Light(void);
void fConfigVLD_SenseC_RF(void);

void fCheckVLDLevel(void);
void fdelayMS ( UINT16 n );

#define MICROSECONDS          1000000
#define SECONDSINMIN          60
#define MILISECOND            1000

#define CLOCKPERIOD           125      // Clock Period based
on 8 Khz clock
#define SLEEP_TIME            1       // SC time-out

#define Aswitch               BIT0
#define Bswitch               BIT3
#define Cswitch               BIT4
#define Dswitch               BIT2
#define Dbarswitch           BIT3
#define Eswitch               BIT7
#define TurnOFFSys           BIT7

void fPowerSaveMode(void);
void fConfigStartSC(void);

UINT16 fSetTimeSleepCounter_s (UINT16 time);
UINT16 fSetTimeSleepCounter_min (UINT16 time);

howto_vld.c
//- Description      :
//-                  Configure the level detector in the
microcontroller
//-----
-----

#include "header.h"
#include "howto_vld.h"

volatile UINT8 timer_expired; // flag for TIME-BASE
interrupt

/*****
*
fConfigVLD:

```

Configures VLD level,VLD source and enables the
VLD

```
*****  
*/  
  
void fConfigVLD_main_VS2(void)  
{  
    Config_VLD(VLDLEVEL_main_VS2,VLDSOURCE_main_VS2);  
    VLD_Enable();  
}  
  
void fConfigVLD_Backup(void)  
{  
    Config_VLD(VLDLEVEL_Backup,VLDSOURCE_Backup);  
    VLD_Enable();  
}  
  
void fConfigVLD_SupplyNode_VS1(void)  
{  
  
Config_VLD(VLDLEVEL_SupplyNode_VS1,VLDSOURCE_SupplyNode_VS1);  
    VLD_Enable();  
}  
  
void fConfigVLD_SenseA_USB(void)  
{  
    Config_VLD(VLDLEVEL_SenseA_USB,VLDSOURCE_SenseA_USB);  
    VLD_Enable();  
}  
  
void fConfigVLD_SenseB_Light(void)  
{  
    Config_VLD(VLDLEVEL_SenseB_Light,VLDSOURCE_SenseB_Light);  
    VLD_Enable();  
}  
  
void fConfigVLD_SenseC_RF(void)  
{  
    Config_VLD(VLDLEVEL_SenseC_RF,VLDSOURCE_SenseC_RF);  
    VLD_Enable();  
}  
/*****  
*  
fRunVLD:  
  
    Check if the Voltage is Below the VLD Level,is so Blink  
LED D7  
  
*****  
*/
```

```

// void fTim34_config (void)
// {
//   Tim34_Enable();
//   Tim34_SelStart_Clk(TimSelStart_SW,Tim3SelClk_PR1CK9);
//   Timer34_AR_En();
//   Tim3_Int_FullValue();
//   Tim34_SetFullValue(1000);
//   En_IRQ_Tim3();
// }

void fCheckVLDLevel(void)
{

    fConfigVLD_SupplyNode_VS1();
    if(is_level_below_VLD) // if supply node voltage<3V (VS1<3)
//ERROR here
    {

        SetBit(RegPCDOut,Dswitch); //D=1
//   ClrBit(RegPCDOut,Dbarswitch); //Dbar=0
        SetBit(RegPBDOut,Eswitch); //Turn on E

//   fdelayMS (10000); //delay 10s
//switch to Dbar when
Vmain>1.2
        fConfigVLD_main_VS2();
        while(is_level_below_VLD) //wait until main_bat>1.2
// NO ERROR here
        {
            ;
        }
        if(is_level_below_VLD==0) //if main_bat>1.2
        {

//   SetBit(RegPCDOut,Dbarswitch); //Dbar=1
//   ClrBit(RegPCDOut,Dswitch); //D=0
        }
        fConfigVLD_Backup(); //Turn off E when Vbackup>1.2
        while(is_level_below_VLD)
        {
//   fdelayMS (50); //check it every 500ms
            ;
        }
        if(is_level_below_VLD==0) //if backup_bat>1.2
        {
            ClrBit(RegPBDOut,Eswitch); //turn off E
        }
    }
}

```

```

}

/*****
*
fdelayMS:
    generate 1ms delay for clock settings as per
fSysInitilize()
    Actual delay will be n*1ms

e.g. if n=10;delay will be 10 ms

*****/

void fdelayMS ( UINT16 n )
{
    unsigned int i;

        while (n--)                // n*1 ms delay
        {
            ;
        }
}

/*-----
--
fConfigStart_SC:
    Configure Sleep Counter
    Set sleep wakup time-out time and Start sleep
counter
-----*/
void fConfigStartSC(void)
{

    SC_Enable();
    En_IRQ_SlpCnt();
    SC_Stop();
    fSetTimeSleepCounter_s (10); // set sleep wakup time-out
    SC_Start();

}

/*-----
--
fSetTimeSleepCounter_s:
    set sleep counter time-out in seconds
parameter :
    Parameter "time" is integer value in the range [1, 59]
return:

```

```

        return 1 if parameter is beyond range,otherwise echo
"time"
-----
*/

UINT16 fSetTimeSleepCounter_s (UINT16 time)
{
    if((time>59)|| (time<1))return(1);
    SC_timeout(((MICROSECONDS/CLOCKPERIOD)*time));
    return(time);
}

/*-----
--
fSetTimeSleepCounter_min:
        set sleep counter time-out in minutes
parameter :
        Parameter "time" is integer value in the range [1, 30]
return:
        return 1 if parameter is beyond range,otherwise echo
"time"
-----
*/

UINT16 fSetTimeSleepCounter_min (UINT16 time)
{
    if((time>30)|| (time<1))return(1);

SC_timeout(((MICROSECONDS/CLOCKPERIOD)*(time*SECONDSINMIN)));
    return(time);
}

```

IROHandler.c

```

/*
#include "Types.h"
#include "Macro.h"
#include "Periph.h"
#include "timers.h"
#include "slpcntwakeup.h"

extern volatile unsigned int Dflag;
extern volatile unsigned int UserSelect;
/*****
*****/
// IRQ Level 0
/*****
*****/
#if 0 //unused handlers should be #if'ed out. The linker
script will take care of them

```

```

void Handle_Irq_PMMiss (void)
{
    // Handles the interruption from Program memory, wait
    introduction
}
#endif

#if 0 //unused handlers should be #if'ed out. The linker
script will take care of them
void Handle_Irq_ADC (void)
{
    // Handles the interruption from ADC conversion finished
}
#endif

#if 0 //unused handlers should be #if'ed out. The linker
script will take care of them
void Handle_Irq_Prescl1Hz (void)
{
    // Handles the interruption from Prescaler1 1Hz (Pr1-Ck[0]
falling edge)
}
#endif

#if 0 //unused handlers should be #if'ed out. The linker
script will take care of them
void Handle_Irq_Tim1 (void)
{
}
}
#endif

#if 0 //unused handlers should be #if'ed out. The linker
script will take care of them
void Handle_Irq_Port0 (void)
{
    // Handles the interruption from PA0 or PC0, positive
and/or negative edge
}
}
#endif

/*****
*****/
// IRQ Level 1
/*****
*****/

#if 0 //unused handlers should be #if'ed out. The linker
script will take care of them
void Handle_Irq_SPI_START (void)
{
    // Handles the interruption from SPI, Start transmission
1byte
}
}
#endif

```

```

#if 0 //unused handlers should be #if'ed out. The linker
script will take care of them
void Handle_Irq_SPI_STOP (void)
{
    // Handles the interruption from SPI, Stop transmission 1
byte
}
#endif
#if 0 //unused handlers should be #if'ed out. The linker
script will take care of them
void Handle_Irq_PresclB (void)
{
    // Handles the interruption from Prescaler 1, 8Hz or
32Hz (falling edge)
}
#endif
#if 0 //unused handlers should be #if'ed out. The linker
script will take care of them
void Handle_Irq_OpAmp (void)
{
    // Handles the interruption from Comparator; falling
and/or rising output change
}
#endif
#if 1 //unused handlers should be #if'ed out. The linker
script will take care of them

void Handle_Irq_Tim3 (void)
{
    ToggleBit(RegPCDOut,BIT3);

}
#endif
#if 0 //unused handlers should be #if'ed out. The linker
script will take care of them
void Handle_Irq_Tim4 (void)
{
    // Handles the interruption from Timer2, Input capture,
Compare value, Compare Full
}
#endif
#if 0 //unused handlers should be #if'ed out. The linker
script will take care of them
void Handle_Irq_Port1 (void)
{
    // Handles the interruption from PA1 or PC1, positive
and/or negative edge
}
#endif

```

```

#if 0 //unused handlers should be #if'ed out. The linker
script will take care of them
void Handle_Irq_Port2 (void)
{
    // Handles the interruption from PA2 or PC2, positive
and/or negative edge
}
#endif

/*****
*****/

// IRQ Level 2

/*****
*****/
#if 0 //unused handlers should be #if'ed out. The linker
script will take care of them
void Handle_Irq_Tim2 (void)
{
    // Handles the interruption from Timer4, Input capture,
Compare value, Compare Full
}
#endif
#if 1 //unused handlers should be #if'ed out. The linker
script will take care of them
void Handle_Irq_Port3 (void)
{
    UserSelect=1;
}
#endif
#if 1 //unused handlers should be #if'ed out. The linker
script will take care of them
void Handle_Irq_Port4 (void)
{
    UserSelect=2;
}
#endif
#if 1 //unused handlers should be #if'ed out. The linker
script will take care of them
void Handle_Irq_Port5 (void)
{
    UserSelect=3;
}
#endif
#if 0 //unused handlers should be #if'ed out. The linker
script will take care of them
//#pragma Handle_Irq_Port6
void Handle_Irq_Port6 (void)
{
    // Handles the interruption from PA6 or PC6, positive and/or
negative edge
}

```

```

}
#endif
#if 0 //unused handlers should be #if'ed out. The linker
script will take care of them
void Handle_Irq_Port7 (void)
{
    // Handles the interruption from PA7 or PC7, positive
and/or negative edge
}
#endif
//#if 0 //unused handlers should be #if'ed out. The linker
script will take care of them
//extern UINT8 sleep_wakeup_flag;
void Handle_Irq_SlpCnt (void)
{
    ToggleBit(RegPCDOut,0x04); // to observe in case of ms
// Handles the interruption from Sleep counter wakeup timeout
}
//#endif
#if 0 //unused handlers should be #if'ed out. The linker
script will take care of them
void Handle_Irq_VLD (void)
{
    // Handles the interruption from Voltage level detector;
input low
}
#endif

/*****
*****/

```

irqmsk.h

```

#ifndef _IRQMSK_
#define _IRQMSK_

/*-----*/
-----*/
// RegInt0 sources
//-----
-

#define En_IRQ_PmMiss()           SetBit ( RegInt0Msk,
Int0MskPmMiss )
#define Dis_IRQ_PmMiss()        ClrBit ( RegInt0Msk,
Int0MskPmMiss )

#define En_IRQ_GASP()           SetBit ( RegInt0Msk,
Int0MskGasp )
#define Dis_IRQ_GASP()        ClrBit ( RegInt0Msk,
Int0MskGasp )

```

```

#define En_IRQ_DoCPM()           SetBit ( RegInt0Msk,
Int0MskDoCPM )
#define Dis_IRQ_DoCPM()         ClrBit ( RegInt0Msk,
Int0MskDoCPM )

#define En_IRQ_DoCDM()           SetBit ( RegInt0Msk,
Int0MskDoCDM )
#define Dis_IRQ_DoCDM()         ClrBit ( RegInt0Msk,
Int0MskDoCDM )

#define En_IRQ_ADC()             SetBit ( RegInt0Msk,
Int0MskADC )
#define Dis_IRQ_ADC()           ClrBit ( RegInt0Msk,
Int0MskADC )

#define En_IRQ_Psc11Hz()         SetBit ( RegInt0Msk,
Int0MskPsc11Hz )
#define Dis_IRQ_Psc11Hz()       ClrBit ( RegInt0Msk,
Int0MskPsc11Hz )

#define En_IRQ_Tim1()            SetBit ( RegInt0Msk,
Int0MskTim1 )
#define Dis_IRQ_Tim1()          ClrBit ( RegInt0Msk,
Int0MskTim1 )

#define En_IRQ_Port0()           SetBit ( RegInt0Msk,
Int0MskPort_0 )
#define Dis_IRQ_Port0()         ClrBit ( RegInt0Msk,
Int0MskPort_0 )

//-----
-
// RegInt1 sources
//-----
-
#define En_IRQ_SPIStart()        SetBit ( RegInt1Msk,
Int1MskSPIStart )
#define Dis_IRQ_SPIStart()       ClrBit ( RegInt1Msk,
Int1MskSPIStart )

#define En_IRQ_SPIStop()         SetBit ( RegInt1Msk,
Int1MskSPIStop )
#define Dis_IRQ_SPIStop()        ClrBit ( RegInt1Msk,
Int1MskSPIStop )

#define En_IRQ_Psc1B()           SetBit ( RegInt1Msk,
Int1MskPsc1B )

```

```

#define Dis_IRQ_Psc1B()          ClrBit ( RegInt1Msk,
Int1MskPsc1B )

#define En_IRQ__OpAmp()         SetBit ( RegInt1Msk,
Int1MskOpAmp )
#define Dis_IRQ__OpAmp()       ClrBit ( RegInt1Msk,
Int1MskOpAmp )

#define En_IRQ_Tim3()           SetBit ( RegInt1Msk,
Int1MskTim3 )
#define Dis_IRQ_Tim3()         ClrBit ( RegInt1Msk,
Int1MskTim3 )

#define En_IRQ_Tim2()           SetBit ( RegInt1Msk,
Int1MskTim2 )
#define Dis_IRQ_Tim2()         ClrBit ( RegInt1Msk,
Int1MskTim2 )

#define En_IRQ_Port1()          SetBit ( RegInt1Msk,
Int1MskPort_1 )
#define Dis_IRQ_Port()         ClrBit ( RegInt1Msk,
Int1MskPort_1 )

#define En_IRQ_Port2()          SetBit ( RegInt1Msk,
Int1MskPort_2 )
#define Dis_IRQ_Port2()        ClrBit ( RegInt1Msk,
Int1MskPort_2 )

//-----
-
// RegInt2 sources
//-----
-
#define En_IRQ_Tim4()           SetBit ( RegInt2Msk,
Int2MskTim4 )
#define Dis_IRQ_Tim4()         ClrBit ( RegInt2Msk,
Int2MskTim4 )

#define En_IRQ_Port3()          SetBit ( RegInt2Msk,
Int2MskPort_3 )
#define Dis_IRQ_Port3()        ClrBit ( RegInt2Msk,
Int2MskPort_3 )

#define En_IRQ_Port4()          SetBit ( RegInt2Msk,
Int2MskPort_4 )
#define Dis_IRQ_Port4()        ClrBit ( RegInt2Msk,
Int2MskPort_4 )

#define En_IRQ_Port5()          SetBit ( RegInt2Msk,
Int2MskPort_5 )
#define Dis_IRQ_Port5()        ClrBit ( RegInt2Msk,
Int2MskPort_5 )

```

```

#define En_IRQ_Port6()           SetBit ( RegInt2Msk,
Int2MskPort_6 )
#define Dis_IRQ_Port6()         ClrBit ( RegInt2Msk,
Int2MskPort_6 )

#define En_IRQ_Port7()           SetBit ( RegInt2Msk,
Int2MskPort_7 )
#define Dis_IRQ_Port7()         ClrBit ( RegInt2Msk,
Int2MskPort_7 )

#define En_IRQ_SlpCnt()          SetBit ( RegInt2Msk,
Int2MskSlpCnt )
#define Dis_IRQ_SlpCnt()         ClrBit ( RegInt2Msk,
Int2MskSlpCnt )

#define En_IRQ_VLD()             SetBit ( RegInt2Msk,
Int2MskVLD )
#define Dis_IRQ_VLD()           ClrBit ( RegInt2Msk,
Int2MskVLD )

//-----
-
// RegInt0PostMsk sources
//-----
-
#define EnPost_IRQ_PmMiss()      SetBit ( RegInt0PostMsk,
Int0PostMskPMMiss )
#define DisPost_IRQ_PmMiss()     ClrBit ( RegInt0PostMsk,
Int0PostMskPMMiss )

#define EnPost_IRQ_GASP()        SetBit ( RegInt0PostMsk,
Int0PostMskGasp )
#define DisPost_IRQ_GASP()       ClrBit ( RegInt0PostMsk,
Int0PostMskGasp )

#define EnPost_IRQ_DoCPM()       SetBit ( RegInt0PostMsk,
Int0PostMskDoCPM )
#define DisPost_IRQ_DoCPM()      ClrBit ( RegInt0PostMsk,
Int0PostMskDoCPM )

#define EnPost_IRQ_DoCDM()       SetBit ( RegInt0PostMsk,
Int0PostMskDoCDM )
#define DisPost_IRQ_DoCDM()      ClrBit ( RegInt0PostMsk,
Int0PostMskDoCDM )

#define EnPost_IRQ_ADC()         SetBit ( RegInt0PostMsk,
Int0PostMskADC )
#define DisPost_IRQ_ADC()        ClrBit ( RegInt0PostMsk,
Int0PostMskADC )

```

```

#define EnPost_IRQ_Psc11Hz()      SetBit ( RegInt0PostMsk,
Int0PostMskPsc11Hz )
#define DisPost_IRQ_Psc11Hz()    ClrBit ( RegInt0PostMsk,
Int0PostMskPsc11Hz )

#define EnPost_IRQ_Tim1()        SetBit ( RegInt0PostMsk,
Int0PostMskTim1 )
#define DisPost_IRQ_Tim1()      ClrBit ( RegInt0PostMsk,
Int0PostMskTim1 )

#define EnPost_IRQ_Port0()       SetBit ( RegInt0PostMsk,
Int0PostMskPort_0 )
#define DisPost_IRQ_Port0()     ClrBit ( RegInt0PostMsk,
Int0PostMskPort_0 )

//-----
-
// RegInt1 PostMSK sources
//-----
-
#define EnPost_IRQ_SPIStart()    SetBit ( RegInt1PostMsk,
Int1PostMskSPIStart )
#define DisPost_IRQ_SPIStart()  ClrBit ( RegInt1PostMsk,
Int1PostMskSPIStart )

#define EnPost_IRQ_SPIStop()     SetBit ( RegInt1PostMsk,
Int1PostMskSPIStop )
#define DisPost_IRQ_SPIStop()   ClrBit ( RegInt1PostMsk,
Int1PostMskSPIStop )

#define EnPost_IRQ_Psc1B()       SetBit ( RegInt1PostMsk,
Int1PostMskPsc1B )
#define DisPost_IRQ_Psc1B()     ClrBit ( RegInt1PostMsk,
Int1PostMskPsc1B )

#define EnPost_IRQ_OpAmp()       SetBit ( RegInt1PostMsk,
Int1PostMskOpAmp )
#define DisPost_IRQ_OpAmp()     ClrBit ( RegInt1PostMsk,
Int1PostMskOpAmp )

#define EnPost_IRQ_Tim3()        SetBit ( RegInt1PostMsk,
Int1PostMskTim3 )
#define DisPost_IRQ_Tim3()      ClrBit ( RegInt1PostMsk,
Int1PostMskTim3 )

#define EnPost_IRQ_Tim2()        SetBit ( RegInt1PostMsk,
Int1PostMskTim2 )
#define DisPost_IRQ_Tim2()      ClrBit ( RegInt1PostMsk,
Int1PostMskTim2 )

#define EnPost_IRQ_Port1()       SetBit ( RegInt1PostMsk,
Int1PostMskPort_1 )

```

```

#define DisPost_IRQ_Port1()          ClrBit ( RegInt1PostMsk,
Int1PostMskPort_1 )

#define EnPost_IRQ_Port2()          SetBit ( RegInt1PostMsk,
Int1PostMskPort_2 )
#define DisPost_IRQ_Port2()          ClrBit ( RegInt1PostMsk,
Int1PostMskPort_2 )

//-----
-
// RegInt2 PostMSK sources
//-----
-
#define EnPost_IRQ_Tim4()           SetBit ( RegInt2PostMsk,
Int2PostMskTim4 )
#define DisPost_IRQ_Tim4()          ClrBit ( RegInt2PostMsk,
Int2PostMskTim4 )

#define EnPost_IRQ_Port3()          SetBit ( RegInt2PostMsk,
Int2PostMskPort_3 )
#define DisPost_IRQ_Port3()          ClrBit ( RegInt2PostMsk,
Int2PostMskPort_3 )

#define EnPost_IRQ_Port4()          SetBit ( RegInt2PostMsk,
Int2PostMskPort_4 )
#define DisPost_IRQ_Port4()          ClrBit ( RegInt2PostMsk,
Int2PostMskPort_4 )

#define EnPost_IRQ_Port5()          SetBit ( RegInt2PostMsk,
Int2PostMskPort_5 )
#define DisPost_IRQ_Port5()          ClrBit ( RegInt2PostMsk,
Int2PostMskPort_5 )

#define EnPost_IRQ_Port6()          SetBit ( RegInt2PostMsk,
Int2PostMskPort_6 )
#define DisPost_IRQ_Port6()          ClrBit ( RegInt2PostMsk,
Int2PostMskPort_6 )

#define EnPost_IRQ_Port7()          SetBit ( RegInt2PostMsk,
Int2PostMskPort_7 )
#define DisPost_IRQ_Port7()          ClrBit ( RegInt2PostMsk,
Int2PostMskPort_7 )

#define EnPost_IRQ_SlpCnt()          SetBit ( RegInt2PostMsk,
Int2PostMskSlpCnt )
#define DisPost_IRQ_SlpCnt()          ClrBit ( RegInt2PostMsk,
Int2PostMskSlpCnt )

#define EnPost_IRQ_VLD()            SetBit ( RegInt2PostMsk,
Int2PostMskVLD )
#define DisPost_IRQ_VLD()            ClrBit ( RegInt2PostMsk,
Int2PostMskVLD )

```

```

//-----
-
// RegInt0Sts SOFTWARE INTERRUPT ACQUISITION SET
//-----
-
#define SetPending_IRQ_PmMiss()          SetBit ( RegInt0Sts,
Int0StsPmMiss )
#define ClrPending_IRQ_PmMiss()         ClrBit ( RegInt0Sts,
Int0StsPmMiss )

#define SetPending_IRQ_GASP()           SetBit ( RegInt0Sts,
Int0StsGasp )
#define ClrPending_IRQ_GASP()          ClrBit ( RegInt0Sts,
Int0StsGasp )

#define SetPending_IRQ_DoCPM()          SetBit ( RegInt0Sts,
Int0StsDoCPM )
#define ClrPending_IRQ_DoCPM()         ClrBit ( RegInt0Sts,
Int0StsDoCPM )

#define SetPending_IRQ_DoCDM()          SetBit ( RegInt0Sts,
Int0StsDoCDM )
#define ClrPending_IRQ_DoCDM()         ClrBit ( RegInt0Sts,
Int0StsDoCDM )

#define SetPending_IRQ_ADC()            SetBit ( RegInt0Sts,
Int0StsADC )
#define ClrPending_IRQ_ADC()           ClrBit ( RegInt0Sts,
Int0StsADC )

#define SetPending_IRQ_Psc11Hz()        SetBit ( RegInt0Sts,
Int0StsPsc11Hz )
#define ClrPending_IRQ_Psc11Hz()       ClrBit ( RegInt0Sts,
Int0StsPsc11Hz )

#define SetPending_IRQ_Tim1()           SetBit ( RegInt0Sts,
Int0StsTim1 )
#define ClrPending_IRQ_Tim1()          ClrBit ( RegInt0Sts,
Int0StsTim1 )

#define SetPending_IRQ_Port0()          SetBit ( RegInt0Sts,
Int0StsPort_0 )
#define ClrPending_IRQ_Port0()         ClrBit ( RegInt0Sts,
Int0StsPort_0 )

//-----
-
// RegInt1Sts SOFTWARE INTERRUPT ACQUISITION SET
//-----
-

```

```

#define SetPending_IRQ_SPIStart()      SetBit ( RegInt1Sts,
Int1StsSPIStart )
#define ClrPending_IRQ_SPIStart()      ClrBit ( RegInt1Sts,
Int1StsSPIStart )

#define SetPending_IRQ_SPIStop()       SetBit ( RegInt1Sts,
Int1StsSPIStop )
#define ClrPending_IRQ_SPIStop()       ClrBit ( RegInt1Sts,
Int1StsSPIStop )

#define SetPending_IRQ_Psc1B()         SetBit ( RegInt1Sts,
Int1StsPsc1B )
#define ClrPending_IRQ_Psc1B()         ClrBit ( RegInt1Sts,
Int1StsPsc1B )

#define SetPending_IRQ_OpAmp()         SetBit ( RegInt1Sts,
Int1StsOpAmp )
#define ClrPending_IRQ_OpAmp()         ClrBit ( RegInt1Sts,
Int1StsOpAmp )

#define SetPending_IRQ_Tim3()          SetBit ( RegInt1Sts,
Int1StsTim3 )
#define ClrPending_IRQ_Tim3()          ClrBit ( RegInt1Sts,
Int1StsTim3 )

#define SetPending_IRQ_Tim2()          SetBit ( RegInt1Sts,
Int1StsTim2 )
#define ClrPending_IRQ_Tim2()          ClrBit ( RegInt1Sts,
Int1StsTim2 )

#define SetPending_IRQ_Port1()         SetBit ( RegInt1Sts,
Int1StsPort_1 )
#define ClrPending_IRQ_Port1()         ClrBit ( RegInt1Sts,
Int1StsPort_1 )

#define SetPending_IRQ_Port2()         SetBit ( RegInt1Sts,
Int1StsPort_2 )
#define ClrPending_IRQ_Port2()         ClrBit ( RegInt1Sts,
Int1StsPort_2 )

//-----
-
// RegInt2Sts SOFTWARE INTERRUPT ACQUISITION SET
//-----
-

#define SetPending_IRQ_Tim4()          SetBit ( RegInt2Sts,
Int2StsTim4 )
#define ClrPending_IRQ_Tim4()          ClrBit ( RegInt2Sts,
Int2StsTim4 )

```

```

#define SetPending_IRQ_Port3()          SetBit ( RegInt2Sts,
Int2StsPort_3 )
#define ClrPending_IRQ_Port3()          ClrBit ( RegInt2Sts,
Int2StsPort_3 )

#define SetPending_IRQ_Port4()          SetBit ( RegInt2Sts,
Int2StsPort_4 )
#define ClrPending_IRQ_Port4()          ClrBit ( RegInt2Sts,
Int2StsPort_4 )

#define SetPending_IRQ_Port5()          SetBit ( RegInt2Sts,
Int2StsPort_5 )
#define ClrPending_IRQ_Port5()          ClrBit ( RegInt2Sts,
Int2StsPort_5 )

#define SetPending_IRQ_Port6()          SetBit ( RegInt2Sts,
Int2StsPort_6 )
#define ClrPending_IRQ_Port6()          ClrBit ( RegInt2Sts,
Int2StsPort_6 )

#define SetPending_IRQ_Port7()          SetBit ( RegInt2Sts,
Int2StsPort_7 )
#define ClrPending_IRQ_Port7()          ClrBit ( RegInt2Sts,
Int2StsPort_7 )

#define SetPending_IRQ_SlpCnt()         SetBit ( RegInt2Sts,
Int2StsSlpCnt )
#define ClrPending_IRQ_SlpCnt()         ClrBit ( RegInt2Msk,
Int2StsSlpCnt )

#define SetPending_IRQ_VLD()            SetBit ( RegInt2Sts,
Int2StsVLD )
#define ClrPending_IRQ_VLD()            ClrBit ( RegInt2Sts,
Int2StsVLD )

//-----
-
//EVENT MSK CONFIG

#define En_Evt0_GASP()                  SetBit ( RegEvtCfg,
Evt0MskGasp )
#define Dis_Evt0_GASP()                 ClrBit ( RegEvtCfg,
Evt0MskGasp )

#define EnPost_Evt0_GASP()              SetBit ( RegEvtCfg,
Evt0PostMskGasp )
#define DisPost_Evt0_GASP()             ClrBit ( RegEvtCfg,
Evt0PostMskGasp )

#define En_Evt1_ADC()                   SetBit ( RegEvtCfg,
Evt1MskADC )

```

```

#define Dis_Evt1_ADC()                ClrBit ( RegEvtCfg,
Evt1MskADC )

#define EnPost_Evt1_ADC()             SetBit ( RegEvtCfg,
Evt1PostMskADC )
#define DisPost_Evt1_ADC()           ClrBit ( RegEvtCfg,
Evt1PostMskADC )

#define En_Evt1_SPI()                 SetBit ( RegEvtCfg,
Evt1MskSPI )
#define Dis_Evt1_SPI()               ClrBit ( RegEvtCfg,
Evt1MskSPI )

#define EnPost_Evt1_SPI()            SetBit ( RegEvtCfg,
Evt1PostMskSPI )
#define DisPost_Evt1_SPI()          ClrBit ( RegEvtCfg,
Evt1PostMskSPI )

#define En_Evt1_SC()                 SetBit ( RegEvtCfg,
Evt1MskSC )
#define Dis_Evt1_SC()               ClrBit ( RegEvtCfg,
Evt1MskSC )

#define EnPost_Evt1_SC()             SetBit ( RegEvtCfg,
Evt1PostMskSC )
#define DisPost_Evt1_SC()           ClrBit ( RegEvtCfg,
Evt1PostMskSC )

//-----
-
//Event Status Set and Clear
//-----
-

#define SetPending_Evt0_GASP()        SetBit ( RegEvtSts,
Evt0StsGasp )
#define ClrPending_Evt0_GASP()       ClrBit ( RegEvtSts,
Evt0StsGasp )

#define SetPending_Evt1_ADC()         SetBit ( RegEvtSts,
Evt1StsADC )
#define ClrPending_Evt1_ADC()        ClrBit ( RegEvtSts,
Evt1StsADC )

#define SetPending_Evt1_SPI()         SetBit ( RegEvtSts,
Evt1StsSPI )
#define ClrPending_Evt1_SPI()        ClrBit ( RegEvtSts,
Evt1StsSPI )

#define SetPending_Evt1_SC()          SetBit ( RegEvtSts,
Evt1StsSlpCnt )

```



```

*****
*/

volatile unsigned int UserSelect=0;

int main()
{
//Connect PB[2] TO PA[3]
//CONNECT PC[4] TO PA[4]
//CONNECT PC[0] TO PA[5]

    fSysInitilize();
//Initialization: Make D=0,Dbar=1, therefore main Battery
working

//    SetBit(RegPCDOut,Dswitch);    //D=0
    ClrBit(RegPCDOut,Dswitch);
//    SetBit(RegPCDOut,Dbarswitch); //Dbar=1
    SetBit(RegPBDOut,TurnOFFSys); //Make System ON
    SetBit(RegPCDOut,FreqOut); //make FreqOut as 1

//This is for the code to set the FreqOut

    Tim34_Enable();
    Tim34_SelStart_Clk(TimSelStart_SW,Tim3SelClk_PR1CK13);
//8kHz/4=2kHz
    Timer34_AR_En();
    Tim34_SetFullValue(500); //2kHz/1000=2HZ
    Tim3_Int_FullValue();
    En_IRQ_Tim3();
    Timer34_SWStart();

while(1)
{
    switch (UserSelect)
    {
        case 1: //if select USB, turn ON A, OFF B && C
            ClrBit(RegPBDOut,Bswitch);
            ClrBit(RegPBDOut,Cswitch);
            SetBit(RegPADOut,Aswitch);
            break;

        case 2:
            ClrBit(RegPADOut,Aswitch);
            ClrBit(RegPBDOut,Cswitch);
            SetBit(RegPBDOut,Bswitch);
            break;

        case 3:

```

```

        ClrBit(RegPADOut,Aswitch);
        ClrBit(RegPBDOut,Bswitch);
        SetBit(RegPBDOut,Cswitch);
        break;

    case 0:          //user made no selection

        fConfigVLD_SenseA_USB();
        if(is_level_below_VLD==0) //turn on A if it has
voltage
        {
            ClrBit(RegPBDOut,Bswitch);
            ClrBit(RegPBDOut,Cswitch);
            SetBit(RegPADOut,Aswitch);
        }else
        {
            fConfigVLD_SenseB_Light();
            if(is_level_below_VLD==0)
            {
                ClrBit(RegPADOut,Aswitch);
                ClrBit(RegPBDOut,Cswitch);
                SetBit(RegPBDOut,Bswitch); //turn on B
            }else
            {
                fConfigVLD_SenseC_RF();
                if(is_level_below_VLD==0)
                {
                    ClrBit(RegPBDOut,Bswitch);
                    ClrBit(RegPADOut,Aswitch);
                    SetBit(RegPBDOut,Cswitch); //turn on C
                }else
                {
                    fConfigVLD_SupplyNode_VS1();
                    if(is_level_below_VLD) //TurnOFF system
                        ClrBit(RegPBDOut,TurnOFFSys);
                }
            }
        }

        break;

    }
    fCheckVLDLevel();
}

return 0;
}

```

sc wakeup.c

```
*****
*/
#include "header.h"
#include "8kmeas.h"
/*****
**/
extern UINT16 clock_period;
/*****
**
    fSetTimeSleepCounter_ms:
        set sleep counter time-out in milli-seconds
    parameter :
        Parameter "time" is integer value in the range [1,
999]
return:
        return 1 if parameter is beyond range, otherwise echo
"time"
*****
*/

UINT16 fSetTimeSleepCounter_ms(UINT16 time)
{
    // SC_timeout(((MILLISECOND/clock_period)*time));
    // Above format calls udivmodhi4, which puts garbage value for
    RegSCLdVal2
    // Format below is workaround from rest functions where it
    would call
    // divmodsi4 and everything is clean
    if((time>999)|| (time<1))return(1);
    SC_timeout(((MICRO_SECONDS/clock_period)*time)/MILLISECOND);
    return(time);
}

/*****
**
    fSetTimeSleepCounter_s:
        set sleep counter time-out in seconds
    parameter :
        Parameter "time" is integer value in the range [1, 59]
return:
        return 1 if parameter is beyond range, otherwise echo
"time"
*****
/
UINT16 fSetTimeSleepCounter_s (UINT16 time)
{
```

```

        if((time>59)|| (time<1)) return(1);
        SC_timeout((MICRO_SECONDS/clock_period)*time));
        return(time);
    }
/*****
**
    fSetTimeSleepCounter_min:
        set sleep counter time-out in minutes
    parameter :
        Parameter "time" is integer value in the range [1, 30]
    return:
        return 1 if parameter is beyond range, otherwise echo
    "time"
*****/
UINT16 fSetTimeSleepCounter_min (UINT16 time)
{
    if((time>30)|| (time<1)) return(1);

    SC_timeout((MICRO_SECONDS/clock_period)*(time*SECONDS_IN_MIN)
    ));
    return(time);
}

/*****
**
    validate_sleep_time:
        set sleep mode &
        GLOW LED conncted to PORT-PC6 on Reva Board on
    wake-up
*****/
void validate_sleep_time(void)
{

    En_IRQ_SlpCnt();
    SC_Start();
    SetSleep_Mode();
    ClrBit(RegPCDOut,0x40); // GLOW the LED connected to PC6
    SC_Stop();

}
/*****/
**/

```

sysinitialize.c

```

#include "header.h"
#include "Lib6819\periph.h"

```

```

#include "Lib6819\ports.h"
#include "Lib6819\Types.h"

/*****
*
fSysInitilize:
    Initilises CPU Clock,PORT

*****/
*/
void fSysInitilize()
{
    SelCkLo_Ck_8KHZ();
    Sel_CPU_Clock(Ck_Lo_Divided_1);
    Sel_Prescaler1_Clock(SelCkPr1_Ck_Lo_Divided_1);

//Set Ouput Port----->>>> Switch Control
PA_SetOUT (PAOE_0);      //A
PB_SetOUT (PBOE_6);      //B
PB_SetOUT (PBOE_4);      //C
PC_SetOUT (PCOE_2);      //D
PC_SetOUT (PCOE_3);      //FreqOut
PB_SetOUT (PBOE_7);      //E
PB_SetOUT (PBOE_5);      //TurnOFFSys
// PA_SetOUT (PAOE_6);    //

//Set Input Port----->>>> User Input Select
PA_SetIN(BIT3);         // SW1  PB[2]  PA[3]
PB_SetIN(BIT2);

PA_SetIN(BIT4);         // SW2  PC[4]  PA[4]
PC_SetIN(BIT4);

PA_SetIN(BIT5);         // SW4  PC[0]  PA[5]
PC_SetIN(BIT0);

En_IRQ_Port3();         //Enable PA3(PORT3) interrupt
En_IRQ_Port4();
En_IRQ_Port5();

IntPortSrc_PORTA(BIT3);
IntPortSrc_PORTA(BIT4);
IntPortSrc_PORTA(BIT5);

PA_INT_FALLING_EDGE(BIT3);      //falling edge
PA_INT_FALLING_EDGE(BIT4);
PA_INT_FALLING_EDGE(BIT5);

//disable debouncer

```

```

/*
PA4_DEBOUNCER(Port_4_DebSel_NO_CLK);
PA5_DEBOUNCER(Port_5_DebSel_NO_CLK);

PA6_DEBOUNCER(Port_6_DebSel_NO_CLK);
PA7_DEBOUNCER(Port_7_DebSel_NO_CLK);
*/
// WDT_Disable();
// RegResFlg = 0x00;

//fTim34_config();

}

// void fTim34_config (void )
// {
// Tim34_Enable();
// Tim34_SelStart_Clk(TimSelStart_SW,Tim3SelClk_PR2CK4);
// Timer34_AR_En();
// Tim3_Int_FullValue();
// Tim34_SetFullValue(625);
// En_IRQ_Tim3();
// }

```

sysinitialize.h

```

//function prototype
void fSysInitalize(void)

```

Chapter 8: Bibliography

- [1] T.J.Kazmierski, S.Beeby, *Energy Harvesting Systems, Principles, Modeling and Applications*, New York: Springer, 2011.
- [2] S.Priya, D.J.Inman, *Energy Harvesting Technologies*, New York: Springer, 2009.
- [3] M.T.Penella-Lopez, M.Gasulla-Forner, *Powering Autonomous Sensors: An integral Approach with Focus on Solar and RF Energy Harvesting*, New York: Springer, 2011.
- [4] D.I.Andres, *Energy Harvesting Materials*, Danvers: World Scientific Publishing Co. Pte. Ltd, 2005.
- [5] F. Lasnier, T.G. Ang, *Photovoltaic Engineering Handbook*, Bristol: Adam Hilger, 1990.
- [6] U.S. Department of Energy, "PV systems, Energy Efficiency and Renewable Energy, Solar Energy Technologies," [Online]. Available: <http://www1.eere.energy.gov/solar>. [Accessed 27 June 2013].
- [7] U.S. Department of Energy, Energy Efficiency and Renewable Energy, Solar Energy Technologies Program, "PV devices," [Online]. Available: <http://www1.eere.energy.gov/solar>. [Accessed 27 June 2013].
- [8] M. van Cleef, P. Lippens, and J.Call, "Superior energy yields of UNI-SOLAR_ triple junction thin film silicon solar cells under real outdoor conditions in Western Europe," in *17th European Photovoltaic Solar Energy Conference and Exhibition*, Munich, 2001.
- [9] M.Van Cleef, P.Lippens, and J. Call, "Superior energy yields of UNI-SOLAR triple junction thin film silicon solar cells compared to crystalline silicon solar cells under real outdoor conditions in Western Europe," in *17th European Photovoltaic Solar Energy Conference and Exhibition*, Munich, 2001.
- [10] U.S. Department of Energy, Energy Efficiency and Renewable Energy, Solar Energy Technologies Program, "Solar cell materials," [Online]. Available: <http://www1.eere.energy.gov/solar>. [Accessed 27 June 2013].
- [11] A. Khaligh, O.C.Onar, *Energy Harvesting: Solar, Wind, and Ocean Energy Conversion Systems*, CRC Press, 2009.
- [12] J.P. Thomas, M.A. Qidwai, J.C. Kellogg, "Energy scavenging for small-scale unmanned systems," *Journal of Power Sources*, vol. 159, no. 2, p. 1494–1509, 2006.
- [13] L. Hu, "ENMA 698N lecture in University of Maryland College Park," College Park, MD, 2012.
- [14] J.B.Burch, M.Clark, M.G.Yost, C.T.T.Fitzpatrick, A.M. Bachand, J.Ramaprasad, J.S.Reif, "Radio Frequency Nonionizing Radiation in a Community Exposed to Radio and Television Broadcasting," *Environ Health*

- Perspect*, vol. 114, no. 2, p. 248–253, 2006.
- [15] J.A. Hagerty, F.B. Helmbrecht, W.H. McCalpin, R. Zane, Z. B. Popovic, "Recycling ambient microwave energy with broad-band rectenna arrays," *IEEE Trans. on Microwave Theory and Techniques*, vol. 52, no. 3, pp. 1014-1024, 2004.
 - [16] J.P. Curty, N. Joehl, C. Dehollain, M.J. Declercq, "Remotely powered addressable UHF RFID integrated system," *IEEE Journal of Solid-State Circuits*, vol. 40, pp. 2149-2202, 2005.
 - [17] S. Young-Ho, C. Kai, "A high-efficiency dual-frequency rectenna for 2.45- and 5.8-GHz wireless power transmission," *IEEE Trans. Microwave Theory and Techniques*, vol. 50, pp. 1784-1789, 2002.
 - [18] E.M. Yeatman, G.K. Rao, A.S. Holmes, T.C. Green, "Energy Harvesting From Human and Machine Motion for Wireless Electronic Devices," *Proceedings of the IEEE*, vol. 96, no. 9, pp. 1457-1486, 2008.
 - [19] N.S. Shenck, "Energy scavenging with shoe-mounted piezoelectrics," *Micro, IEEE*, vol. 21, no. 3, pp. 30-40, 2001.
 - [20] B.H. Stark, P.D. Mitcheson, M. Peng, T.C. Green, E.M. Yeatman, A.S. Holmes, "Converter circuit design, semiconductor device selection and analysis of parasitics for micropower electrostatic generators," *IEEE Trans. Power Electronics*, vol. 21, pp. 27-37, 2006.
 - [21] E.O. Torres, G.A. Rincon-Mora, "Electrostatic energy harvester and Li-ion charger circuit for micro-scale applications," in *Proceedings of 49th IEEE International Midwest Symposium on Circuits and Systems, MWSCAS (2006)*, Puerto Rico, 2006.
 - [22] S. Xu, K.D.T. Ngo, T. Nishida, G.B. Chung, A. Sharma, "Low frequency pulsed resonant converter for energy harvesting," *IEEE Trans. Power Electronics*, vol. 22, pp. 63-68, 2007.
 - [23] M. H. Schneider, J. W. Evans, P. K. Wright, D Ziegler, "Designing a thermoelectrically powered wireless sensor network for monitoring aluminium smelters," *Journal of Process Mechanical Engineering*, vol. 220, no. 3, pp. 181-190, 2006.
 - [24] D. Guyomar, G. Sebald, E. Lefevre, A. Khodayari, "Toward Heat Energy Harvesting using Pyroelectric Material," *Journal of Intelligent Material Systems and Structures*, vol. 20, no. 3, p. 265, 2009.
 - [25] G. Sebald, S. Pruvost, D. Guyomar, "Energy harvesting based on Ericsson pyroelectric cycles," *Smart Materials and Structures*, vol. 17, no. 1, 2008.
 - [26] S. Kerzenmachera, J. Ducree, R. Zengerle, F. Von Stetten, "Energy harvesting by implantable abiotically catalyzed glucose fuel cells," *Journal of Power Sources*, vol. 182, no. 1, pp. 1-17, 2008.
 - [27] N.G. Dhere, R.G. Dhere, "Thin-film photovoltaics," *Journal of Vacuum Science & Technology A*, vol. 23, no. 4, pp. 1208-1214, 2005.
 - [28] P. Rako, "EDN Network," EDN Network, 1 Dec 2006. [Online]. Available: <http://www.edn.com/design/power-management/4317437/Creating-the-power->

- subsystem-in-modern-design. [Accessed 21 Sep 2012].
- [29] R.W. Erickson, D. Maksimovic, *Fundamentals of Power Electronics*, Norwell: Kluwer Academic, 2001.
- [30] H.A.Kiehne, *Battery Technology Handbook*, Second Edition, New York: Marcel Dekker, Inc., 2003.
- [31] D. Linden, T.B. Reddy, *Handbook of Batteries*, New York: McGraw-Hill, 2001.
- [32] R.M. Dell, D.A.J. Rand, *Understanding Batteries*, London: The Royal Society of Chemistry, 2001.
- [33] I.Buchmann, *Batteries in a Portable World*, 2nd edn., Richmond: Cadex Electronics Inc., 2001.
- [34] J.B.Bates, N.J. Dudney, B Neudecker, A.Ueda, C.D. Evans, "Thin-film lithium and lithium-ion," *Solid State Ionics*, vol. 135, no. 1-4, p. 33–45, 2000.
- [35] D.Steigart, C.C.Ho, J. Salminen, J.W.Evans, P.K.Wright, "Dispenser printing of solid polymerionic liquid electrolytes for lithium ion cells," in *Polymers and Adhesives in Microelectronics and*, Tokyo, Japan, 2007.
- [36] M. T. Inc, "Design considerations for ultracapacitors," Maxwell Technologies Inc, [Online]. Available: http://www.maxwell.com/pdf/uc/white-papers/200904_WhitePaper_DesignInGuide.pdf. [Accessed 24 Sep 2012].
- [37] G.Prophet, "EDN, Electronic Design Newsletter," 9 Jan 2003. [Online]. Available: <http://www.edn.com/file/18347-268379.pdf>. [Accessed 24 09 2012].
- [38] T. Umeda, H. Yoshida, S. Sekine, Y. Fujita, T. Suzuki, S. Otaka, "A 950-MHz rectifier circuit for sensor network tags with 10-m distance," *IEEE Journal of Solid-State Circuits*, vol. 41, no. 1, pp. 35-41, 2006.
- [39] F. Kocer, M.P. Flynn, "An RF-powered, wireless CMOS temperature sensor," *IEEE Sensors Journal*, vol. 6, no. 3, pp. 557-564, 2006.
- [40] T. Paing, J. Morroni, A. Dolgov, J. Shin, J. Brannan, R. Zane, Z. Popovic, "Wirelessly-powered wireless sensor platform," in *Proceedings of European Microwave Conference*, Boulder, 2007.
- [41] P. Singh, W. Xiquan, R. Lafollette, D. Reisner, "RF-recharged microbattery for powering miniature sensors," in *Proceedings of IEEE Sensors*, Vienna, Austria, 2004.
- [42] Powercast, "P2110 Datasheet," April 2010. [Online]. Available: <http://www.powercastco.com/PDF/P2110-datasheet.pdf>. [Accessed 22 Oct 2012].
- [43] H. Jabbar, Y. S. Song, T. T. Jeong, "RF Energy Harvesting System and Circuits for Charging of Mobile Devices," *IEEE Transactions on Consumer Electronics*, vol. 56, no. 1, pp. 247 - 253, 2010.
- [44] B. Li, "Ultra Low Power FSK Receiver and RF Energy Harvester," PhD Dissertation, University of Maryland, College Park, MD, 2011.
- [45] W. Zhao, K. Choi, S Bauman, Z. Dilli, T. Salter and M. Peckerar, "A Radio-Frequency Energy Harvesting Scheme for Use in Low-Power Ad Hoc Distributed Networks," *IEEE Transactions on Circuits and Systems II: Express*

- Briefs*, vol. 59, no. 9, pp. 573-577, 2012.
- [46] M Peckerar, W Zhao, Z Dilli, M Dornajafi, D Lowy, S Potbhare, "Supercapacitor/Battery Hybrids for Energy Harvesting Applications," *ECSTransactions*, vol. 41, no. 8, pp. 31-35, 2011.
- [47] T. Salter, K. Choi, M. Peckerar, G. Metze and N. Goldsman, "RF energy scavenging system utilizing switched capacitor DC-DC converter," *Electronics Letters*, vol. 45, no. 7, pp. 374-376, 2009.
- [48] M. Peckerar, M. Dornajafi, Z. Dilli, N. Goldsman, Y. Ngu, B. Boerger, N. V. Wyck, J. Gravelin, B. Grenon, R. B. Proctor, and D. A. Lowy, "Fabrication of flexible ultracapacitor/galvanic cell hybrids using advanced nanoparticle coating technology," *J. Vac. Sci. Technol. B*, vol. 29, no. 1, pp. 011008 - 011008-6, 2011.
- [49] M. Peckerar, Z. Dilli, M. Dornajafi, N. Goldsman, Y. Ngu, R.B. Proctor, B.J. Krupsaw and D. A. Lowy, "A novel high energy density flexible galvanic cell," *Energy Environ. Sci.*, vol. 4, pp. 1807-1812, 2011.
- [50] D.B.Miron, *Small Antenna Design*, Burlington, MA 01803, USA: Elsevier, 2006.
- [51] T.A.Milligan, *Modern Antenna Design*, Second Edition, Hoboken, New Jersey: John Wiley & Sons, Inc., 2005.
- [52] J.P. Curty, M. Declercq, C. Dehollain, N. Joehl, *Design and Optimization of Passive UHF RFID Systems*, New York: Springer Science+Business Media, 2007.
- [53] V.H.Rumsey, "Frequency Independent Antennas," in *I.R.E. National Convention Record, Part I*, New York, 1957.
- [54] Skyworks Solutions Inc., "Surface Mount Mixer and Detector Schottky Diodes Datasheet," 21 April 2012. [Online]. Available: <http://www.skyworksinc.com/uploads/documents/200041V.pdf>. [Accessed 27 09 2012].
- [55] R. J. Baker, H. W. Li, D. E. Boyce, *CMOS Circuit Design, Layout and Simulation*, New York: IEEE Press, 1998.
- [56] S.R.Forrest, "The path to ubiquitous and low-cost organic electronic appliances on plastic," *Nature*, vol. 428, no. 6986, pp. 911-918, 2004.
- [57] S.Sarpeshkar and R.Mandal, "Low-Power CMOS Rectifier Design for RFID Applications," *IEEE Trans. Circuits Syst. I*, vol. 54, no. 6, pp. 1177-1188, 2007.
- [58] C.F.Owens, B.B.Holmes, *Batteries for Implantable Biomedical Applications*. Wiley Encyclopedia of Biomedical Engineering, New York: J. Wiley & Sons, 2006.
- [59] Y. Lin, N. Zhao, W. Nie and X. Ji, "Synthesis of ruthenium dioxide nanoparticles by a two-phase route and their electrochemical properties," *J. Phys. Chem*, vol. 112, no. 42, pp. 16219-16224, 2008.
- [60] Y. Zhao, L. Liu, J. Xu, J. Yang, M. Yan and Z. Jiang, "High-performance supercapacitors of hydrous ruthenium oxide/mesoporous carbon composites," *J. Solid State Electrochem*, vol. 11, no. 2, pp. 283-290, 2007.

- [61] B. E. Conway, *Electrochemical Supercapacitors. Scientific Fundamentals and Technological Applications*, New York: Kluwer Academic/Plenum, 1999.
- [62] "SOLAR MINI-PANELS AND MOTORS," *Solar Made*, 11 May 2011. [Online]. Available: <http://www.solarmade.com/SolarMini-Panels%26Motors.htm>. [Accessed 3 Oct 2012].
- [63] "Universal Serial Bus," *Wikipedia*, 3 Oct 2012. [Online]. Available: <http://en.wikipedia.org/wiki/USB>. [Accessed 3 Oct 2012].
- [64] M.J. Perenson, "SuperSpeed USB 3.0: More Details Emerge," *PCWorld*, 9 Jan 2010. [Online]. Available: http://www.pcworld.com/article/156494/superspeed_usb.html. [Accessed 3 Oct 2012].
- [65] Texas Instruments, "Peak Current Limited Step Down Converter for USB Applications," Sep 2008. [Online]. Available: <http://www.ti.com/lit/ds/symlink/tps62250.pdf>. [Accessed 3 Oct 2012].
- [66] M. Park, K. Choi, M. Peckerar, "ULTRA-LOW POWER SERIES PASS ELEMENT VOLTAGE REGULATOR FOR RF-DC ENERGY HARVESTING," in *ISDRS Proceedings*, College Park, MD, 2009.
- [67] Maxim Integrated, "MAX1920 datasheet," 2005. [Online]. Available: <http://datasheets.maximintegrated.com/en/ds/MAX1920-MAX1921.pdf>. [Accessed 6 June 2013].
- [68] Linear Technology Corporation, "http://cds.linear.com/docs/en/datasheet/112935ff.pdf," [Online]. Available: <http://cds.linear.com/docs/en/datasheet/112935ff.pdf>. [Accessed 6 June 2013].
- [69] Linear Technology Corporation, "LTC3564 Datasheet," 2008. [Online]. Available: <http://cds.linear.com/docs/Datasheet/3564f.pdf>. [Accessed 3 Oct 2012].
- [70] EMMicroelectronic, "EM6819 datasheet," 15 April 2010. [Online]. Available: <http://www.emmicroelectronic.com/products.asp?IdProduct=272#Datasheet>. [Accessed 4 Oct 2012].
- [71] Vishay, "Si1035X Datasheet," 12 March 2012. [Online]. Available: <http://www.vishay.com/docs/71426/71426.pdf>. [Accessed 5 Oct 2012].
- [72] Raisonance, "Raisonance official website," *Raisonance*, 4 Oct 2012. [Online]. Available: <http://www.raisonance.com/>. [Accessed 4 Oct 2012].
- [73] EMMicroelectronic, "EM6819 Toolkit," 8 Oct 2008. [Online]. Available: <http://www.emmicroelectronic.com/products.asp?IdProduct=272#15>. [Accessed 4 Oct 2012].
- [74] Raisonance, "Raisonance tools for C816 family," 15 Jan 2009. [Online]. Available: <http://www.raisonance.com/>. [Accessed 11 June 2013].
- [75] CTS Electrocomponents, "series 219 datasheet," 30 Dec 2008. [Online]. Available: <http://www.ctscorp.com/components/Datasheets/219.pdf>. [Accessed 12 Oct 2013].
- [76] TriSquare Electronics Corporation, "Model TSX300 Owner's Manual," 2009. [Online]. Available:

- <http://www.buytwowayradios.com/Products/trisquare/manuals/TSX300-manual.pdf>. [Accessed 6 Oct 2012].
- [77] C.A.Balanis, *Antenna Theory Analysis and Design*, 3rd Edition, Hoboken, New Jersey: A JOHN WILEY & SONS, INC., 2005.
 - [78] C.G.Someda, *Electromagnetic waves*, Second Edition, Boca Raton, FL: Taylor & Francis Group, LLC, 2006.
 - [79] H.C.Rhim, O.Buyukozturk, "Electromagnetic Properties of Concrete at Microwave Frequency Range," *Materials Journal*, vol. 95, no. 3, pp. 262-271, 1998.
 - [80] C.L.Holloway, P.L.Perini, R.R.DeLyser and K.C.Allen, "Analysis of Composite Walls and Their Effects on Short-Path Propagation Modeling," *IEEE TRANSACTIONS ON VEHICULAR TECHNOLOGY*, vol. 46, no. 3, pp. 730-738, 1997.
 - [81] Bo Li, Xi Shao, Negin Shahshahan, Neil Goldsman, Thomas Salter and George M. Metze, "Antenna Coupled Dual Band Energy Harvester Design," in *Proceedings of International Semiconductor Device Research Symposium (ISDRS)*, College Park, MD, 2011.
 - [82] X. Shao, B. Li, N. Shahshahan, N. Goldsman, T. Salter and G. M. Metze, "A Planar Dual-Band Antenna Design for RF Energy Harvesting Applications," in *Proceedings of International Semiconductor Device Research Symposium (ISDRS)*, College Park, MD, 2011.
 - [83] N. Shahshahan, "Resonant Circuit Topology for Radio Frequency Energy Harvesting," UMD Theses and Dissertations, College Park, MD, 2012.
 - [84] W. Greatbatch, "Medical Cardiac Pacemaker". USA Patent 3,057,356, 9 Oct 1962.
 - [85] W.Zhao, K.Choi, S.Bauman, T.Salter, D.A.Lowy, M.Peckerar, M.Kalantari Khandani, "An energy harvesting system surveyed for a variety of unattended electronic applications," *Solid-State Electronics*, 2012.
 - [86] M. Mahowald, R. Douglas, "A silicon neuron," *Nature*, vol. 354, pp. 515-518, 1991.
 - [87] M.T.Hagan, H.B.Demuth, M.H.Beale, *Neural Network Design*, Boston: Pws Pub, 1996.
 - [88] E.R.Kandel, J.H.Schwartz, T.M.Jessell, *Principles of Neural Science*, 4th ed, New York: McGraw-Hill, 2000.
 - [89] J.H.B.Wijekoon, "Integrated circuit implementation of a cortical neuron," in *IEEE International Symposium on Circuits and Systems (ISCAS)*, Seattle, WA, USA, 2008.
 - [90] Wikipedia, "Neuron," Wikipedia, 8 Oct 2012. [Online]. Available: <http://en.wikipedia.org/wiki/Neuron>. [Accessed 9 Oct 2012].
 - [91] K.Matsuoka, "Sustained oscillations generated by mutually inhibiting neurons with adaptation," *Biological Cybernetics*, vol. 52, no. 6, pp. 367-376, 1985.
 - [92] W.Zhao, M.Peckerar, "A novel tunable neural oscillator for biological rhythmic behaviors," in *2012 IEEE 55th International Midwest Symposium on Circuits*

- and Systems (MWSCAS), Boise, Idaho, 2012.
- [93] S.A.Richmond, J.J.Collins and, "Hard-wired central pattern generators for quadrupedal locomotion," *Biological Cybernetics*, vol. 71, no. 5, pp. 375-385, 1994.
- [94] P.Strumillo, M.Strzelecki, "Application of Coupled Neural Oscillators for Image Texture Segmentation and Biological Rhythms Modeling," *Int.J.Appl.Math*, vol. 16, no. 4, pp. 513-523, 2006.
- [95] A. L.Huxley, A. F.Hodgkin, "Currents carried by sodium and potassium ions through the membrane of the giant axon of Loligo," *J Physiol*, vol. 116, no. 4, pp. 449-472, 1952.
- [96] A.Cassidy, "Dynamical digital silicon neurons," in *Biomedical Circuits and Systems Conference, 2008. BioCAS 2008. IEEE*, Baltimore, MD, 2008.
- [97] E.M.Izhikevich, "Simple model of spiking neurons," *IEEE Trans. Neural Netw*, vol. 14, no. 6, pp. 1569-1572, 2003.
- [98] A.Mortara, "A Pulsed Communication/Computation Framework for Analog VLSI Perceptive Systems," *The Kluwer International Series in Engineering and Computer Science*, vol. 447, no. 3, pp. 201-215, 1998.
- [99] J. H.B. Wijekoon, P. Dudek, "Compact silicon neuron circuit with spiking and bursting behavior," *Neural Networks*, vol. 21, pp. 524-534, 2008.
- [100] T.Horiuchi, R. Z. Shi, "A summing, exponentially-decaying CMOS synapse for spiking neural systems," *Adv. Neural Info. Proc. Syst.*, vol. 16, 2004.
- [101] Rensensys, "Rensensys Products," Rensensys, 2011. [Online]. Available: <http://www.rensensys.com/product1.html>. [Accessed 9 Oct 2012].
- [102] J.F.Randall, J.Jacot, "Is AM1.5 applicable in practice? Modeling eight photovoltaic materials with respect to light intensity and two spectra," *Renewable Energy*, vol. 28, no. 12, pp. 1851-1864, 2003.
- [103] A. Hande, T. Polk, W. Walker, D. Bhatia, "solar energy harvesting for sensor network router nodes," *Microprocessors & Microsystems*, vol. 31, no. 6, pp. 420-432, 2007.
- [104] D. Shir, J. Yoon, D. Chanda, J.-H. Ryu, J. A. Rogers, "Performance of Ultrathin Silicon Solar Microcells with Nanostructures of Relief Formed by Soft Imprint Lithography for Broad Band Absorption Enhancement," *Nano Letters*, vol. 10, no. 8, pp. 3041-3046, 2010.
- [105] D.Weatherington, "Unmanned Aerial Vehicles roadmap: 2002 – 2027," Office of the secretary of Defense, Washington, DC, 2002.
- [106] National Research Council, *Uninhabited Air Vehicles: Enabling Science for Military Systems*, Washington, DC: National Academy Press, 2000.
- [107] H.B. Torabi, M. Sadi, A.Y. Varjani, "Solar Power System for Experimental Unmanned Aerial Vehicle; Design and Fabrication," in *Power Electronics, Drive Systems and Technologies Conference (PEDSTC), 2011 2nd*, Tehran, Iran, 2011.
- [108] L. Karunarathne, J.T. Economou, K. Knowles, "Model based power and energy management system for PEM fuel cell/ Li-Ion battery driven propulsion

- system," in *5th International conference on Power Electronics, Machines and Drives (PEMD)*, Bristol, United Kingdom, 2010.
- [109] W. Zhao, K. Choi, Z. Dilli, S. Bauman, T. Salter, M. Peckerar, "Design of radio frequency energy harvesting system for an unmanned airplane," in *Proceedings of International Semiconductor Device Research Symposium (ISDRS) 2011*, College Park, MD, 2011.
- [110] A.M.Stux, K.Swider-Lyons, "Survey of Commercial Small Lithium Polymer Batteries," Naval Research Laboratory, Washington, DC, 2007.
- [111] C. Alippi, C. Galperti, "An adaptive system for optimal solar energy harvesting in wireless sensor network nodes," *IEEE Trans. on Circuits and Systems I: Regular Papers*, vol. 55, pp. 1742-1750, 2008.
- [112] D. Dondi, A. Bertacchini, D. Brunelli, L. Larcher, L. Benini, "Modeling and optimization of a solar energy harvester system for self-powered wireless sensor networks," *IEEE Trans. Industrial Electronics*, vol. 55, pp. 2759-2766, 2008.
- [113] F.I. Simjee, P.H. Chou, "Efficient charging of supercapacitors for extended lifetime of wireless sensor nodes," *IEEE Trans. Power Electronics*, vol. 23, pp. 1526-1536, 2008.